



NTNU – Trondheim
Norwegian University of
Science and Technology

Nonlinear Dynamic Response of Concrete Structure with Soil-Structure Interaction

Marte Sørbrøden Talberg

Civil and Environmental Engineering

Submission date: June 2015

Supervisor: Amir Kaynia, KT

Norwegian University of Science and Technology
Department of Structural Engineering

Preface

This Master's thesis is the result of 20 weeks work, which was done in the spring semester of 2015. It has been written at the Department of Structural Engineering at the Norwegian University of Science and Technology (NTNU), and finalizes my study in Civil Engineering, with an emphasis on Computational Mechanics. My supervisor for this thesis has been Amir M. Kaynia (NTNU).

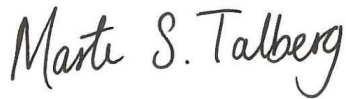
Acknowledgements

I would like to thank my supervisor Amir M. Kaynia for great guidance and help with my thesis. Through counseling and instructive discussions, he has inspired me to work hard, and has shared his knowledge and insight into nonlinear and earthquake analysis. His help has been of great significance for the final result of this thesis.

A special thanks is also given to Armin Gharakhanloo for providing necessary information and program files that were used in his thesis.

At last, I would like to show gratitude to my fellow M.Sc. candidate Veronica Liverud Krathe for good discussions and help throughout the semester.

Trondheim, 2015-06-10

A handwritten signature in black ink that reads "Marte S. Talberg". The script is cursive and fluid, with the first letters of each word being capitalized and prominent.

Marte Sørbrøden Talberg

Abstract

A common assumption for a structure that is subjected to an earthquake is that the structure is considered fixed at the base. In this thesis, analyses where the soil is deformed and the foundation may be moved and rotate have been done, and it has been investigated if this can reduce forces or displacements in the structure. This have been done through the use of soil-structure interaction (SSI).

In this thesis well known beam-column element formulations will be presented, and the benefits and disadvantages will be briefly explained. Formulations for elements that are force-based and displacement-based with distributed plasticity are presented, as well as concentrated plasticity elements with fiber discretization. Both the physical and numerical definition of localization are explained, and regularization methods to prevent numerical localization have been discussed. A pushover analysis has been done for each of the element formulation in SeismoStruct, such that the effect of change in number of elements and spacing in stirrups could be examined. The pushover analyses were done for load in both one and two directions. At last, a 3D-model was used to see the effect of change in spacing in stirrups when excitation in two directions is applied.

The attention is then brought over to use of SSI on structures, and the effect of applying this to a structure. An explanation on how to formulate SSI problem is given, and how to apply this in SeismoStruct through the use of *link* elements. These elements requires that a hysteresis curve is defined for each of the six degrees of freedom, and suitable models are presented. To model the soil's behavior, two models are used; the Ramberg–Osgood model and a linear model. To see the effect of SSI, a parameter study has been done. A study on how the results are changed by use of nonlinear horizontal springs, linear rocking springs, increased acceleration, smaller foundation and both linear horizontal and rocking springs have been done in SeismoStruct, by looking at one parameter at a time. Analyses where the structure was expanded by one floor, were also done, due to the possibility of seeing the effect of SSI in several places in the structure.

Through the analyses that is done, it has been observed that by taking the soil stiffness into consideration, the forces and moments can be reduced. The best effect was shown by decreasing the size of foundation, for both one and two stories.

Sammendrag

En antagelse som ofte blir gjort under dimensjonering for jordskjelv er at bygningen antas å være fast innspent. Det har i denne oppgaven blitt undersøkt om man, ved å anta at jorden vil kunne deformeres, kan redusere krefter og forflytninger i en bygning. Dette har blitt gjort ved bruk av jord-struktur-interaksjon (SSI).

Oppgaven presenterer kjente bjelke-søyle elementformuleringer, og det blir kort forklart deres fordeler og ulemper. Formuleringene som er i fokus er forskyvnings- og kraft-baserte elementer med fordelt plastisitet, samt elementer med konsentrert plastisitet med fiberdiskretisering. Både den fysiske og numeriske definisjonen av lokalisering blir forklart, og ulike metoder for å korrigere numeriske feil, kalt regulering, er presentert. De ulike elementformuleringene har videre blitt brukt i en pushoveranalyse i SeismoStruct. Dette ble gjort for å se på effekten av å modellere med forskjellig antall elementer og ulik avstand i bøylearmering. Pushoveranalysen har blitt utført med last påført i én og to retninger. Det har også blitt sett på hvordan resultatene påvirkes ved å endre avstand i bøylearmering for en 3D-modell med eksitasjon i to retninger.

Fokuset har så blitt ført over til bruk av SSI, og hvilken effekt man oppnår ved å innføre dette. Det blir forklart hvordan man bør formulere slike problemer, og hvordan man kan innføre dette i SeismoStruct ved bruk av *link* elementer. For disse elementene må det defineres hysteresekurver for alle seks frihetsgradene, og modeller som kan brukes blir presentert i oppgaven. De to modellene som er brukt til å modellere jordens oppførsel i denne oppgaven er Ramberg-Osgood og lineær modell. For å se effekten av SSI har det blitt gjort et parameterstudie, hvor én og én parameter har blitt endret av gangen. Det har blitt undersøkt hvordan resultatene blir påvirket av å modellere med en ikkelineær horisontalfjær, linear rotasjonsfjær, økt akselerasjon, mindre fundament og både lineære horisontal- og rotasjonsfjærer i SeismoStruct. Analyser hvor bygningen ble utvidet med en etasje ble også gjort, da det gjør det mulig å se effekten av SSI på flere steder enn ved bruk av en én-etasjes-bygning.

Fra de ulike analysene har det blitt observert at man kan redusere krefter og moment ved å ta hensyn til stivheten i jord. Størst effekt ble oppnådd ved å minke fundamentstørrelsen, både for én- og to etasjer.

Contents

Preface	i
Abstract	iii
Sammendrag	v
List of Figures	xiii
List of Tables	xv
1 Introduction	1
2 Distributed Inelasticity Elements	3
2.1 Model Assumptions	3
2.2 Distributed Inelasticity Elements	4
2.2.1 Displacement-Based Element Formulation	5
2.2.2 Force-Based Element Formulation	6
2.3 Numerical Issues in Distributed Inelasticity Modeling	7
2.3.1 Localization	7
2.3.2 Regularization Techniques	9
3 Concentrated Plasticity Elements	13
3.1 Point Hinge Models	13
3.2 Plastic Hinge Integration Methods	16
4 Hysteresis Models	19
4.1 Elasto-Plastic Model	19
4.2 Bilinear Model	20
4.3 Clough Model	21
4.4 Takeda Model	22
4.5 Q-hyst Model	23
5 Soil-Structure Interaction	25
5.1 Formulation of SSI Problem	27
5.2 SSI in SeismoStruct	29
6 Pushover Analysis	35
6.1 Effect of Change in Number of Elements	35

6.2	Effect of Different Spacing in Stirrups	37
6.2.1	Unidirectional Pushover Analysis	37
6.2.2	Bidirectional Pushover Analysis	39
7	Model Verification	43
7.1	Experimental Background	43
7.2	Modeling in SeismoStruct	47
7.2.1	2D-Model	47
7.2.2	3D-Model	49
8	Results	51
8.1	Effect of Change in Spacing in Stirrups	51
8.1.1	Hand Calculation of Shear Force	52
8.2	Effect of Soil Springs for One Story Building	56
8.3	Effect of Soil Springs for Two Story Building	73
8.4	Conclusions	93
	Bibliography	95

List of Figures

2.1	Displacements, internal forces and deformations.	3
2.2	Integration sections along the element's length, x , and section fiber discretization.	5
2.3	The element's dependence of size due to localization.	8
2.4	Objective and non-objective response of hardening and softening behavior.	9
2.5	Kent–Park stress-strain law and compressive fracture energy.	10
2.6	Plastic hinges formed at each end of a interior beam.	10
2.7	Comparison between different DB element lengths and experimental data.	12
3.1	Illustration of the two-component model.	13
3.2	Illustration of the one-component model.	14
3.3	Midpoint and endpoint plastic hinge integration methods.	17
3.4	Gauss–Radau and modified Gauss–Radau plastic hinge integration methods.	18
4.1	Elasto-plastic hysteresis model.	19
4.2	Bilinear hysteresis model.	20
4.3	Clough hysteresis model.	21
4.4	Takeda hysteresis model.	22
4.5	Q-hyst hysteresis model.	23
5.1	Illustration of foundation input motion and free-field motion.	25
5.2	Illustration of SSI.	26
5.3	Decomposition of a SSI problem.	27
5.4	Illustration of superposition theorem.	29
5.5	Time-displacement curve for the 3D-model with and without SSI. With high stiffness for the link elements.	30
5.6	Ramberg–Osgood hysteresis model.	31
5.7	Force-displacement curve for Ramberg–Osgood with different γ s.	32
6.1	Illustration of pushover analysis.	35
6.2	Force-displacement curve for different number of DB elements.	36
6.3	Force-displacement curve for different number of FB elements.	36
6.4	Force-displacement curve for different number of PH elements.	37

6.5	Load-displacement curve for a column consisting of a DB element with different spacings in stirrups.	38
6.6	Load-displacement curve for a column consisting of a FB element with different spacings in stirrups.	38
6.7	Load-displacement curve for a column consisting of a PH element with different spacings in stirrups.	39
6.8	Load-displacement curve for a column consisting of a DB element with different spacings in stirrups, from bidirectional pushover analysis.	40
6.9	Load-displacement curve for a column consisting of a FB element with different spacings in stirrups, from bidirectional pushover analysis.	40
6.10	Load-displacement curve for a column consisting of a PH element with different spacings in stirrups, from bidirectional pushover analysis.	41
6.11	Results from uni- and bidirectional pushover analyses for a column consisting of a FB element and a spacing of 150mm.	41
7.1	Picture of the prototype	43
7.2	Geometry of the prototype.	44
7.3	Longitudinal reinforcement pattern.	45
7.4	Positioning of the hydraulic jacks.	45
7.5	Artificial accelerogram.	46
7.6	Response spectrum for acceleration in Figure 7.5.	46
7.7	Time-histories for respectively 0.32g, 0.64g and 0.80g.	47
7.8	2D-model in SeismoStruct, with acceleration applied at the bottom of each column.	48
7.9	Displacements from static and dynamic analyses for the 2D-model with FB-elements.	48
7.10	Screen shot of the model in SeismoStruct.	49
7.11	Displacement for the 3D-model with excitation in one and two directions.	50
8.1	Time-displacement curve for different spacing in stirrups for base case acceleration.	51
8.2	Cross-section of the columns.	52
8.3	Total base shear against time for different spacing in stirrups for base case acceleration.	53
8.4	Base shear against time for one column with 150mm spacing for base case acceleration.	53
8.5	Displacement against time for different spacing in stirrups, with 5× acceleration applied.	54
8.6	Total base shear against time for different spacing in stirrups, with 5× acceleration applied.	54
8.7	Displacement against time for different spacing in stirrups with 10× acceleration applied.	55
8.8	Force against time for different spacing in stirrups with 10× acceleration applied.	55
8.9	Displacements for structure with nonlinear horizontal springs applied.	57
8.10	Shear force at base of column with nonlinear horizontal springs applied.	57
8.11	Moment at base of column with nonlinear horizontal springs applied.	58

8.12 Force-displacement response for structure with nonlinear horizontal springs applied.	58
8.13 Moment-rotation response at base of column with nonlinear horizontal springs applied.	59
8.14 Force-displacement response for nonlinear horizontal spring.	60
8.15 Displacements for structure with linear rocking springs applied.	60
8.16 Shear force at base of column with linear rocking springs applied.	61
8.17 Moment at base of column with linear rocking springs applied.	61
8.18 Force-displacement response for structure with linear rocking springs applied.	62
8.19 Moment-rotation response at base of column with linear rocking springs applied.	62
8.20 Moment-rotation response in rocking spring.	63
8.21 Displacements for structure with linear rocking springs applied.	64
8.22 Shear force at base of column with linear rocking springs applied.	64
8.23 Moment at base of column with linear rocking springs applied.	65
8.24 Force-displacement response for structure with linear rocking springs applied.	65
8.25 Moment-rotation response at base of column with linear rocking springs applied.	66
8.26 Displacements for structure with $1m \times 1m$ and $1.5m \times 1.5m$ foundation.	67
8.27 Shear force at base of column for structure with $1m \times 1m$ and $1.5m \times 1.5m$ foundation.	67
8.28 Moment at base of column for structure with $1m \times 1m$ and $1.5m \times 1.5m$ foundation.	68
8.29 Force-displacement response for structure with $1m \times 1m$ and $1.5m \times 1.5m$ foundation.	68
8.30 Moment-rotation response at base of column for structure with $1m \times 1m$ and $1.5m \times 1.5m$ foundation.	69
8.31 Displacement of roof for structure with linear soil springs, and foundation of $1m \times 1m$	70
8.32 Base shear at base of column with linear soil springs, and foundation of $1m \times 1m$	70
8.33 Moment at base of column with linear soil springs, and foundation of $1m \times 1m$	71
8.34 Force-displacement response for structure with linear soil springs, and foundation of $1m \times 1m$	71
8.35 Moment-rotation response at base of column with linear soil springs, and foundation of $1m \times 1m$	72
8.36 2D model with two stories.	73
8.37 Displacements for structure with nonlinear horizontal springs applied.	75
8.38 Shear force at base of column with nonlinear horizontal springs applied	75
8.39 Moment at base of column with nonlinear horizontal springs applied.	76
8.40 Force-displacement response for structure with nonlinear horizontal springs applied.	76
8.41 Moment-rotation response at base of column at ground floor. Nonlinear horizontal springs applied at the base of the structure.	77

8.42 Moment-rotation response at base of column in first floor. Nonlinear horizontal springs applied at the base of the structure. 77

8.43 Force-displacement response for nonlinear horizontal spring. 78

8.44 Displacements for structure with linear rocking springs applied. 78

8.45 Shear force at base of column with linear rocking springs applied. 79

8.46 Moment at base of column with linear rocking springs applied. 79

8.47 Force-displacement response for structure with linear rocking springs applied. 80

8.48 Moment-rotation response at base of column at ground floor. Linear rocking springs applied at the base of the structure. 80

8.49 Moment-rotation response at base of column in first floor. Linear rocking springs applied at the base of the structure. 81

8.50 Displacements for structure with linear rocking springs applied, and increased acceleration. 82

8.51 Shear force at base of column with linear rocking springs applied, and increased acceleration. 82

8.52 Moment at base of column with linear rocking springs applied, and increased acceleration. 83

8.53 Force-displacement response for structure with linear rocking springs applied, and increased acceleration. 83

8.54 Moment-rotation response at base of column at ground floor. Linear rocking springs applied at the base of the structure, and increased acceleration. 84

8.55 Moment-rotation response at base of column in first floor. Linear rocking springs applied at the base of the structure, and increased acceleration. 85

8.56 Displacements for structure with linear rocking springs applied, and foundation of 1.5m×1.5m. 86

8.57 Shear force at base of column with linear rocking springs applied, and foundation of 1.5m×1.5m. 86

8.58 Moment at base of column with linear rocking springs applied, and foundation of 1.5m×1.5m. 87

8.59 Force-displacement response for structure with linear rocking springs applied, and foundation of 1.5m×1.5m. 87

8.60 Moment-rotation response at base of column at ground floor. Linear rocking springs applied at the base of the structure, and foundation of 1.5m×1.5m. 88

8.61 Moment-rotation response at base of column in first floor. Linear rocking springs applied at the base of the structure, and foundation of 1.5m×1.5m. 88

8.62 Displacement of roof for structure with linear soil springs, and foundation of 1.5m×1.5m. 89

8.63 Base shear at base of column with linear soil springs, and foundation of 1.5m×1.5m. 89

8.64 Moment at base of column with linear soil springs, and foundation of 1m×1m. 90

8.65 Force-displacement response for structure with linear soil springs, and foundation of 1.5m×1.5m. 90

- 8.66 Moment-rotation response at base of column at ground floor. Linear soil springs applied at the base of the structure, and foundation of $1.5\text{m} \times 1.5\text{m}$. 91
- 8.67 Moment-rotation response at base of column in first floor. Linear soil springs applied at the base of the structure, and foundation of $1.5\text{m} \times 1.5\text{m}$. 91

List of Tables

5.1	Parameters that must be defined in SeismoStruct for the Ramberg–Osgood model.	31
5.2	Parameters used for the Ramberg–Osgood model.	33
6.1	Confinement factors for the different spacings.	42
7.1	Values used to create the models.	47
8.1	Parameters for a foundation of $1m \times 1m$	66
8.2	Maximum moment for the different analyses for the one story building, and reduction of maximum moment for the fixed structure in percent. . .	73
8.3	Parameters for a foundation of $2m \times 2m$	74
8.4	Maximum moment for the different analyses for the two story building, and reduction of maximum moment for the fixed structure in percent. . .	92

Chapter 1

Introduction

Dimensioning of a building requires that several factors are being taken into consideration. One of these factors, that needs to be considered, is dynamic response due to an earthquake. Even for regions where the chance that an earthquake will occur is small, it is required that the building is dimensioned for an earthquake. The seismic design of a structure is normally done by neglecting interaction between the soil and the structure, and the assumption of a fixed structure is used to evaluate the dynamic response of the structure (Pecker (2008)). Even though this assumption is frequently used, it does not give an accurate dynamic response. During seismic loading the soil will deform and the foundation may rotate and move horizontally. The interaction between the structure and the soil is named soil-structure interaction (SSI).

Soil-structure interaction arises from two phenomena: inertial and kinematic interaction. When a structure is being subjected to an earthquake, forces are formed at the base of the structure. These forces generate internal forces in the superstructure, and this interaction is named inertial interaction. Kinematic interaction, on the other hand, arises from the difference in stiffness for the soil and the embedded part of the structure. When the soil is deformed, the stiffness of the foundation tries to prevent it from following the displacements. The relative displacement of the structure is the sum of the displacements imposed by the inertial and kinematic interaction, and gives a system of differential equations that are used to formulate SSI problems.

Buildings are often strengthened at the most vulnerable junctions to withstand the forces and moments that take place during seismic loading. One method to make junctions more solid, is to increase the amount of reinforcement. However, it is known that the forces occurring for a fixed base structure is larger than for a structure where the foundation is allowed to rotate and move horizontally. If it can be shown that SSI reduces forces and moments, it may lead to that a lower dimensioning force can be used in the calculations. This also means that the amount of reinforcement can be reduced, which again leads to lower costs. The main focus of this thesis is therefore to investigate the effect of SSI, and how the response of the structure is influenced.

This thesis is divided into 8 chapters, where Chapter 1 is the current chapter. Chapter 2 is presenting distributed plasticity elements. Displacement-based and force-based elements are discussed with focus on the formulations and the numerical issues that may occur. In Chapter 3, the concentrated plasticity elements are introduced. The plastic hinge elements are presented, and it is described how the force-based formulation can be modified to include the fact that plastic hinges are formed. Chapter 4 focuses on hysteresis models, and presents a selection of the most common models. In Chapter 5 soil-structure interaction is in focus, and it is explained how a SSI problem is formulated. It is also discussed how SSI can be implemented in SeismoStruct through the use of *link* elements. In Chapter 6 pushover analyses are done, with a focus on what effect of changing the number of elements and changing the spacing in stirrups gives. For the different spacings, both a uni- and bidirectional pushover were done. Chapter 7 describes the experiment which was the foundation of Gharakhanloo's thesis (2014). The same structure is used in this thesis, and the details of how it is modeled in SeismoStruct is therefore given, in addition to the acceleration that is used. In the last chapter, which is Chapter 8, the model is exposed to a ground acceleration. The effect of spacing in stirrups has been examined, and a parameter study is done. Several parameters is regarded, such that the effect of SSI is seen for different situations.

Chapter 2

Distributed Inelasticity Elements

2.1 Model Assumptions

In the following chapter, two different beam-column elements will be presented; displacement- and force-based elements. Both of these elements are based on the Euler–Bernoulli beam theory. The torsion is assumed to be uncoupled from the axial and flexural response, and is therefore omitted from the models for simplicity. Figure 2.1 shows how the displacements, internal forces and deformations is defined within an element.

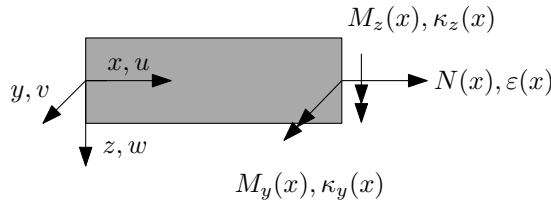


Figure 2.1: Displacements, internal forces and deformations.

With these assumptions, the variables of the element displacement field can be described by

$$\mathbf{u}(x) = \begin{bmatrix} u(x) \\ w(x) \\ v(x) \end{bmatrix} \quad (2.1)$$

where $u(x)$ is the axial displacement, while $v(x)$ and $w(x)$ are the transverse displacement in y - and z -direction. The corresponding deformation field is given by

$$\mathbf{e}(x) = \begin{bmatrix} \varepsilon_a(x) \\ \kappa_y(x) \\ \kappa_z(x) \end{bmatrix} = \begin{bmatrix} \frac{\partial u(x)}{\partial x} + \frac{1}{2} \left(\frac{\partial^2 w(x)}{\partial x^2} \right)^2 + \frac{1}{2} \left(\frac{\partial^2 v(x)}{\partial x^2} \right)^2 \\ -\frac{\partial^2 w(x)}{\partial x^2} \\ \frac{\partial^2 v(x)}{\partial x^2} \end{bmatrix} \quad (2.2)$$

The internal section force fields are defined as

$$\mathbf{s}(x) = \begin{bmatrix} N(x) \\ M_y(x) \\ M_z(x) \end{bmatrix} \quad (2.3)$$

where $\mathbf{s}(x)$ contains the axial force, $N(x)$, and the bending moments, $M_y(x)$ and $M_z(x)$. Assuming that the constitutive relation

$$\mathbf{s}_{n+1}(x) = \mathbf{C}[\mathbf{s}_n(x), \mathbf{e}_n(x), \mathbf{e}_{n+1}(x)] \quad (2.4)$$

are known, and its linearization,

$$\Delta \mathbf{s}(x) = \mathbf{k}_s(x) \Delta \mathbf{e}(x) \quad (2.5)$$

then the section stiffness matrix, \mathbf{k}_s , is given by

$$\mathbf{k}_s = \frac{\partial \mathbf{s}}{\partial \mathbf{e}} = \begin{bmatrix} \frac{\partial N}{\partial \varepsilon} & \frac{\partial N}{\partial \kappa_y} & \frac{\partial N}{\partial \kappa_z} \\ \frac{\partial M_y}{\partial \varepsilon} & \frac{\partial M_y}{\partial \kappa_y} & \frac{\partial M_y}{\partial \kappa_z} \\ \frac{\partial M_z}{\partial \varepsilon} & \frac{\partial M_z}{\partial \kappa_y} & \frac{\partial M_z}{\partial \kappa_z} \end{bmatrix} \quad (2.6)$$

where n denotes the time. For simplicity the x-coordinate is left out of the expressions in \mathbf{k}_s . The equations above form the force-deformation relations of a section.

2.2 Distributed Inelasticity Elements

The concentrated, or lumped, inelasticity elements consider an inner span of the element as linearly elastic, and has a predefined length where inelasticity can occur. In comparison, the distributed inelasticity elements lets inelastic behavior occur at any section point throughout the whole length of the element. The section points is determined by the integration model that is used. Distributed inelasticity elements have the disadvantage that it requires a higher computational cost, but on the other hand it gives a more exact result than the concentrated inelasticity elements.

The fiber model is a common and useful approach to compute the sectional response. It is done by a refined discretization of the section into small domains which have a uniaxial inelastic behavior. For a structural member consisting of reinforced concrete, the member will not behave homogeneous, and it is therefore very useful to discretize the member and take the different properties of the materials into account. Figure 2.2 shows how a reinforced concrete beam can be divided into sections of confined core concrete, unconfined cover concrete and steel bars. Thus, three different material models need to be defined to model the element. To reduce the computational cost for a fiber model, the level of discretization should be evaluated. For instance, if the bending moment about the y-axis is significantly lower than the bending moment about the z-axis, the number of fibers along the z-axis can be set much lower than the number of fibers in the y-direction.

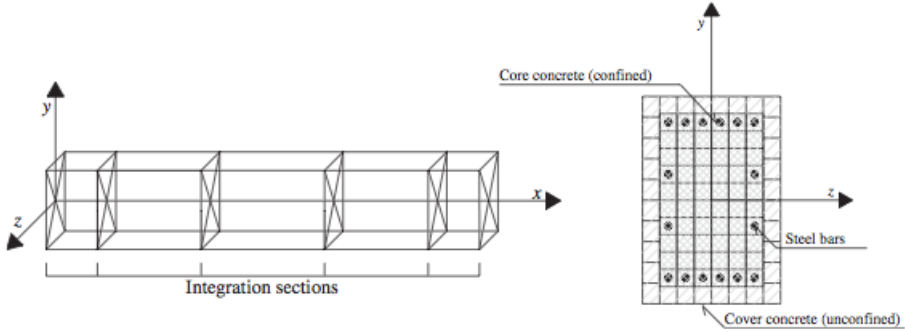


Figure 2.2: Integration sections along the element's length, x , and section fiber discretization (Calabrese et al. (2010)).

The fiber model is normally modeled by the use of displacement-based or force-based formulation. The main difference is if the formulation is based on the element's stiffness or the element's flexibility.

2.2.1 Displacement-Based Element Formulation

For the displacement-based (DB) formulation, the displacement fields of the element are discretized and interpolated in terms of the generalized degrees of freedom \mathbf{q} . The relation between the displacement field and the generalized degrees of freedom is given as

$$\mathbf{u}(x) = \mathbf{N}(x)\mathbf{v} \quad (2.7)$$

where $\mathbf{N}(x)$ is a matrix containing the shape functions for the axial and transverse displacements, \mathbf{N}_u , \mathbf{N}_w and \mathbf{N}_v .

$$\mathbf{N}(x) = \begin{bmatrix} \mathbf{N}_u(x) & \mathbf{0} & \mathbf{0} \\ \mathbf{0} & \mathbf{N}_w(x) & \mathbf{0} \\ \mathbf{0} & \mathbf{0} & \mathbf{N}_v(x) \end{bmatrix} \quad (2.8)$$

The elements are based on linear Lagrangian shape functions for the axial displacements, and cubic Hermetian shape functions for the transverse displacement of the member (Neuenhofer and Filippou (1997)). The deformation field is related to the generalized degrees of freedom through the strain-displacement transformation matrix, $\mathbf{B}(x)$, which contains the first derivative of the axial shape function, and second derivative of the transverse shape functions

$$\mathbf{e}(x) = \mathbf{B}(x)\mathbf{v} \quad (2.9)$$

By using the incremental version of Equation (2.9), and the constitutive relation in Equation (2.5) the following relation for the force field increment is found

$$\Delta \mathbf{s}(x) = \mathbf{k}_s(x)\Delta \mathbf{e}(x) = \mathbf{k}_s(x)\mathbf{B}(x)\Delta \mathbf{v} \quad (2.10)$$

From the principle of virtual displacement the equilibrium equation is derived:

$$\mathbf{q} = \int_0^L \mathbf{B}^T(x) \mathbf{s}(x) dx \quad (2.11)$$

The element stiffness matrix is further derived by taking the derivative of \mathbf{q} with respect to the generalized degrees of freedom, \mathbf{v}

$$\mathbf{k} = \frac{\partial \mathbf{q}}{\partial \mathbf{v}} = \int_0^L \mathbf{B}^T(x) \mathbf{k}_s(x) \mathbf{B}(x) dx \quad (2.12)$$

Distribution of stresses in beam-column material sections often tend to be irregular and discontinuous. For reinforced concrete, this may be inelasticity, which causes a non-linear curvature. Equations (2.11) and (2.12) should therefore be solved by numerical integration, and not classical integration. The discrete form of the equations becomes:

$$\mathbf{q} = \int_0^L \mathbf{B}^T(x) \mathbf{s}(x) dx \approx \sum_{i=1}^{N_p} \mathbf{B}_i^T \mathbf{s} \omega_i \quad (2.13)$$

and

$$\mathbf{k} = \int_0^L \mathbf{B}^T(x) \mathbf{k}_s(x) \mathbf{B}(x) dx \approx \sum_{i=1}^{N_p} \mathbf{B}_i^T \mathbf{k}_{s,i} \mathbf{B}_i \omega_i \quad (2.14)$$

2.2.2 Force-Based Element Formulation

Instead of using shape functions for displacement, the force-based (FB) formulation uses the shape functions for internal forces. The internal forces $\mathbf{s}(x)$ are related to the generalized nodal forces \mathbf{q} through the force interpolation functions, $\mathbf{b}(x)$

$$\mathbf{s}(x) = \mathbf{b}(x) \mathbf{q} \quad (2.15)$$

In Equation (2.15), the matrix $\mathbf{b}(x)$ contains the interpolation functions that relates the section and basic forces. The matrix describes the axial force and bending moments at location x along an element with length L , and is given as

$$\mathbf{b}(x) = \begin{bmatrix} 1 & 0 & 0 & 0 & 0 \\ 0 & \frac{x}{L} - 1 & \frac{x}{L} & 0 & 0 \\ 0 & 0 & 0 & \frac{x}{L} - 1 & \frac{x}{L} \end{bmatrix} \quad (2.16)$$

The inverse form of Equation (2.5) with the incremental version of Equation (2.15) gives the following incremental deformation field:

$$\Delta \mathbf{e}(x) = \mathbf{k}_s^{-1}(x) \Delta \mathbf{s}(x) = \mathbf{f}_s(x) \Delta \mathbf{s}(x) = \mathbf{f}_s(x) \mathbf{b}(x) \Delta \mathbf{q} \quad (2.17)$$

As seen from Equation (2.17), the section flexibility matrix is the inverse of the section stiffness matrix, $\mathbf{f}_s(x) = \mathbf{k}_s^{-1}(x)$.

The compability condition

$$\mathbf{v} = \int_0^L \mathbf{b}^T(x) \mathbf{e}(x) dx \quad (2.18)$$

is found through the principle of virtual forces, where \mathbf{v} describes the element end displacements. The flexibility matrix of the element is given by the derivative of \mathbf{v} with respect to \mathbf{q}

$$\mathbf{f} = \frac{\partial \mathbf{v}}{\partial \mathbf{q}} = \int_0^L \mathbf{b}^T(x) \mathbf{f}_s(x) \mathbf{b}(x) dx \quad (2.19)$$

To get a meaningful expression for \mathbf{f} , it can only be derived for a beam-element that do not have any rigid-body modes (Neuenhofer and Filippou (1997)). The discrete forms of Equations (2.18) and (2.19) are written as

$$\mathbf{v} = \int_0^L \mathbf{b}^T(x) \mathbf{e}(x) dx \approx \sum_{i=1}^{N_p} \mathbf{b}_i^T \mathbf{e}_i \omega_i \quad (2.20)$$

and

$$\mathbf{f} = \int_0^L \mathbf{b}^T(x) \mathbf{f}_s(x) \mathbf{b}(x) dx \approx \sum_{i=1}^{N_p} \mathbf{b}_i^T \mathbf{f}_{s,i} \mathbf{b}_i \omega_i \quad (2.21)$$

For a material with linear elastic behavior, the FB and DB formulation will give the same results, provided that only nodal forces are acting on the element. On the contrary, for an inelastic material, the curvature field may be nonlinear and it can be hard to capture the real deformed shape due to an imposed displacement field. With a situation where an inelastic material is used in combination with a DB formulation a refined meshing of the structural member is required. This is due to the assumption that the inside of each sub domain consists of a linear curvature field. The FB formulation, on the other hand, does not restrain the element's displacement field and is therefore always exact. Along the length of the element, the integration sections are used for numerical integration. This means that a member can be modeled with a single finite element. Due to the fact that the force field is exact even if the level of inelasticity is high or low, each element does not require meshing, regardless of the cross section of the element.

2.3 Numerical Issues in Distributed Inelasticity Modeling

2.3.1 Localization

For structural members made of concrete, localization may occur. From a physical point of view, the term localization refers to the fact that the descending part of the stress-strain curve becomes dependent of the size of the specimen. That is, a concrete specimen in compression will collapse, due to concentrated strains in a localized region of the whole specimen. A stress-strain curve will therefore not depend on the concrete properties, but rather depend on the size. The dependence of size is shown in Figure 2.3. Localization was first found to happen in tensile tests, where it occurs as a crack,

and is well documented. For compression, the localization results in damage zones being formed. For the type of model used later in this thesis the main focus will be on localization for compression. For a specimen being subjected to compression, localization will take place after the peak point is reached (Hillerborg (1990)). To take the physical definition of localization into account, one can adjust the structural element's stress-strain relationship. This, however, leads to a numerical problem.

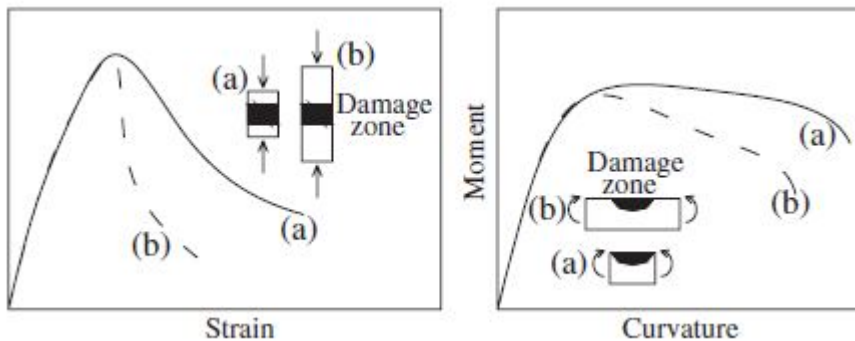


Figure 2.3: The element's dependence of size due to localization (Calabrese et al. (2010)).

From a numerical point of view, localization is related to the fact that the concentration of inelasticity is dependent on the choice of mesh and numerical integration scheme (Calabrese et al. (2010)). The numerical problems arises from the use of finite elements, and refers to the computed damage that occurs. The numerical results for softening behavior does not converge to a stable solution, which is termed non-objective response. While it, on the other hand, does converge for the hardening behavior, which is termed objective response.

For displacement-based elements that show softening behavior, the strain localization is forced to form in a single element by the displacement interpolation functions. The mesh element with the highest bending moment is where localization occurs. On the other hand, a force-based element will have the strain localized at one integration point (Coleman and Spacone (2001)). The integration point where this occurs is, similar to the displacements-based elements, at the point of highest bending moment.

Considering a cantilever with a axial load, and lateral displacement as in Figure 2.4, the bending moment will always be highest at the base of the column. If modeled with DB elements, the localization will always occur in the bottom element. By refining the mesh, the strain will still localize in the same element, and this will increase the strains within the element. By use of FB elements, localization will occur in the first integration point. The FB element does only require one element per structural member, and an increase of the strains at the bottom integration point will only be happen by increasing the total number of integration points.

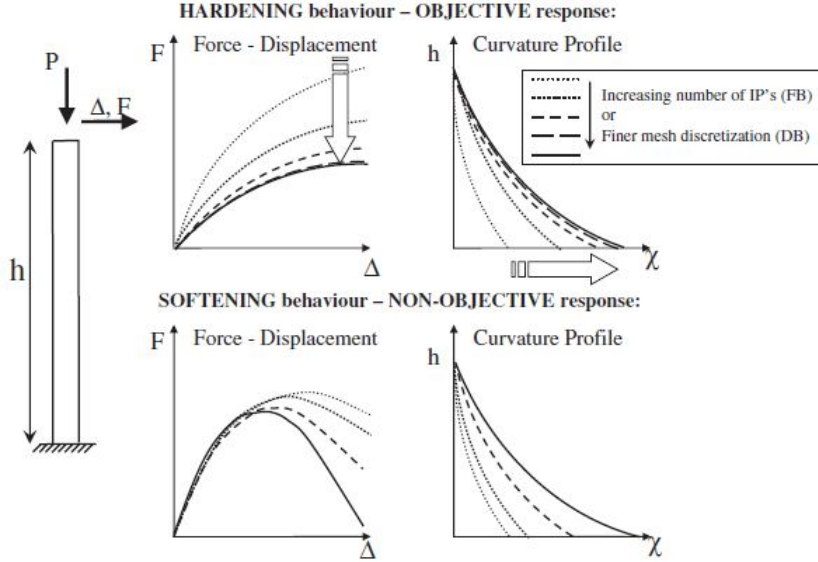


Figure 2.4: Objective and non-objective response of hardening and softening behavior (Calabrese et al. (2010)).

2.3.2 Regularization Techniques

Force-Based Formulation

Constant fracture energy is a well used concept for DB elements in tension, but is also applied to FB elements that soften in compression. Although the use is not as widely accepted for compression as it is for tension, it is found through research (Jansen and Shah (1997)) that the theory also holds for localization in compression. The constant fracture energy concept is based on including an extra material parameter, the fracture energy in compression, G_f^c , which is defined as

$$G_f^c = \int \sigma du_i = L_{IP} \int \sigma d\varepsilon_i \quad (2.22)$$

The compressive strength is here written as σ , while u_i is the inelastic displacement, and ε_i is the inelastic strain. L_{IP} represents the length of the integration point where the localization takes place. In Figure 2.5 the regularization is applied to the Kent and Park law used for the concrete fibers of the fiber section (Coleman and Spacone (2001)). As seen from the figure, the prepeak behavior is given by a parabola. After the peak, the softening-behavior will be linear until it reaches 20% of f_c' . After this turning point, ε_{20} , the stress is assumed to be constant. From Figure 2.5, the following expression for ε_{20} is derived

$$\varepsilon_{20} = \frac{G_f^c}{0.6f_c' L_{IP}} - \frac{0.8f_c'}{E} + \varepsilon_0 \quad (2.23)$$

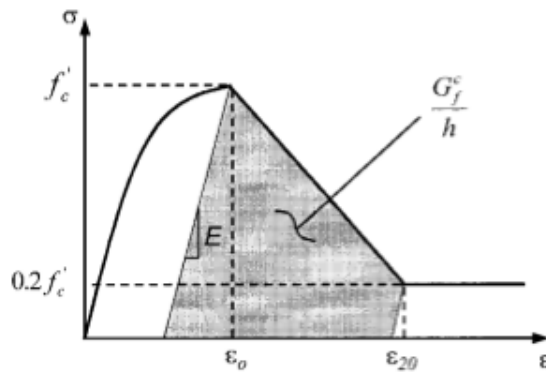


Figure 2.5: Kent–Park stress-strain law and compressive fracture energy (Coleman and Spacone (2001)).

The values of G_f^c , f'_c , E and ϵ_0 are assumed to be constant. The only parameter varying is the length of integration points, L_{IP} , and to maintain a constant fracture energy it is therefore necessary to adjust ϵ_{20} for each integration point.

In some cases, the constant fracture energy criterion is not sufficient. This occurs for instance when the length of the first integration point does not correspond to the physical length of the plastic hinge. Coleman and Spacone(2001) suggested to use curvature post processing to obtain objectivity in these cases. An illustration of a interior beam, with plastic hinges at both ends, is depicted in Figure 2.6. The curvature of the plastic hinge region is divided into an elastic and an inelastic component.

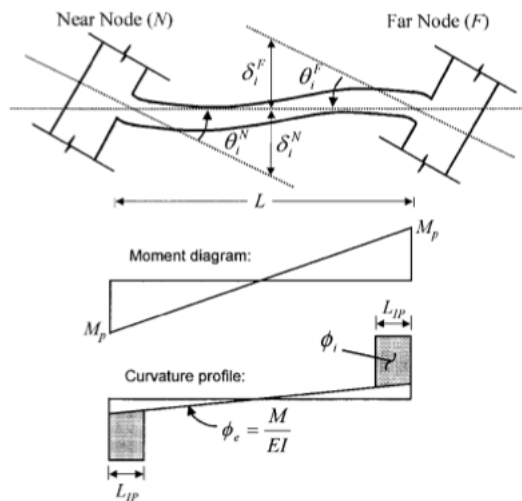


Figure 2.6: Plastic hinges formed at each end of a interior beam (Coleman and Spacone (2001)).

The inelastic curvature component from the analysis is approximated as

$$\phi_i^{model} \cong \frac{\delta_i}{L_{IP} \left(\frac{L}{2} - \frac{L_{IP}}{2} \right)} \quad (2.24)$$

By substituting the length of integration point, L_{IP} , with the actual length of the plastic hinge, L_p , an approximation for the inelastic curve based on the assumed length of the plastic hinge is given as

$$\phi_i^{predict} \cong \frac{\delta_i}{L_p \left(\frac{L}{2} - \frac{L_p}{2} \right)} \quad (2.25)$$

The total curvature can be calculated by

$$\phi = \phi_e + (scale\ factor)\phi_i^{model} \quad (2.26)$$

where ϕ_e is the elastic component of the total curvature. By solving for δ_i and combining Equation (2.24) and Equation (2.25), the scale factor is given by equation 2.28 for a double-curvature case, as the one shown in Figure 2.6.

$$scale\ factor = \frac{w_{IP}L^2(1-w_{IP})}{L_p(L-L_p)} \quad (2.27)$$

For a single-curvature case, the scale factor expression will be

$$scale\ factor = \frac{w_{IP}L^2(2-w_{IP})}{L_p(2L-L_p)} \quad (2.28)$$

For both of the expressions above, w_{IP} describes the weight of the extremal integration point.

From this it is seen that if $L_{IP} = L_p$ there will not be necessary to post-process the curvature to obtain objectivity. Problems may occur by choosing the length of integration points to correspond with the plastic hinge length. In most cases the length of the elements needs to be adjusted, which results in an extra element and increased computational costs.

Displacement-Based Formulation

For a DB element, a typical regularization technique is to use the length of the plastic hinge as a base to assume the length of the element. Formerly it was common to believe that localization was formed in a single element, and not in one integration point. With that assumption, the length of the most strained element was defined by the length of the plastic hinge. Through later work and research, it is found that localization occurs in one integration point. This behavior is similar to the behavior of FB elements (Zeris and Mahin (1988)). The length for the most strained integration point should be equal to L_p , and for a element with two Gauss points, where each integration point is given the same weight, the length of the most strained element should then be $2L_p$. L_p is a predetermined length and may be found through the following equation

$$L_p = 0.08L + 0.022d_b f_y \quad (2.29)$$

Equation (2.29) is said to give a good estimation of the effective plastic hinge length and was found from observations from experiments (Paulay and Priestley (2009)). L is the length of the member, while f_y is the steel reinforcement's yield stress and d_b is the diameter of the longitudinal reinforcement.

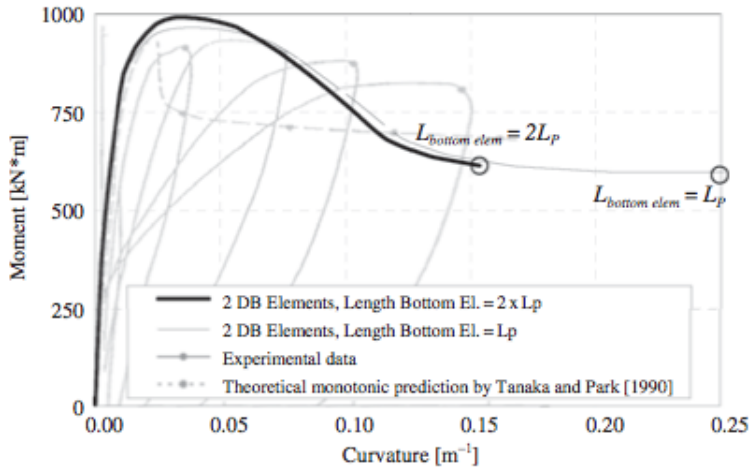


Figure 2.7: Comparison between different DB element lengths and experimental data (Calabrese et al. (2010)).

Results from experiments that have been done are compared to analysis results and depicted in Figure 2.7. It is clear that an increased length of the element gives a better approximation for the curvature of the member. The graph also shows that the principle described above does not give a good estimation for the post-peak stage here. This is due to the column's total height for the example used here is 1.65 m and the length of the base element is 0.71 m , which gives a ratio between them that is significantly higher than encountered in practice.

Chapter 3

Concentrated Plasticity Elements

3.1 Point Hinge Models

For a structure subjected to large lateral forces, the most significant inelastic deformations will form at the ends of the structural members. The largest bending moments will also form at these points, and not at the mid-span of the members as moment from dead and live loads do.

In 1965, Clough, Benuska and Wilson (Filippou (2013)) introduced the first model to take hardening response in nonlinear structural analysis into consideration. The first model was named the two-component model, and consists of two components in parallel. One of the components is modeled to be linear elastic-perfectly plastic, while the other component is modeled to be linear elastic. An illustration of the model is given in Figure 3.1. The interaction between the two components, results in a model that is able to represent bilinear response.

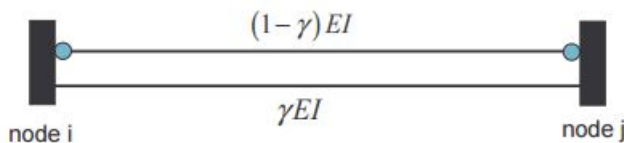


Figure 3.1: Illustration of the two-component model (Filippou (2013)).

For both of the components, the axial stiffness is defined to be linear and uncoupled from the flexural response. The stiffness for the linear elastic-perfectly plastic element is $(1 - \gamma)EI$, where γ is the ratio between the stiffness of the linear elastic flexural component and the flexural stiffness of the element, EI . It is through the linear elastic component that linear hardening behavior of the element is represented.

As the components are parallel, the stiffness matrix is the sum of the stiffness matrices for the two components. The elastic rotational stiffness, k_{el} , before yielding will be EI . Post yielding, the stiffness will be equal to only the stiffness of the linear elastic component, since the upper component has zero stiffness as it has reached perfect plasticity.

In 1967 the one-component model was presented by Giberson (Filippou (2013)). This model consist of a linear elastic beam element that is in series with nonlinear springs at the ends of the beam. Despite the name of the model refers to one component, it actually consists of three components, two nonlinear springs and one elastic beam. The springs does only contribute to the stiffness when the plastic capacity is exceeded at one of the ends of the beam. In Figure 3.2, the one-component model is illustrated. The linear hardening force-deformation response in each spring is given by the linear elastic stiffness under antisymmetric bending multiplied with the hardening stiffness ratio, η .

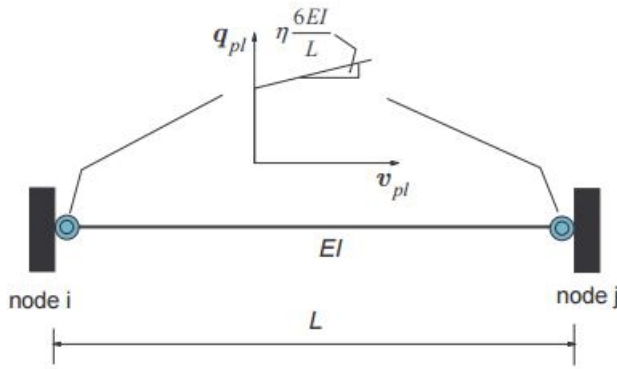


Figure 3.2: Illustration of the one-component model (Filippou (2013)).

For a series model, the stiffness matrix is found by taking the inverse of the flexibility matrix. The flexibility matrix is the sum of the components flexibilities, \mathbf{f}_{el} and \mathbf{f}_{pl} , where the elastic part is from the beam, and the plastic part from the nonlinear springs. The matrices are given in Equation (3.1) and (3.2), and the variables r_i and r_j are set to 1 or 0, depending on whether the corresponding beam end has reached the plastic moment capacity, M_p .

$$\mathbf{f}_{el} = \frac{L}{6EI} \begin{bmatrix} 2 & 1 \\ 1 & 2 \end{bmatrix} \quad (3.1)$$

$$\mathbf{f}_{pl} = \frac{L}{6\eta EI} \begin{bmatrix} r_i & 0 \\ 0 & r_j \end{bmatrix} \quad (3.2)$$

Both of the models above are based on concentrated plasticity theory, and have the advantage of being fundamentally simple. On the other hand, a disadvantage is that the plastic hinges are concentrated at the end nodes. In addition, the concentrated plasticity models separate axial-moment interaction from the element behavior. A calibra-

tion is therefore necessary to find the correct interaction along the member (Scott and Fenves (2006)).

To improve the concentrated integration methods for plastic hinge, fiber modeling at specific lengths of the element members ends have been introduced. Since it is desirable to achieve objectivity for softening response of FB elements, the fiber modeled member ends are based on FB formulation. The interior part of these elements are said to be linear elastic, while the outer parts are assumed to form plastic hinges. Thus, the FB formulation from Subsection 2.2.2 needs some modifications to take this into consideration.

The length of the plastic hinges at node i and j are denoted as l_{pi} and l_{pj} , and the plastic hinge integration methods that will be presented are based on the assumption that nonlinear behavior is restricted to occur in these regions. The compatibility relationship in Equation (2.18) is rewritten as three separate integrals, where two of the integrals represents the two hinge regions, while the third represents the interior region. With these changes, the compatibility condition becomes

$$\mathbf{v} = \int_0^{l_{pi}} \mathbf{b}^T(x) \mathbf{e}(x) dx + \int_{l_{pi}}^{L-l_{pj}} \mathbf{b}^T(x) \mathbf{e}(x) dx + \int_{L-l_{pj}}^L \mathbf{b}^T(x) \mathbf{e}(x) dx \quad (3.3)$$

Numerical integration is required to find the section deformations for the plastic hinge regions, while the interior part is assumed to be linear elastic and is evaluated by the flexibility of the interior region.

$$\mathbf{v} = \sum_{i=1}^{N_p} \mathbf{b}^T(x) \mathbf{e}_i(x) \omega_i + \mathbf{f}_{int}^{el} \mathbf{q} \quad (3.4)$$

In Equation (3.4), N_p is the number of integration points in the plastic hinge region, with the weight ω_i of the plastic hinge integration points. \mathbf{f}_{int}^{el} is the flexibility matrix for the interior region of the element, which is given by the closed-form integral

$$\mathbf{f}_{int}^{el} = \int_{l_{pi}}^{L-l_{pj}} \mathbf{b}^T(x) \mathbf{f}_s^{el} \mathbf{b}(x) dx \quad (3.5)$$

The elastic flexibility coefficients at a cross section of the interior region are assembled in the flexibility matrix, \mathbf{f}_s^{el} , which is given as

$$\mathbf{f}_s^{el} = \begin{bmatrix} \frac{1}{EA} & \mathbf{0} \\ \mathbf{0} & \frac{1}{EI} \end{bmatrix} \quad (3.6)$$

Through linearization of Equation (3.4), the element flexibility is given as the sum of the numerical integration over the hinge regions and the flexibility of the interior region

$$\mathbf{f} = \sum_{i=1}^{N_p} \mathbf{b}_i^T(x) \mathbf{f}_s \mathbf{b}_i(x) \omega_i + \mathbf{f}_{int}^{el} \quad (3.7)$$

To represent strain softening as good as possible in the plastic hinge regions, the plas-

tic hinge integration rule used in Equation (3.4) and (3.7) has to satisfy the criteria as follows (Scott and Fenves (2006)):

1. To detect the largest bending moments, integration points should be located at the element ends.
2. To provide the exact solution for linear curvature distributions, quadratic polynomials should be integrated exactly.
3. Deformations should be integrated over the plastic hinge lengths l_{pi} and l_{pj} by use of one integration point in each hinge region.

By use of the Gauss-Lobatto integration rule, the first two criteria can be satisfied, but because the plastic hinge lengths are defined through the number of integration points, N_p , it does not satisfy the third criterion. If an integration method fulfill all three criteria, it means that strain hardening can be represented, but only in the defined plastic hinge region. In search of an integration method that satisfy all criteria for strain-softening response, three plastic hinge integration methods was investigated by Scott & Fenves (2006).

3.2 Plastic Hinge Integration Methods

Midpoint Integration

Midpoint integration is based on that the integration points are located at the midpoint of each plastic hinge region, and the weights equals the length of the plastic hinges, as shown in Figure 3.3. This is the most accurate one-point integration method, but it has some drawbacks. Since the integration points are located at the center of the plastic hinge region, there will not be an integration point at the element ends where the largest bending moment occurs. I.e. criterion (1) is not satisfied. In addition, the midpoint integration method will only give exact integration for linear functions, which means that criterion (2) is not satisfied either. The midpoint integration is therefore only able to satisfy criterion (3).

Endpoint Integration

For the endpoint integration method, the integration weights are still equal to the plastic hinge lengths, as it was for the midpoint integration method. The integration points, on the other hand, are now located at the ends of the element. The major drawback of this method is that the order of accuracy is reduced by one, which means that it only have the ability to give exact results for integration of constant functions. Endpoint integration meets the criteria (1) and (3), but is not able to satisfy criterion (2).

Two-Point Gauss–Radau Integration

From the two methods discussed above, it is found that it is not possible to satisfy all of the three criteria by applying one-point integration in each of the plastic hinge regions,

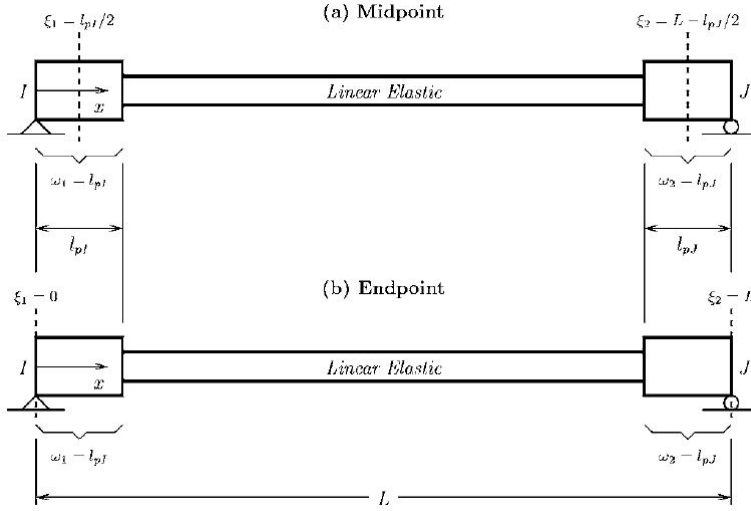


Figure 3.3: Midpoint and endpoint plastic hinge integration methods (Scott and Fenves (2006)).

and it is necessary to use at least one more integration point. Two-point integration methods as Gauss–Legendre and two-point Gauss–Lobatto are not sufficient as they are only able to either locate integration points at the element ends or give the desired level of element integration accuracy, and not both. However, the advantages of both these two-point integration methods are found in the Gauss–Radau quadrature. It has an integration point at one end of the element, and an accuracy of $2N_p - 2$, which is one order higher than Gauss–Lobatto. This results in an integration method that, with two integration points in each plastic hinge region, satisfies criteria (1) and (2).

The two-point Gauss–Radau integration rule places its integration points in the plastic hinge region as illustrated in Figure 3.4 a). The locations of the integration points are at $\{0, \frac{2}{3}\}$ and the corresponding weights are $\{\frac{1}{4}, \frac{3}{4}\}$. The use of two-point Gauss–Radau results in two noteworthy properties (Scott and Fenves (2006)). The first property is that when the plastic hinge lengths sums up to be equal to the element length, the integration rule becomes a four point integration scheme. The second property is that when the plastic hinge lengths are identical and equal to $L/2$, Simpson’s $3/8$ rule is obtained, and the accuracy is increased by one order.

Even though this method has its advantages, it does not satisfy all of the three criteria. The localized deformations are integrated over an length equal to the integration weight at the end point, $l_p/4$, and not the plastic hinge length, l_p , as criterion (3) states.

Modified Two-Point Gauss–Radau Integration

To make sure that the deformations are integrated over the whole plastic hinge lengths, the location of the integration points is modified. The modified two-point Gauss–Radau integration method have the integration points at $\{0, \frac{8}{3}l_{pI}, L - \frac{8}{3}l_{pJ}, L\}$ with the integra-

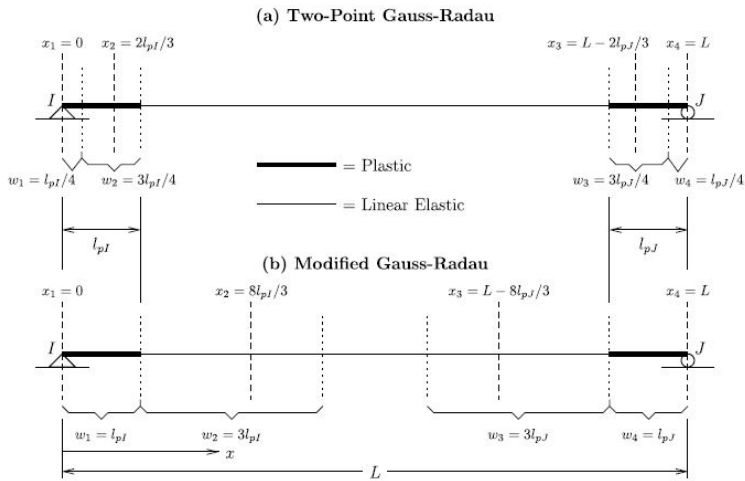


Figure 3.4: Gauss–Radau and modified Gauss–Radau plastic hinge integration methods (Scott and Ryan (2013))

tion weights $\{l_{pI}, 3l_{pI}, 3l_{pJ}, l_{pJ}\}$, as seen in Figure 3.4 b). In other words, the integration rule is applied over a length of $4l_{pI}$ and $4l_{pJ}$, instead of l_{pI} and l_{pJ} . With these modifications to the two-point Gauss–Radau integration method, all three criteria are satisfied, and strain softening in the plastic hinge regions is well represented.

Chapter 4

Hysteresis Models

For a reinforced concrete structure that is being exposed to an earthquake, nonlinear deformations often will develop. The nonlinear behavior arises from the degradation of the structure's stiffness, and reduction in the energy absorption capacity. To take such behavior into consideration a number of hysteresis models have been introduced. Such models need to be able to give information about the stiffness and resistance under any displacement history (Otani (1980)). Some of the models are more intricate, like the Q-Hyst and Takeda models, while the bilinear and elasto-plastic are examples of more simple models. A brief introduction to the most common models will be given in the following sections.

4.1 Elasto-Plastic Model

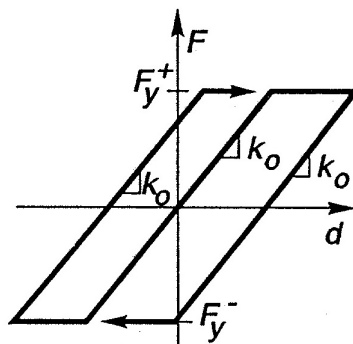


Figure 4.1: Elasto-plastic hysteresis model (Ruaumoko (2005)).

The elasto-plastic model uses an elastic force-deformation curve to represent the cracked-section behavior. No incremental stiffness is assumed upon yielding, and the unloading takes place with the same cracked-section stiffness. The hysteretic energy

dissipation is not provided by this model during small-amplitude deformations, and at the load reversal stage, the slope is not reduced at any point. The latter assumption is in contrast with results from cyclic testing on reinforced concrete connections. Even though the model has a poor correlation with observed hysteretic behavior, it is widely used for response history analysis because it is simple.

4.2 Bilinear Model

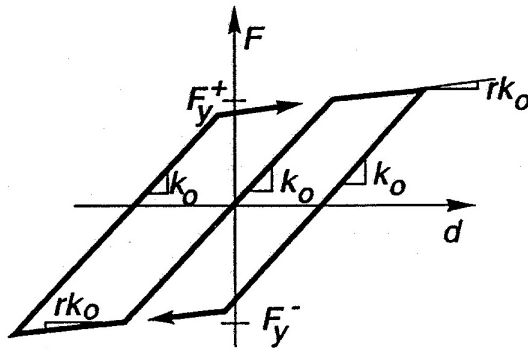


Figure 4.2: Bilinear hysteresis model (Ruaumoko (2005)).

Similar to the elasto-plastic model, the bilinear model uses an elastic force-deformation curve, but it additionally has a post-yield linear curve to take strain-hardening of the steel into account. This makes the model more realistic than the elasto-plastic model, but like the elasto-plastic model this model also fail to degrade the stiffness during load reversal.

4.3 Clough Model

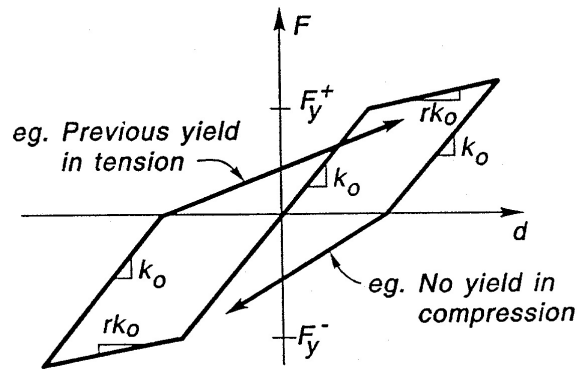


Figure 4.3: Clough hysteresis model (Ruaumoko (2005)).

To include degradation in the stiffness during load reversals, the Clough model was introduced. It operates on a bilinear primary curve, with a post-yielding branch. With a small modification from the elasto-plastic model, the Clough model is better suited to simulate the flexural behavior of reinforced concrete. With this model, the energy absorbed in each cycle beyond yielding, is less than what it is calculated to be with the elasto-plastic model. Clough's model has been widely used in nonlinear analysis because it includes strain-hardening while it at the same time is a simple model.

4.4 Takeda Model

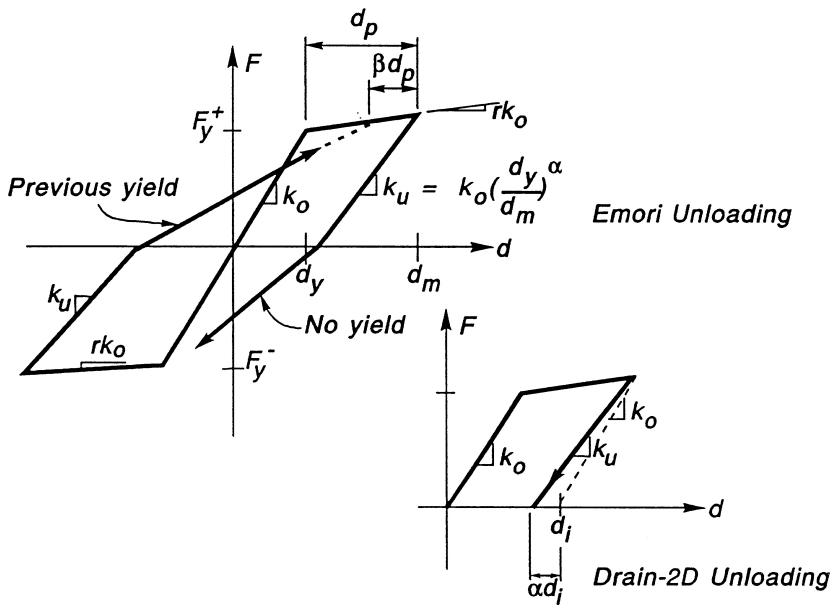


Figure 4.4: Takeda hysteresis model (Ruaumoko (2005)).

One of the most complicated models, with most variables needed is the Takeda model. It operates on a trilinear curve, which represents behavior for the uncracked, cracked and post-yielding stages. Once the section starts cracking, deformations will be nonlinear. This model also takes stiffness degradation into account, by reducing the stiffness by an exponential function of the previous maximum deformation.

4.5 Q-hyst Model

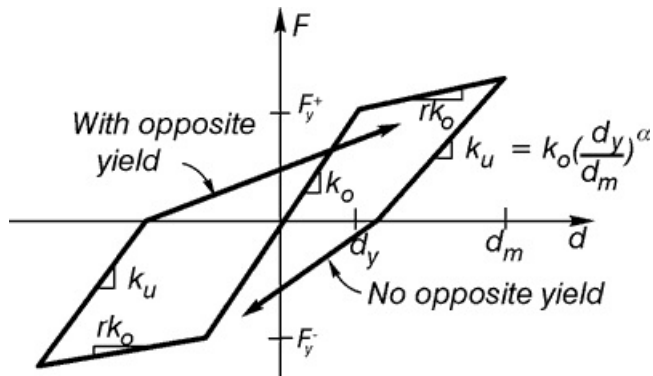


Figure 4.5: Q-hyst hysteresis model (Ruaumoko (2005)).

Like the Clough-model, the Q-hyst model (Saiidi and Sozen (1979)) consists of a bilinear primary curve with an ascending post-yielding branch. It takes account of stiffness degradation for both unloading and load reversal. Hysteretic energy dissipation during low-amplitude deformation is also considered in this model. The model is relatively simple, although it has produced satisfactory results compared to experimental data.

Chapter 5

Soil-Structure Interaction

Normally a dynamic response of a structure is evaluated with the assumption of the structure being fixed to the ground. However, this is not always a good assumption. Soil-structure interaction (SSI) becomes important under some conditions, and this chapter will highlight when it should be used, and some of the consequences using SSI.

When a structure is exposed to an earthquake, inertia forces will arise in the superstructure, which will deform the soil. In addition, the soil is deformed by the seismic waves. The total response can be divided into inertial and kinematic loading. The characteristics of the foundation, and the nature of the wave field governs the importance of each factor. During an earthquake the incoming waves is modified by the geometry, stiffness and damping characteristics of the soil deposit (Pecker (2008)). This modified motion is called the foundation input motion. Determining the free field motion includes several assumptions and is complicated to do, and no satisfactory solution is available to date.

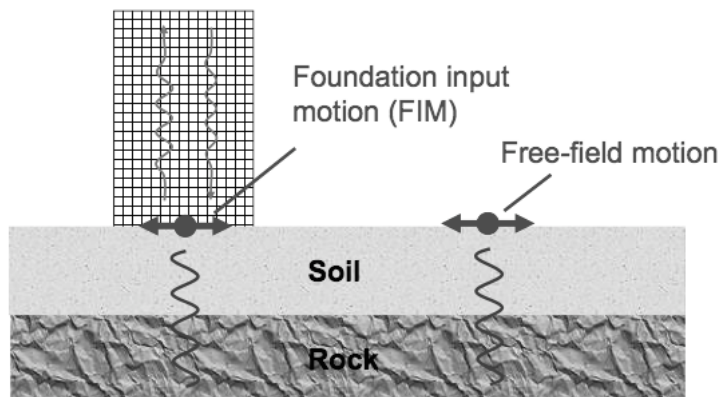


Figure 5.1: Illustration of foundation input motion and free-field motion.

Focusing on the motion around a structure and its foundation during an earthquake, it is normal that the deformation of the soil made by the seismic waves will make piles and foundation to move. This will eventually lead to movement of the supported structure. Reflections and scattering of the waves by the piles and the foundation results in differences between the motion of the foundation and the free field motion. Due to stress in the piles and foundations, curvatures and bending moments will develop. This is called kinematic interaction. The inertial interaction, on the other hand, is due to the internal forces developed in the superstructure and the moments at its base. Because of the motion at the foundation, oscillations are generated in the superstructure, which causes additional dynamic forces and displacement in the foundation, piles and the surroundings of the structure.

Through a simple illustration, the effect of SSI can be explained. Here, the model depicted in Figure 5.2 will be used. The figure illustrates a multistory structure. The foun-

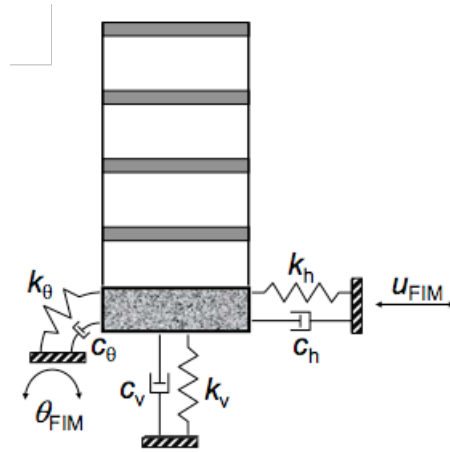


Figure 5.2: Illustration of SSI.

ation of the structure rests on the soil, and the interaction between the soil and the foundation is here modeled with springs and dashpots. The stiffness from the supporting mediums are represented by the spring, while the dissipated energy which comes from the soil and radiation of the seismic waves is given through the modeled dashpot. The material damping is neglected with respect to radiation damping for simplicity.

Pecker (2008) found the following equations:

$$\frac{1}{\tilde{\omega}^2} = \frac{1}{\omega_s^2} + \frac{1}{\omega_h^2} + \frac{1}{\omega_\theta^2} \quad (5.1)$$

$$\tilde{\xi} = \frac{\tilde{\omega}^2}{\omega_s^2} \xi + \frac{\tilde{\omega}^2}{\omega_h^2} \xi_h + \frac{\tilde{\omega}^2}{\omega_\theta^2} \xi_\theta \quad (5.2)$$

$$\tilde{u}_g = \frac{\tilde{\omega}^2}{\omega_s^2} u_g \quad (5.3)$$

where ω_s is the natural frequency of the fixed base structure, while ω_h and ω_θ represents the natural frequency of the rigid structure with a horizontal and rocking spring, respectively. $\tilde{\omega}$ is the natural frequency of the whole system, and is given by Equation (5.1).

From these equations, it is pointed out that the effect of soil-structure interaction is

- to decrease the frequency of vibration of the fixed base structure ($\tilde{\omega} < \omega_s$)
- to increase the damping ratio of the system with respect to the fixed base structure ($\tilde{\xi} > \xi$)
- to decrease the amplitude of the effective motion at the base of the structure ($\tilde{u}_g < u_g$)

5.1 Formulation of SSI Problem

A well known way to formulate a SSI problem in a general sense is within the framework of the finite element method. The mass, damping and stiffness matrices of the system is denoted by $[\mathbf{M}]$, $[\mathbf{C}]$ and $[\mathbf{K}]$, and the dynamic equilibrium equations are:

$$[\mathbf{M}]\{\ddot{\mathbf{u}}\} + [\mathbf{C}]\{\dot{\mathbf{u}}\} + [\mathbf{K}]\{\mathbf{u}\} = \{\mathbf{Q}_f\} \quad (5.4)$$

A decomposition of a SSI problem can be done as shown in Figure 5.3. The loading vector $\{\mathbf{Q}_f\}$ takes non-zero values along the boundary of the model. This is because the source of the earthquake focus normally is excluded within the finite element model. By omitting the structure and using the matrices related to the free field soil instead, the

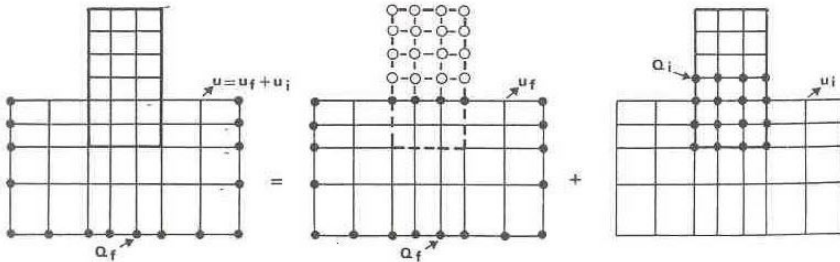


Figure 5.3: Decomposition of a SSI problem (Pecker (2008)).

equations of motion becomes:

$$[\mathbf{M}_f]\{\ddot{\mathbf{u}}_f\} + [\mathbf{C}_f]\{\dot{\mathbf{u}}_f\} + [\mathbf{K}_f]\{\mathbf{u}_f\} = \{\mathbf{Q}_f\} \quad (5.5)$$

The interaction displacement $\{\mathbf{u}_i\}$ is defined by

$$\{\mathbf{u}\} = \{\mathbf{u}_i\} + \{\mathbf{u}_f\} \quad (5.6)$$

and the equation satisfied by the interaction displacement is written as

$$[\mathbf{M}]\{\ddot{\mathbf{u}}_i\} + [\mathbf{C}]\{\dot{\mathbf{u}}_i\} + [\mathbf{K}]\{\mathbf{u}_i\} = -\{\mathbf{Q}_i\} \quad (5.7)$$

where

$$\{\mathbf{Q}_i\} = [[\mathbf{M}] - [\mathbf{M}_f]]\{\ddot{\mathbf{u}}_f\} + [[\mathbf{C}] - [\mathbf{C}_f]]\{\dot{\mathbf{u}}_f\} + [[\mathbf{K}] - [\mathbf{K}]]\{\mathbf{u}_f\} \quad (5.8)$$

From Equation (5.8) it is obtained that if there is a difference in stiffness or mass for the soil and the structure, there will be interaction. For the following sections, the structure that is considered will be without damping. That is, only the mass and stiffness contributes to the equations of motion.

Inertial Interaction

For a structure with an infinitely stiff foundation the last term from Equation (5.8) will vanish, and the load vector will be

$$\{\mathbf{Q}_i\} = [[\mathbf{M}] - [\mathbf{M}_f]]\{\ddot{\mathbf{u}}_f\} \quad (5.9)$$

The inertial force field that is generated in the superstructure arise from the forces at the base of the structure, $\{\mathbf{Q}_i\}$. From Equation (5.9) it is obtained that interaction only is generated by the inertial forces in the structure, which is called inertial interaction.

Kinematic Interaction

For an embedded structure that has a mass equal to the soil mass which also is equally distributed, i.e. and no mass above the ground, the term including the mass matrix will disappear from Equation (5.8). The remaining equation for the load vector is then

$$\{\mathbf{Q}_i\} = [[\mathbf{K}] - [\mathbf{K}_f]]\{\mathbf{u}_f\} \quad (5.10)$$

For this case, the forces will only appear if there is a difference in stiffness for the embedded structure and the soil. The interaction is due to the displacements imposed by the soil that the stiffness of the foundation tries to prevent. The mass does not matter in this case, as interaction is possible even if the mass for the structure and the soil differs or are the same. This interaction is termed kinematic interaction.

The relative displacement $\{\mathbf{u}\}$ can be defined as the sum of the kinematic and inertial interaction displacements, respectively $\{\mathbf{u}_{kin}\}$ and $\{\mathbf{u}_{iner}\}$. By introducing this definition, and substitute this relation into

$$[\mathbf{M}]\{\ddot{\mathbf{u}}\} + [\mathbf{K}]\{\mathbf{u}\} = -[\mathbf{M}]\{\mathbf{I}\}\ddot{u}_g \quad (5.11)$$

the following system of differential equations arises:

$$[\mathbf{M}_{Soil}]\{\ddot{\mathbf{u}}_{kin}\} + [\mathbf{K}]\{\mathbf{u}_{kin}\} = -[\mathbf{M}_{Soil}]\{\mathbf{I}\}\ddot{u}_g \quad (5.12)$$

$$[\mathbf{M}]\{\ddot{\mathbf{u}}_{iner}\} + [\mathbf{K}]\{\mathbf{u}_{iner}\} = -[\mathbf{M}_{Structure}][\{\ddot{\mathbf{u}}_{kin}\} + \{\mathbf{I}\}\ddot{u}_g] \quad (5.13)$$

where $[M] = [M_{Soil}] + [M_{Structure}]$. $[M_{Soil}]$ is the mass matrix of the soil substructure, and $[M_{Structure}]$ represents the mass matrix of the structure, while $\{I\}$ is the vector which gives the direction of the applied load and \ddot{u}_g is the base acceleration. For a per-

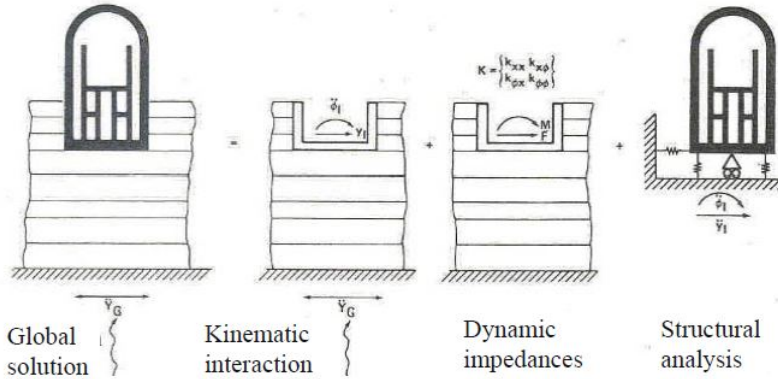


Figure 5.4: Illustration of superposition theorem (Kausel et al. (1978)).

fectly rigid structure, the global problem may be divided into three sub-problems by the use of the superposition theorem. It is necessary to (1) determine the motion of the massless rigid foundation that is subjected to the acceleration \ddot{u}_g , (2) determine the impedance matrix of the foundation and (3) calculate the dynamic response of the structure that is subjected to the kinematic interaction motion at its supports and connected to the foundation impedances. The three sub-problems are schematically depicted in Figure 5.4.

5.2 SSI in SeismoStruct

Application of SSI to a model in SeismoStruct (SeismoSoft (2014b)), may be done through the use of *link* element. It is necessary to define a structural node which initially coincides with the node where a soil spring is going to be applied. Soil spring is a simple way of modeling the effect of the ground flexibility on the structure. By applying such springs to the model, the structure's foundation may be modeled to be able to move and rotate, depending on the given properties of the springs. In SeismoStruct soil springs are modeled by link elements. The link element can then be given properties for six degrees-of-freedom, i.e. rotation and translation in x-, y- and z-directions. Each of these dofs must be given an independent response curve. In total there are 17 predefined response curves in SeismoStruct for describing the behavior of each of the six dofs in the link elements. Some of these curves are not very useful when it comes to describing behavior in soil, like the Takeda model and the Clough model. The Ramberg-Osgood model is, on the other hand, a suitable response curve for SSI. In addition to defining a response curve, damping may also be applied to the link element. The hysteretic response in nonlinear soil springs, however, generates damping which is often large enough that does not require separate damping elements.

Some changes to the model are necessary to be able to use link elements. Structural nodes were created at bottom node of the columns, and non-structural nodes were made to define the direction for the link elements. The bottom node of the columns were changed such that they are no longer fixed, but restrained against movement in z-direction and rotation about z. The SSI-nodes, on the other hand, were set to be fixed and the acceleration is applied at these nodes.

To control if the link elements work as expected, an analysis was first done with very stiff link elements. The link elements will then be so stiff that the column will be close to fixed at the base. The results from the analysis with and without SSI is depicted in Figure 5.5.

It is seen that both analyses gives exactly the same results, which indicates that the link elements work as expected.

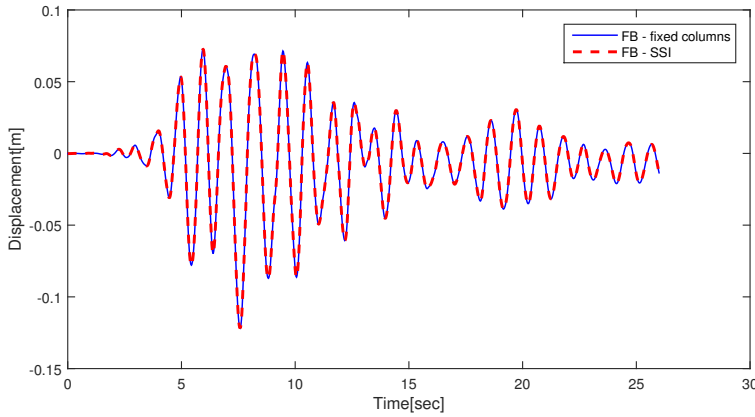


Figure 5.5: Time-displacement curve for the 3D-model with and without SSI. With high stiffness for the link elements.

Ramberg–Osgood Model

Some simple expressions may be used to find the soil spring stiffness, K , for a foundation with radius a over a uniform elastic soil with shear modulus G , mass density ρ and Poisson's ratio ν . As presented by Wolf (1988), the horizontal spring stiffness is given by Equation (5.14)

$$K_h = \frac{8Ga}{2-\nu} \quad (5.14)$$

while the rocking spring stiffness is found by Equation (5.15)

$$K_\theta = \frac{8Ga^3}{3(1-\nu)} \quad (5.15)$$

For a $1.5m \times 1.5m$ foundation the equivalent radius will be $a = \sqrt{\frac{1.5 \times 1.5}{\pi}} = 0.85m$. Usu-

ally the shear modulus of the soil is somewhere between 0.01 to 0.001 times $G_{concrete}$. Here, the relation in Equation (5.16) is used for soil, where τ is the shear strength of the soil.

$$G = 1000 \times \tau \quad (5.16)$$

With a shear strength of $\tau = 10kPa$, it is found that the shear modulus for the soil is $10000kPa$. The horizontal and rocking stiffness is calculated below by inserting G and a in Equation (5.14) and (5.15).

$$K_h = \frac{8 \times 10000 \times 0.85}{2 - 0.4} = 42500kN/m$$

$$K_\theta = \frac{8 \times 10000 \times 0.85^3}{3(1 - 0.4)} = 27294kNm/rad$$

In SeismoStruct, several parameters must be defined for the response curves. For the Ramberg-Osgood model, four parameters are needed.

Table 5.1: Parameters that must be defined in SeismoStruct for the Ramberg–Osgood model (SeismoSoft (2014a)).

Parameters	Default value
Yield strength - F_y	500
Yield displacement - D_y	0.0025
Ramberg-Osgood-parameter - γ	1.5
Convergence limit for the Newton-Raphson procedure - β_1	0.001

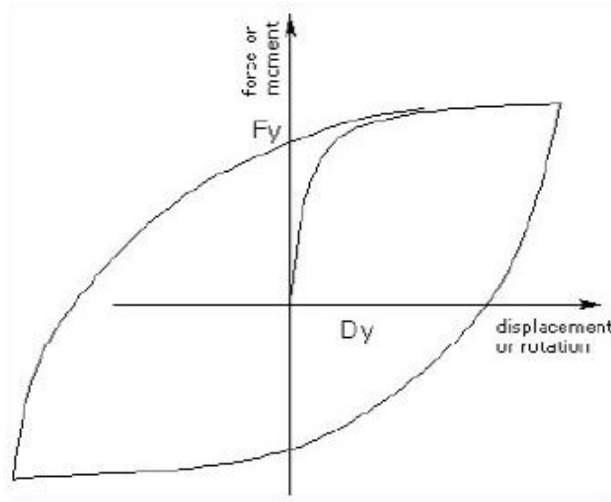


Figure 5.6: Ramberg–Osgood hysteresis model (SeismoSoft (2014a)).

The loading curve is given by

$$\frac{D}{D_y} = \frac{F}{F_y} \left(1 + \left| \frac{F}{F_y} \right|^{(\gamma-1)} \right) \quad (5.17)$$

As seen in Figure 5.7, the curve changes with different γ s. For a higher value of γ , the curve approaches the elasto-plastic curve.

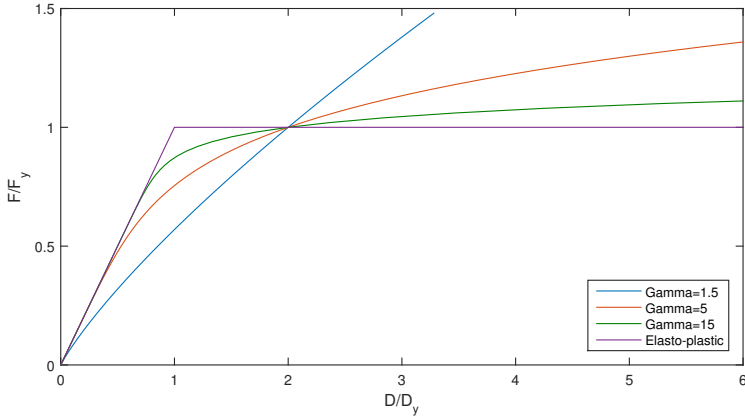


Figure 5.7: Force-displacement curve for Ramberg-Osgood with different γ s.

For $\gamma > 1$, the tangent of the curves near the origin are approximately the same. The slope of the tangent is given by $K = \frac{F_y}{D_y}$. The yield strength, F_y , is equal to the lateral capacity of the foundation, which is defined as

$$F_y = \tau \times A \quad (5.18)$$

where A is the area of the foundation, and τ is the shear strength of the soil. The area of the foundation is $2.25m^2$, and $F_y = 1 \times 10 = 22.5kN$. With the data given above, the displacement can be found by

$$D_y = \frac{F_y}{K}$$

With the horizontal stiffness calculated above, D_y becomes

$$D_{y,h} = \frac{22.5kN}{42500kN/m} = 5.294 \times 10^{-4} m$$

Usually horizontal springs becomes nonlinear, but rocking springs stays linear. Hence, the rocking springs are modeled with linear hysteretic curves with the stiffness, K_θ .

A summary of the parameters used for the Ramberg-Osgood model in SeismoStruct are given in Table 5.2.

Table 5.2: Parameters used for the Ramberg–Osgood model.

Parameters	Value
F_y	22.5
$D_{y,h}$	0.0005294
γ	15
β_1	0.001

Chapter 6

Pushover Analysis

A pushover analysis is a nonlinear static analysis by which the seismic deformations of structure is estimated using nonlinear techniques (Shinde et al. (2014)). During the analysis, typically a horizontal load is applied at the top of a structure incrementally, and the corresponding displacement and force are plotted at each increment until it reaches a target displacement, or until the structure collapses. The load represents the inertial forces and the target displacement is the maximum expected displacement during the earthquake. In the analysis done in this thesis, the load applied for each increment results in a displacement of $0.02m$.

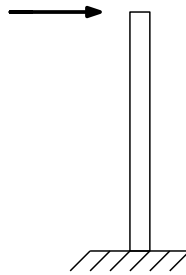


Figure 6.1: Illustration of pushover analysis.

6.1 Effect of Change in Number of Elements

To verify that the elements behave the way that they are predicted to, a pushover analysis was done prior to the analyses where excitation was applied to the structure. The analysis was done for DB, FB and PH elements. It turned out that SeismoStruct did not give the expected results. For all elements, the column has been designed with shear reinforcement consisting of $\text{Ø}6c150$, and longitudinal reinforcement of $8\text{Ø}14$. All of the element types have been modeled with 3% Rayleigh damping here, and for all analyses

later in the thesis. The displacement target was set to $2m$, and the columns have been modeled with 1, 2, 4 and 6 elements.

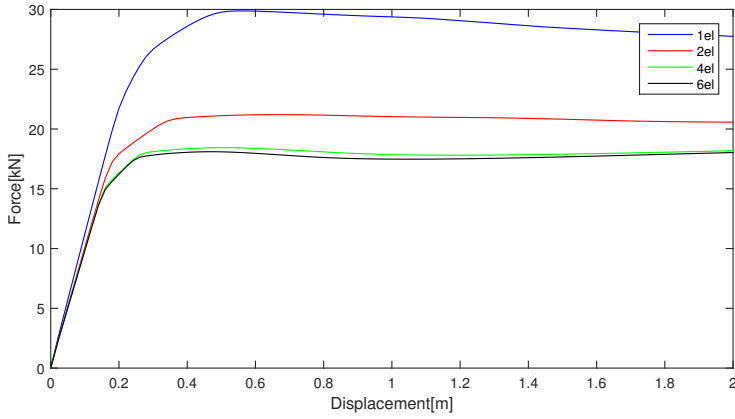


Figure 6.2: Force-displacement curve for different number of DB elements.

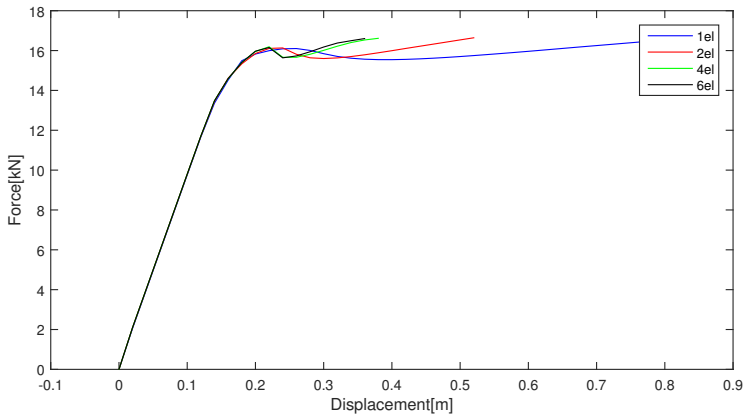


Figure 6.3: Force-displacement curve for different number of FB elements.

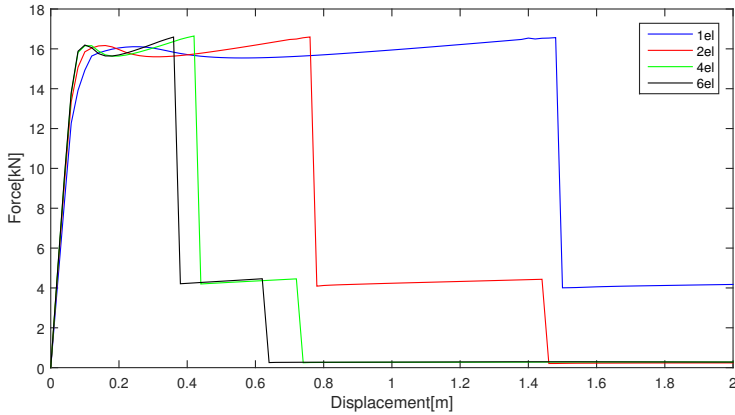


Figure 6.4: Force-displacement curve for different number of PH elements.

For the DB elements, the force-displacement curve from the pushover analysis is shown in Figure 6.2. For all elements, the behavior is approximately the same up to $0.2m$. After that point, the behavior varies with the number of elements; few elements requires a higher force to increase the displacement than a higher number of elements does.

By using FB elements, it is observed from Figure 6.3 that the analysis terminates for a force equal to $16.6kN$. On the contrary to the DB analysis, where all of the analyses reaches the target displacement, it is not reached for the FB element. All analyses reaches a point where the program no longer is able to apply the next load step. The value of the displacement where the structure collapses varies with the number of elements; the less elements, the higher displacement before the column breaks.

At last, it is seen from Figure 6.4 that by changing number of elements for PH elements, the results are varying a lot. This may probably be because of plastic hinges are formed in the ends of each element. I.e. for a column consisting of 6 elements, plastic hinges may form at twelve places, while only two plastic hinges will form in a column modeled with one element. As for the FB elements, the number of PH elements decides at which displacement the column collapses; the fewer elements, the higher displacement is reached.

6.2 Effect of Different Spacing in Stirrups

6.2.1 Unidirectional Pushover Analysis

A pushover test was also done for different spacing between the stirrups. For this test, the column is modeled with the same longitudinal reinforcement as above, and the same diameter for the shear reinforcement. The only variable has been the spacing, which was set to $50mm$, $150mm$, $300mm$ or $1000mm$. All three element types have been used, and the results from the analyses are shown in Figure 6.5, 6.6 and 6.7.

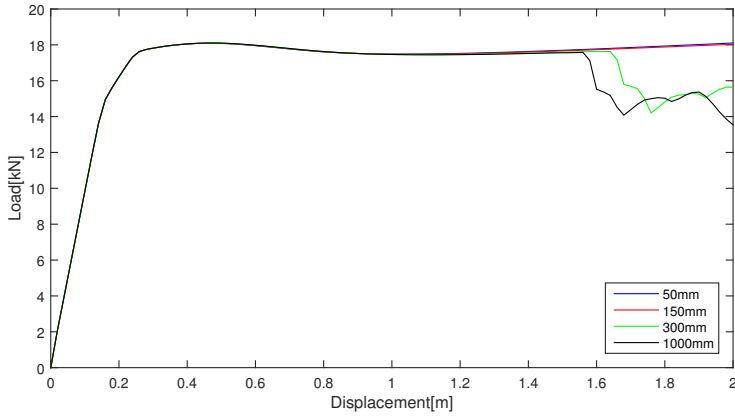


Figure 6.5: Load-displacement curve for a column consisting of a DB element with different spacings in stirrups.

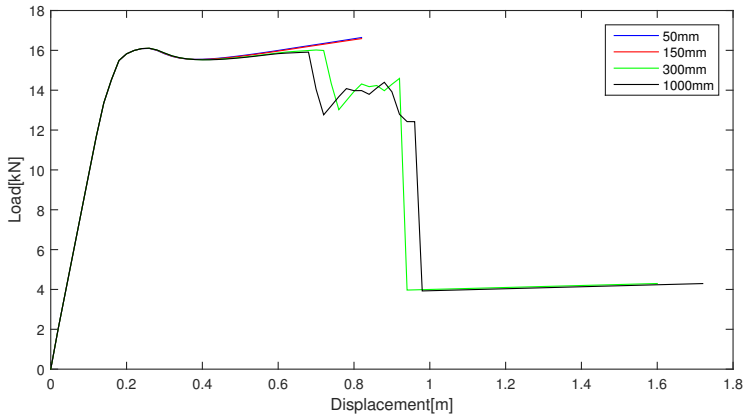


Figure 6.6: Load-displacement curve for a column consisting of a FB element with different spacings in stirrups.

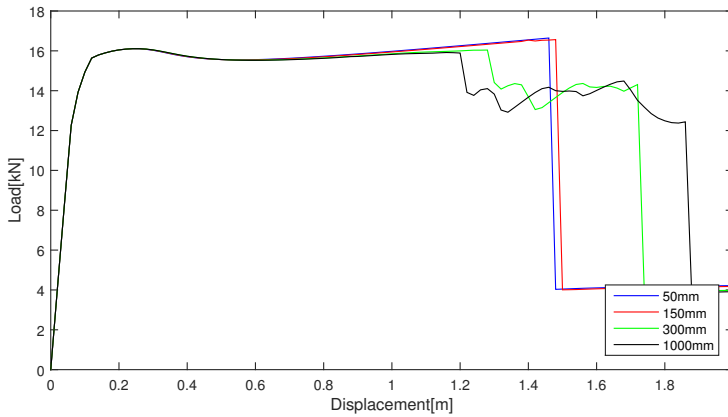


Figure 6.7: Load-displacement curve for a column consisting of a PH element with different spacings in stirrups.

It is noteworthy that the analysis for the FB element terminates earlier for 50mm and 150mm spacing, than for 300mm and 1000mm spacing. For all spacings, the behavior is almost the same until a displacement of 0.7m. At this point the structure almost collapses for a spacing of 300mm and 1000mm. For a spacing of 50mm and 150mm, on the other hand, the analyses terminates for a displacement of 0.8m. For the DB element, the analysis is completed for all spacings. The behavior is also here almost the same up to the point where the displacement is 0.7m. After this point, the load required to increase the displacement is considerable lower for the element with a spacing of 300mm and 1000mm, than for 50mm and 150mm. PH elements yields at the same point as the force-based elements does, but as seen in Figure 6.7 the elements can resist a larger displacement than the FB elements.

6.2.2 Bidirectional Pushover Analysis

An additional load has been applied to the column to see if the results are influenced differently under bidirectional loading. The load which was applied in y-direction is 30% of the load in x-direction. The target displacement is still set to be 2m in x-direction. Figure 6.8 shows that the extra load does not give any particular change for the column modeled with DB elements. On the contrary, the FB element is more affected by the additional load. The analyses are now running until the target displacement is reached for all of the cases, as seen in Figure 6.9. Additionally can it be seen that all of the analyses makes the column collapse after reaching a displacement of 0.8m, and not only for the two largest spacings. The PH elements are also affected by the additional load, as shown in Figure 6.10. The behavior is very similar to the force-based elements, and the main difference is still that the PH elements lasts longer before they break.

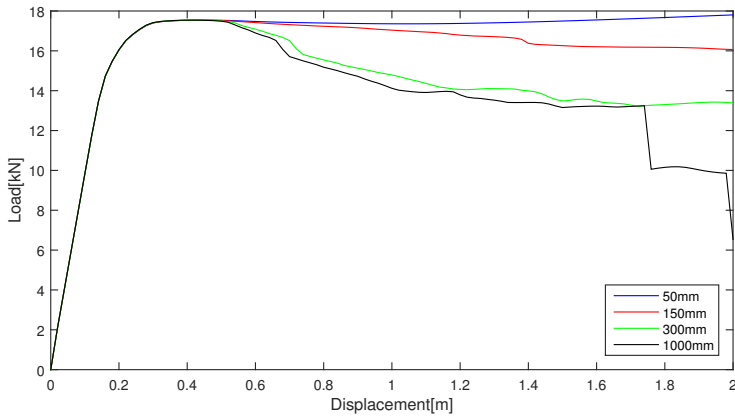


Figure 6.8: Load-displacement curve for a column consisting of a DB element with different spacings in stirrups, from bidirectional pushover analysis.

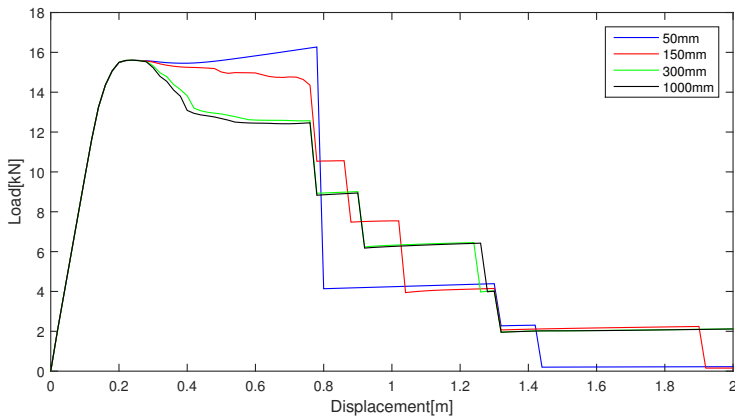


Figure 6.9: Load-displacement curve for a column consisting of a FB element with different spacings in stirrups, from bidirectional pushover analysis.

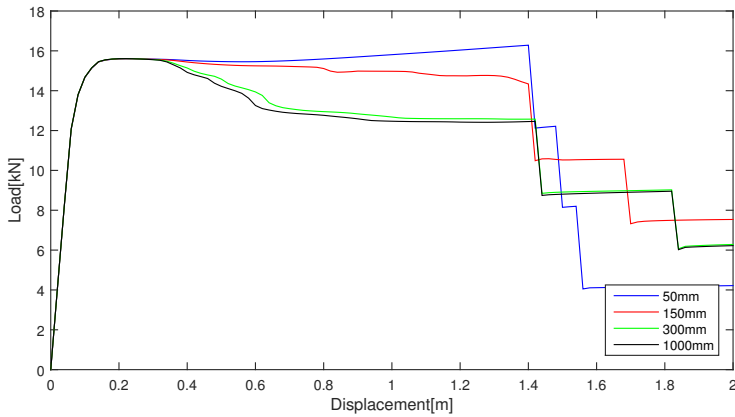


Figure 6.10: Load-displacement curve for a column consisting of a PH element with different spacings in stirrups, from bidirectional pushover analysis.

For comparison, the results from unidirectional and bidirectional pushover analyses are plotted in the same graph in Figure 6.11. By applying a force in y-direction in addition to the pre-existing force in x-direction, the column shows some changes in the load-displacement curve. The column yields for a slightly lower force than for the unidirectional case, and collapses when a displacement of $0.8m$ is reached.

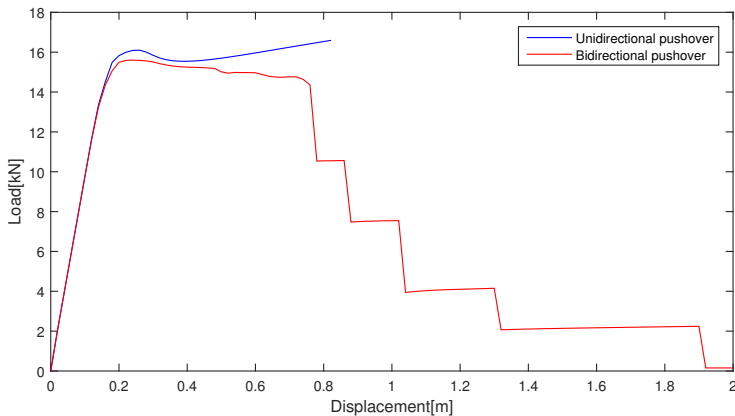


Figure 6.11: Results from uni- and bidirectional pushover analyses for a column consisting of a FB element and a spacing of $150mm$.

By varying the spacing between the stirrups, the confinement factor of the concrete is influenced. For the Mander concrete model, the confining pressure is assumed to be constant throughout the entire stress-strain range. The ratio between the confined and unconfined compressive stress of the concrete, is defined as the confinement factor. This factor is used to scale up the stress-strain relationship throughout the entire strain

range (SeismoSoft (2014a)).

For the same unconfined strength, f'_c , the stirrup spacing changes the confinement factor. The confinement factors for the different spacing are listed in Table 6.1. The table shows that the closer the stirrups are placed, the higher is the confinement factor. In Eurocode 2, section 3.1.9 (Standard Norge (2008)), a description of how confinement affects the properties of the concrete is given: "Confinement of concrete results in a modification of the effective stress-strain relationship: higher strength and higher critical strains are achieved". This means that when the stirrups are placed with 50mm spacing, the strength of the concrete is effectively higher than when the spacing is 1000mm. This is corresponding to the values obtained in SeismoStruct.

Table 6.1: Confinement factors for the different spacings.

Spacing	Confined	Unconfined
50mm	1.4590	1.0000
150mm	1.1058	1.0000
300mm	1.0094	1.0000
1000mm	1.0000	1.0000

Chapter 7

Model Verification

7.1 Experimental Background

The Joint Research Centre has done many seismic experiments on behavior of different structures. To see if the result SeismoStruct gives out is accurate, an examination of a one-story RC industrial building was done. The structure was made of cast-in-situ beams and columns, and consists of two two-bay frames, connected by a slab. It was designed for a dead load of 27 kN/m^2 , which includes the weight of the slab. The dimensions of the columns were $300\text{ mm} \times 300\text{ mm}$, and the beams were $600\text{ mm} \times 300\text{ mm}$. The thickness of the slab was 150 mm . A picture of the prototype can be seen in Figure 7.1, while the geometry is shown in figure 7.2



Figure 7.1: Picture of the prototype (Ferrara and Negro (2004)).

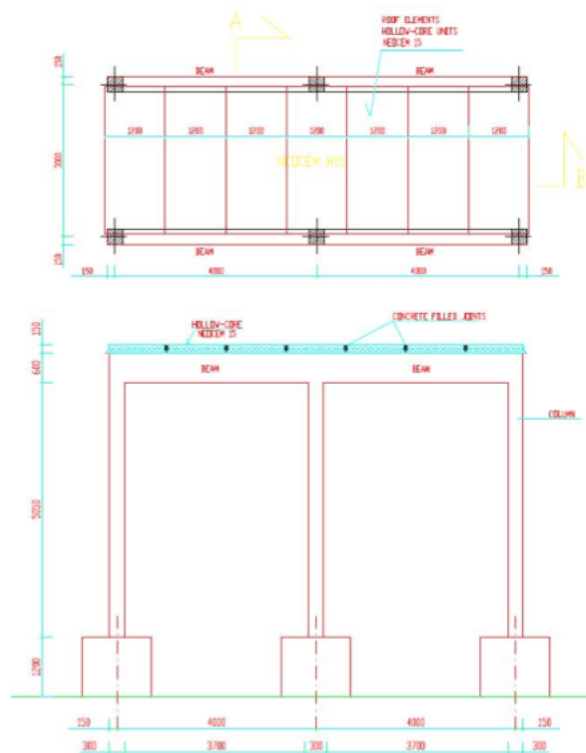


Figure 7.2: Geometry of the prototype (Ferrara and Negro (2004)).

The longitudinal reinforcement pattern can be seen in Figure 7.3, and consists of $8\text{Ø}14\text{mm}$ throughout the whole length columns. The transverse reinforcement varies with the length of the column. In the critical zones, 1m from the top and bottom, the stirrups were placed with a spacing of 50mm , while in the non-critical region, a spacing of 150mm was used. The dimensions of the bars were 6mm , and the stirrups were designed with 4 legs in both directions. The purpose of the transverse reinforcement is both confinement and shear forces. For the beam, the experiment rapport does not provide any specific information. It is only known that the beam is reinforced such that plastic hinges will form in the columns, and the reinforcement of the beam is therefore set to approximately 10 times the amount of the reinforcement in the columns.

The materials used for building the prototype were tested prior to the experiment. The concrete was tested by cube specimen tests, and the cylindrical mean compressive strength was found to be $f_{cm} = 42.74\text{MPa}$ for the columns, and $f_{cm} = 47.20\text{MPa}$ for the beams. The steel in the longitudinal reinforcement had a yielding strength of $f_y = 550\text{MPa}$ and tensile strength of $f_t = 657\text{MPa}$

Hydraulic jacks were used to apply the horizontal displacements to the structure. In Figure 7.1, the jacks are seen connected to the beam at the right. In order to get the wanted load on the slabs, vertical jacks were also used during testing. The load applied through the vertical jacks were 600kN , including the slab self weight. The position of

both the horizontal and vertical jacks is depicted in Figure 7.4.

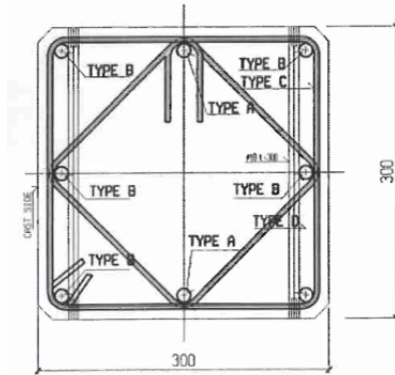


Figure 7.3: Longitudinal reinforcement pattern (Ferrara and Negro (2004)).

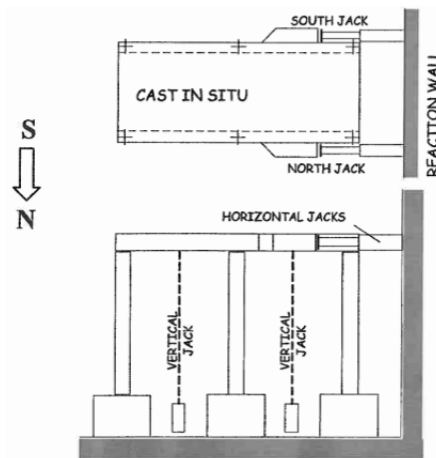


Figure 7.4: Positioning of the hydraulic jacks (Ferrara and Negro (2004)).

The seismic ground motion that the structure was exposed to was simulated through an artificial accelerogram. In Eurocode 8 (Standard Norge (2014)), several response spectrum is presented. The response spectrum used in the test was generated automatically to be similar to what is given for a subsoil 2B. The accelerogram is shown in Figure 7.5, and will be referred to as the base case ground acceleration in this thesis. Displacement time-histories were made with different scaling; 0.05g, 0.32g, 0.64g and 0.80g. To calibrate and test the devices, the 0.05g time-history was used, and it was not further used in the test, nor included in the following analyses. The three displacement time-histories used during the test is shown in Figure 7.7

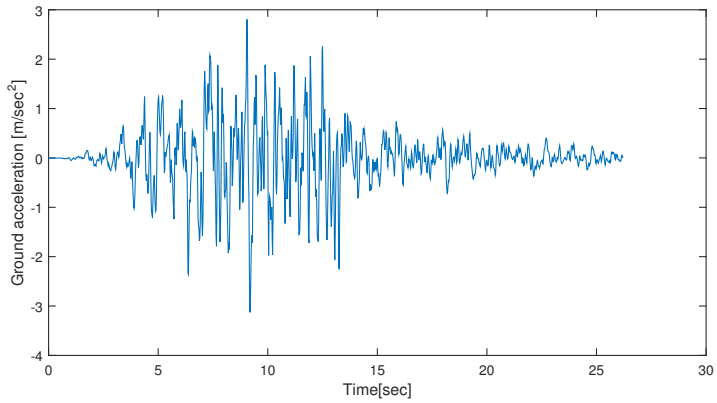


Figure 7.5: Artificial accelerogram.

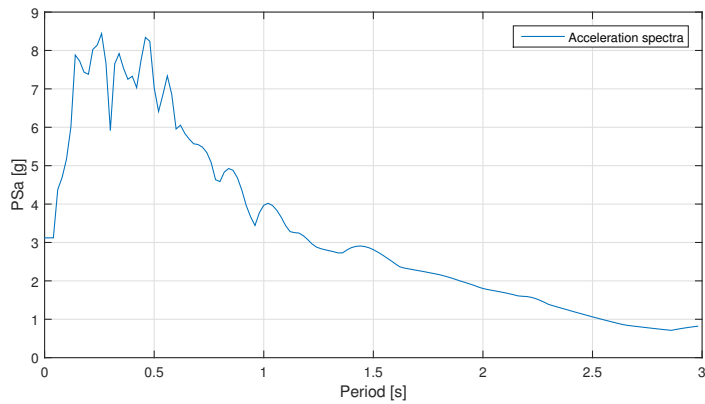


Figure 7.6: Response spectrum for acceleration in Figure 7.5.

From the displacement time-histories it is observed that the ground motion of $0.32g$ gives few irregularities in the displacement, and is said to yield an elastic response. This is depicted in Figure 7.7 a). In Figure 7.7 b) the displacement becomes more irregular, i.e. some inelastic response. For the last case seen in Figure 7.7 c), the response is clearly inelastic.

7.2 Modeling in SeismoStruct

7.2.1 2D-Model

The model is made the same way as it was done in Gharakhanloo's thesis (2014), where analyses with FB elements, DB elements and plastic hinge elements for each intensity of the ground motion has been done. For the columns, the number of integration points, length of plastic hinge and number of elements for the different element types are listed in Table 7.1.

Table 7.1: Values used to create the models (Gharakhanloo (2014)).

Element type	Number of integration points	Number of elements	Length of plastic hinge
DB	2	6	1.146m
FB	5	1	-
FB plastic hinge	2	4	0.573m

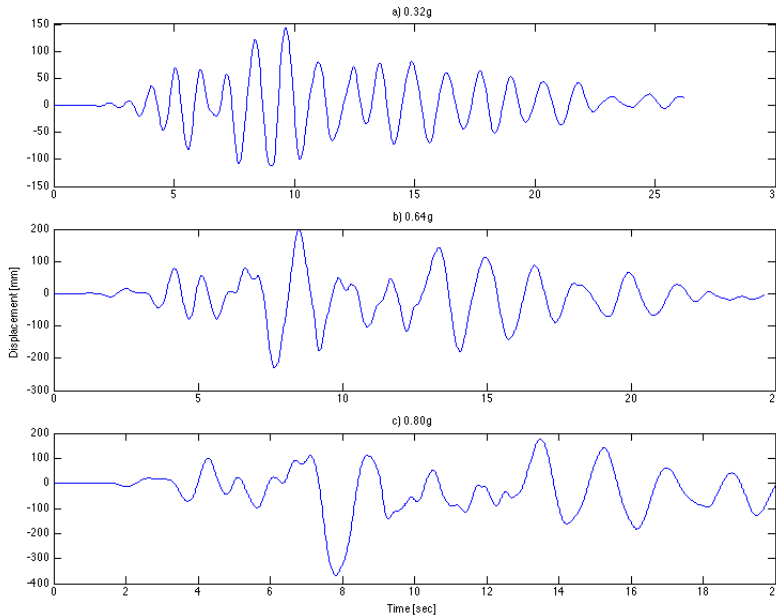


Figure 7.7: Time-histories for respectively 0.32g, 0.64g and 0.80g.

The plastic hinge length for the beams is not specified, but it is assumed over-strength in the beam compared to the column. For the DB elements, it is used 4 elements in the beam, while 2 elements are used for both the FB elements and the FB plastic hinge elements. For the latter element type, the SeismoStruct default value for plastic hinge

of 16.67% is kept unchanged. From the analyses done by Gharakhanloo (2014) it was found that FB and plastic hinge elements gave the best results, and due to the lowest number of elements needed, FB elements is used for all analyses in the last chapter in this thesis.

In SeismoStruct it is necessary to choose a proper material model for the materials used in the model. For the steel reinforcement, the Menegotto-Pinto model has been used, while the Mander model has been used for the concrete.

In Gharakhanloo (2014), the analyses are run as static time-history analyses. The model was subjected to a displacement in the top of the column, the same way as it was done in the experiment. The displacement is a pseudo-dynamic displacement which is found from performing a preliminary dynamic analysis of the prototype. In this thesis it is necessary to apply the earthquake through a ground acceleration. The analyses will therefore change to dynamic time-history analyses. The ground motion shown in Figure 7.5 is applied at the bottom node of the columns, as shown in Figure 7.8.

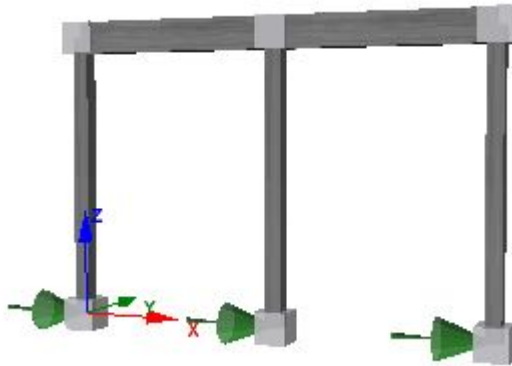


Figure 7.8: 2D-model in SeismoStruct, with acceleration applied at the bottom of each column.

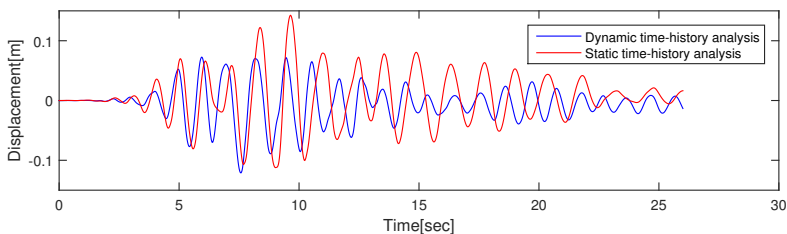


Figure 7.9: Displacements from static and dynamic analyses for the 2D-model with FB-elements.

It is worth mentioning that by applying the acceleration at the base nodes of the structure, instead of displacements at the top node of the columns, the measured displacement differs. The displacements from the static and dynamic time-history analyses

are compared in Figure 7.9. The displacements used in the experiment was found by an analysis done in a program like SeismoStruct. It was necessary to find pseudo-displacements due to the use of hydraulic jacks in the experiment, instead of a shaking table. The report does not give information about which program that was used to find the displacement, nor the choice of what kind of elements, number of elements, etc. For the dynamic analysis, the acceleration is the same as the one used to find the displacement used in the static analysis, but the output for the displacements does not correspond. This must be due to choices made when making the model. This will not be discussed any further in this thesis.

7.2.2 3D-Model

Due to symmetry of the building, it is only necessary to model one frame when the ground motion is applied in one direction, while the full 3D-model is required for the analyses where excitation is applied en both x- and y-direction. The 3D-model consist of two identical frames, with constraints in form of master-slave nodes in the top of the columns. These master and slave nodes represents the slab between the two frames. A screen shot of the model in SeismoStruct can be seen in Figure 7.10.

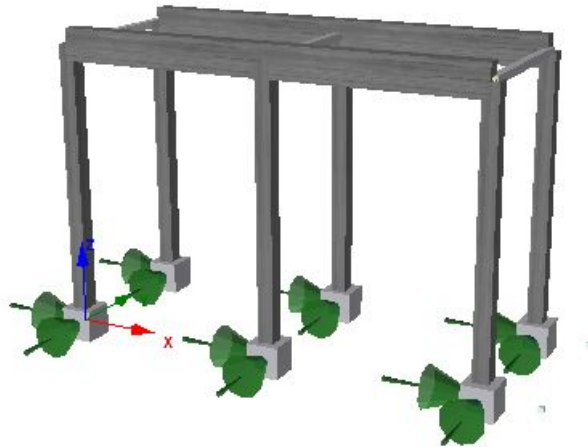


Figure 7.10: Screen shot of the model in SeismoStruct.

For the 3D-model, the acceleration in x-direction is the same as for the 2D-model. In y-direction the acceleration applied is 30% of what it is in x-direction, the same way as for the pushover analysis. The difference in displacement for uni- and bidirectional excitation is minimal. This is shown in Figure 7.11, and it is seen that the maximum displacement in x-direction is slightly bigger for the bidirectional case, than when the excitation is applied in one direction. The largest forces will always occur in x-direction, and the forces and displacement presented in this thesis are obtained in that direction.

The moments, on the other hand, will be largest about the y-axis, and there are these moments that will be compared.

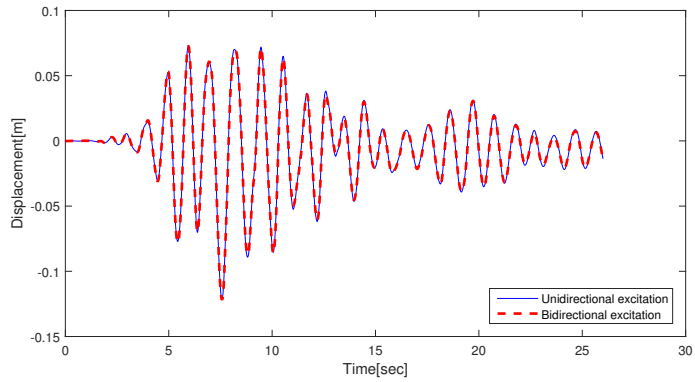


Figure 7.11: Displacement for the 3D-model with excitation in one and two directions.

Chapter 8

Results

8.1 Effect of Change in Spacing in Stirrups

In the experiment, the structure had reinforcement as described earlier in Chapter 7, and the columns were strengthened at the base and top by increasing the amount of stirrups. To see what effect this has on the structure, analyses have been done with different spacing in the stirrups. These analyses are done with FB elements, and a spacing of 50mm , 150mm , 300mm and 1000mm . The reinforcement in the beams is unchanged in all of the analyses. The results from changing the spacing between the stirrups are shown in Figure 8.1. From the figure, it is easy to see that the effect is non-existing. All analyses gives the same displacements, and they are not depending on the spacing at all. The maximum displacement that is reached during the analyses, is approximately 0.12m . From the pushover analysis, it was found that the FB elements could withstand a displacement of 0.70m before the column collapsed.

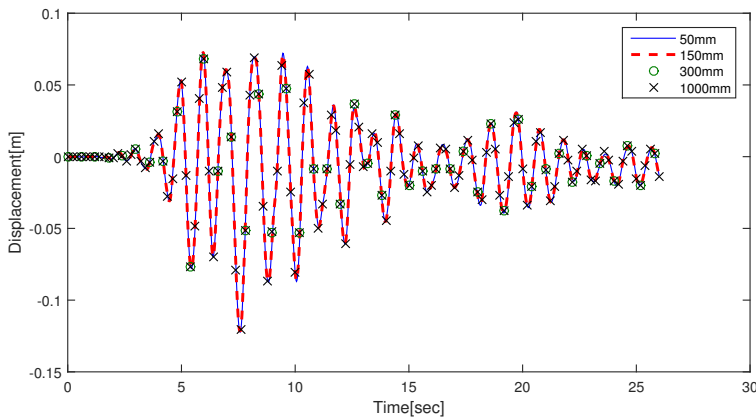


Figure 8.1: Time-displacement curve for different spacing in stirrups for base case acceleration.

One theory is that the size of the force that is obtained in each column is so low that the shear reinforcement is not necessary, and hand calculation has been done to see if this may be the reason why the displacement remains unchanged.

8.1.1 Hand Calculation of Shear Force

The hand calculation has been done as described in Eurocode 2, chapter 6.2 (Standard Norge (2008)). The following data is given by the dimensions and properties of the cross-section of the columns:

$$\begin{aligned} A_{sl} &= 8 \times \pi \times 7^2 = 1231.5 \text{ mm}^2 \\ A_c &= 300 \times 300 = 90000 \text{ mm}^2 \\ f_{sd} &= 434 \text{ MPa} \\ f_{ck} &= 40 \text{ MPa} \\ c_{nom} &= 25 \text{ mm} \\ b_w &= 300 \text{ mm} \end{aligned}$$

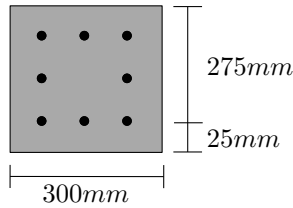


Figure 8.2: Cross-section of the columns.

With these values, the dimensioning shear force is calculated by

$$V_{Rd,c} = [C_{Rd,c} k (100 \rho_l f_{ck})^{1/3}] b_w d \quad (8.1)$$

where

$$k = 1 + \sqrt{\frac{200}{d}} = 1 + \sqrt{\frac{200}{275}} = 1.853 \leq 2.0 \quad (8.2)$$

$$\rho_l = \frac{A_{sl}}{b_w d} = \frac{1231.5}{300 \times 275} = 0.0149 \leq 0.02 \quad (8.3)$$

$$C_{Rd,c} = \frac{0.18}{\gamma_c} = \frac{0.18}{1.5} = 0.12 \quad (8.4)$$

By inserting the values above into Equation (8.1), the value for the dimensioning shear force is found to be

$$V_{Rd,c} = 0.12 \times 1.853 \times (100 \times 0.0149 \times 40)^{1/3} \times 300 \times 275 = 71.7 \text{ kN} \quad (8.5)$$

This means that for a shear force less than 71.7 kN, the stirrups are not necessary. From the analyses the maximum total shear force observed is approximately 215 kN, which is

shown in Figure 8.3. Divided on the six columns, a force of about $36kN$ occurs in each column. This is much less than the value that requires shear reinforcement. Later in the thesis, the value from only one of the column is discussed and compared for different cases. The base shear measured in the left column is therefore shown in Figure 8.4, and will be used for comparison later.

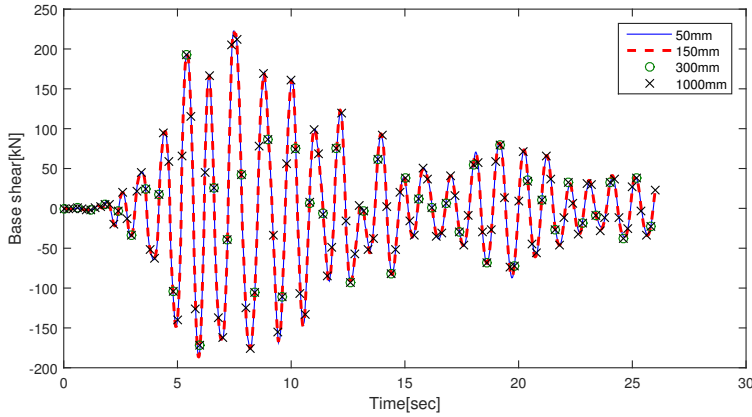


Figure 8.3: Total base shear against time for different spacing in stirrups for base case acceleration.

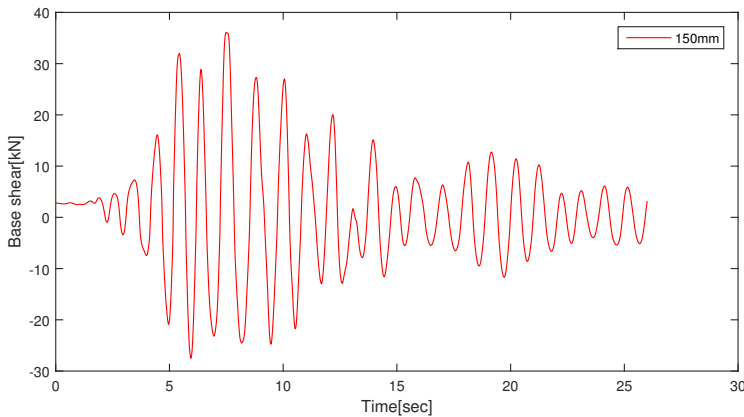


Figure 8.4: Base shear against time for one column with 150mm spacing for base case acceleration.

The acceleration was multiplied by a factor of 5 and 10 to see if the displacement then would be affected by changing the space between stirrups.

By multiplying the base case acceleration by 5, the displacement starts to show some difference for the different spacings. The displacements and forces for $5\times$ acceleration is depicted in Figure 8.5 and 8.6.

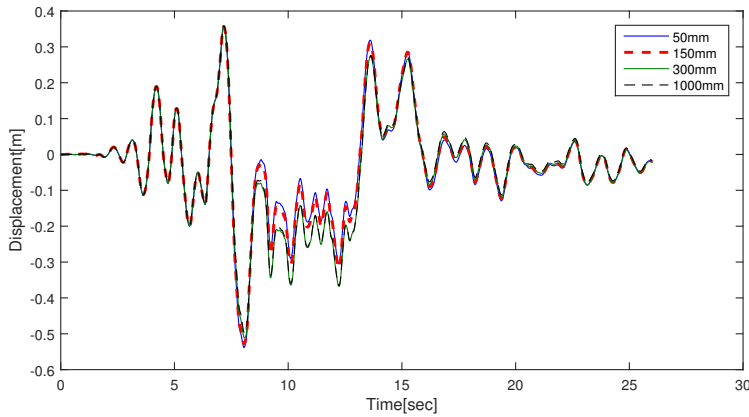


Figure 8.5: Displacement against time for different spacing in stirrups, with $5\times$ acceleration applied.

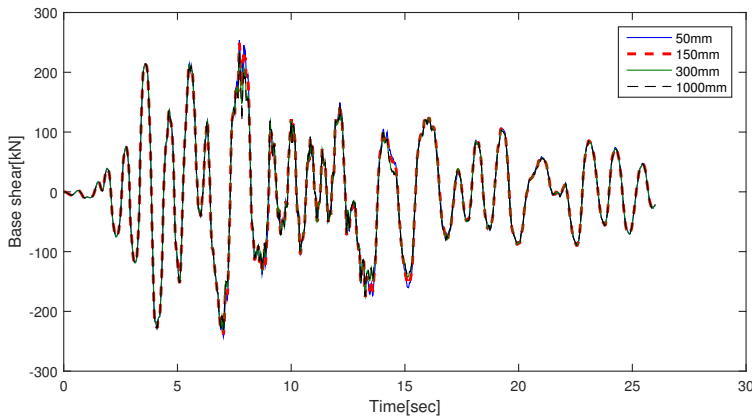


Figure 8.6: Total base shear against time for different spacing in stirrups, with $5\times$ acceleration applied.

The maximum force that is observed is slightly higher than earlier, and by dividing 250 kN on the six columns, the force in each column have now reached a maximum of about 42 kN . The force is still far from the calculated force when shear reinforcement becomes necessary, but as seen in Figure 8.5 the increase of acceleration results in some difference in the displacement for the different spacings.

To see what will happen in a even more extreme case, the acceleration was at last multiplied by 10. The results are shown in Figure 8.7 and 8.8. As mentioned earlier, the response shows a nonlinear response for larger accelerations, which is seen in both Figure 8.5 and 8.7. For the $10\times$ acceleration, the displacement is clearly differing for the four spacings. It seems like the two stiffest columns, collapses after approximately 13

seconds, and gets a really large displacement, and then reaches a point where the analyses no longer are able to continue at 20 seconds. The forces obtained in the columns are almost the same for all four cases, until the point where the two stiffest columns collapse. From Figure 8.8 it is seen that the forces for these two columns are quite low for the time interval 13 to 20 seconds. With a large displacement obtained at the same time as a low force, it is likely to believe that the columns collapse. In the time interval from 15 to 20 seconds, a displacement of about 3m takes place, while the force in this interval does not show any drastic change. As the force has a quite small change, compared to earlier in the analysis, at the same time as a major increase of the displacement, the stiffness must have been reduced.

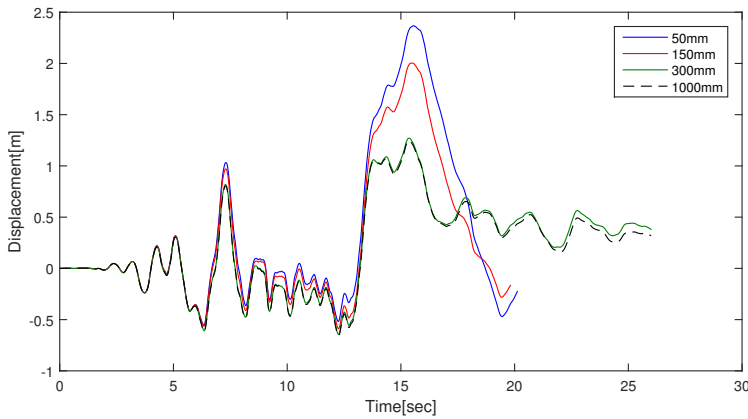


Figure 8.7: Displacement against time for different spacing in stirrups with 10× acceleration applied.

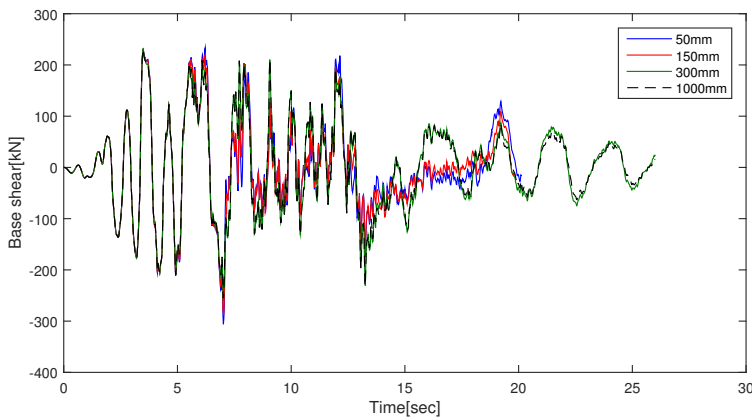


Figure 8.8: Force against time for different spacing in stirrups with 10× acceleration applied.

8.2 Effect of Soil Springs for One Story Building

For the following analyses, the model has been modified, as described in Section 5.2, such that SSI could be used. The structure has been modeled with FB elements, stirrups with a spacing of 150mm and the base case ground acceleration in the following analyses. As shown in Figure 7.11, the excitation in y-direction does not affect the displacement and forces obtained in the structure significantly. Due to this, the 2D-model in Figure 7.8 is used in the current and the following section of this thesis.

As a base case, an analysis where the model is fixed has been done first. This base case will be used for comparison to the results from the analyses with soil springs applied. To see how the different parameters influences the results, the parameters have been changed one at a time. For the link elements that have been used in the following analyses, a stiffness-proportional damping of 1% is used. The different analyses have been done for both a one- and two-story building, and are listed below:

- i.* Nonlinear horizontal springs and fixed rocking springs.
- ii.* Fixed horizontal springs and linear rocking springs.
- iii.* Fixed horizontal springs and linear rocking springs, with increased acceleration.
- iv.* Fixed horizontal springs and linear rocking springs, for a smaller foundation.
- v.* Linear horizontal springs and linear rocking springs, for a smaller foundation.

***i.* Nonlinear Horizontal Springs**

While the rocking springs are still assumed to be fixed, a nonlinear model is given for the horizontal springs. By doing this, the effect of soil-structure interaction due to horizontal flexibility will be shown. The Ramberg–Osgood model is used for the horizontal springs, and the foundation is modeled to be $1.5\text{m} \times 1.5\text{m}$, hence, the properties given in Table 5.2 are used for the Ramberg–Osgood model.

From Figure 8.9 it is seen that the displacement is reduced at some points by use of horizontal soil springs, but also increased at some places. Figure 8.10 and 8.11 shows the base shear and moment at the base of the left column of the frame in Figure 7.8 when the structure is fixed, and when it is modeled with soil springs. From these graphs, it is observed that the maximum force and moment are slightly reduced. This may also be seen in Figure 8.12 and 8.13 where the hysteretic curves for the structure are shown. The figures shows that the maximum displacement and rotation are reduced by implementing soil springs.

The maximum moment for the fixed structure is measured to be 96.9kNm , and it is reduced to 96.1kNm by applying non-linear horizontal soil springs. This means that horizontal flexibility in this case reduces the maximum moment by 0.8%.

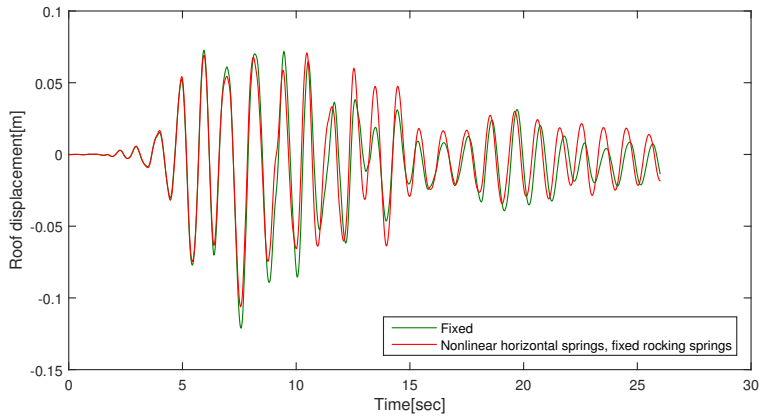


Figure 8.9: Displacements for structure with nonlinear horizontal springs applied.

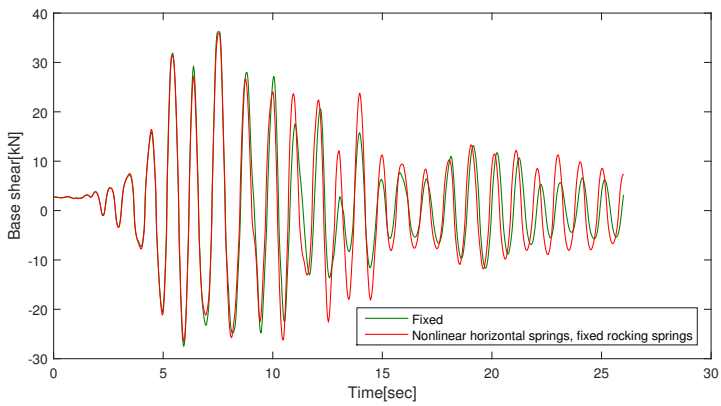


Figure 8.10: Shear force at base of column with nonlinear horizontal springs applied.

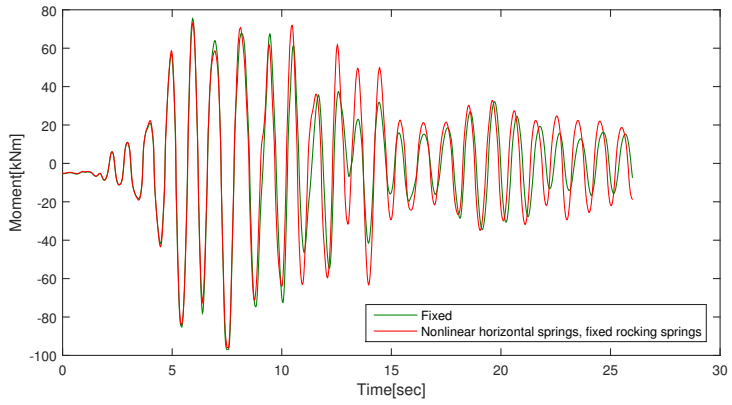


Figure 8.11: Moment at base of column with nonlinear horizontal springs applied.

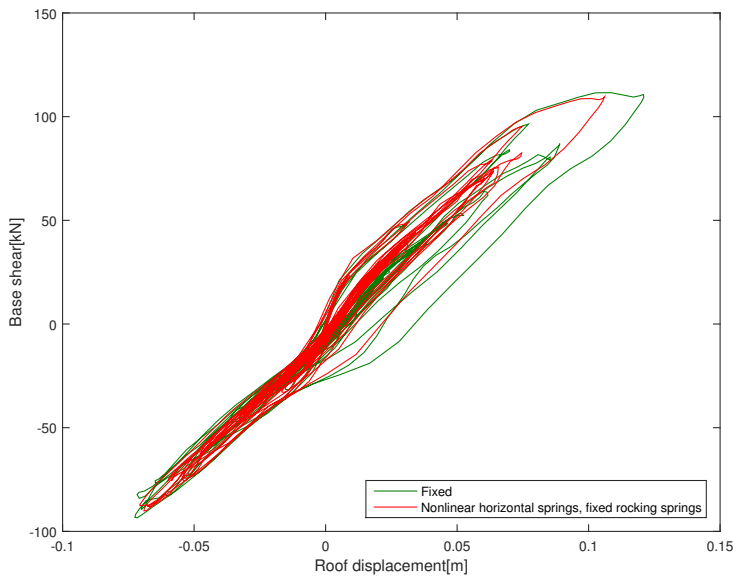


Figure 8.12: Force-displacement response for structure with nonlinear horizontal springs applied.

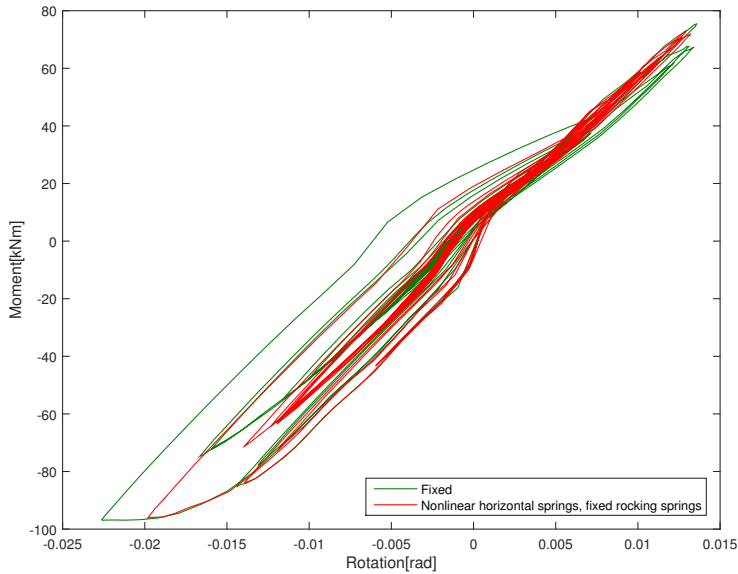


Figure 8.13: Moment-rotation response at base of column with nonlinear horizontal springs applied.

In Figure 8.14, the hysteretic curve for the horizontal link element in x-direction is plotted. It is clearly seen that the shape of the curve is the Ramberg-Osgood model, and this means that the link element works as expected. The base shear in the hysteretic curve in Figure 8.14 varies from -22 kN to 26 kN , while the base shear in Figure 8.10 varies from -26 kN to 36 kN . This can be explained by that for a base element that is connected to a support, the shear forces at the base element and the corresponding support might differ under large displacements. This is due to the fact that the local axis system for the base elements is heavily rotated, while the supports are defined in the global reference system (SeismoSoft (2014a)).

From the same figure, it can also be seen that yield is reached for the link element, which should reduce the shear force. This is because when the link element yields, less acceleration is transferred to the base node of the columns, hence reduced base shear. An analysis that will not be shown here, has been done to see if this happens for an even higher acceleration. The results showed that the base shear was clearly reduced by using a higher acceleration, and the hysteretic curve showed that higher deformations were reached during yielding, i.e. a higher possibility for fracture in the structure.

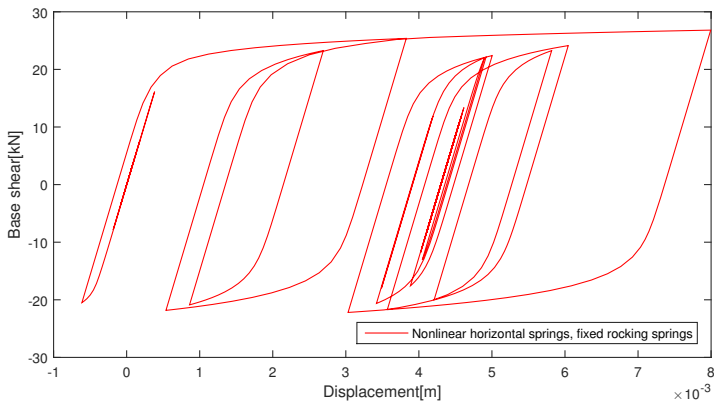


Figure 8.14: Force-displacement response for nonlinear horizontal spring.

ii. Linear Rocking Springs

To see the effect of soil-structure interaction because of rocking flexibility, the horizontal springs have been modeled to have a high stiffness, i.e. assumed to be fixed. The rocking springs have been modeled to be linear, with the stiffness found earlier, $K_{\theta} = 27294 kNm$. The output from the analysis is given in Figure 8.15 to 8.20. Figure 8.15 shows that the roof displacement, as for the previous analysis, increases at some points and decreases at others. Force-displacement response for the whole structure is depicted in Figure 8.18, and the moment-rotation response at the base of the western column is seen in Figure 8.19. By introducing linear rocking soil springs, the maximum moment is reduced to $96.2 kN$, which means a reduction of 0.7%.

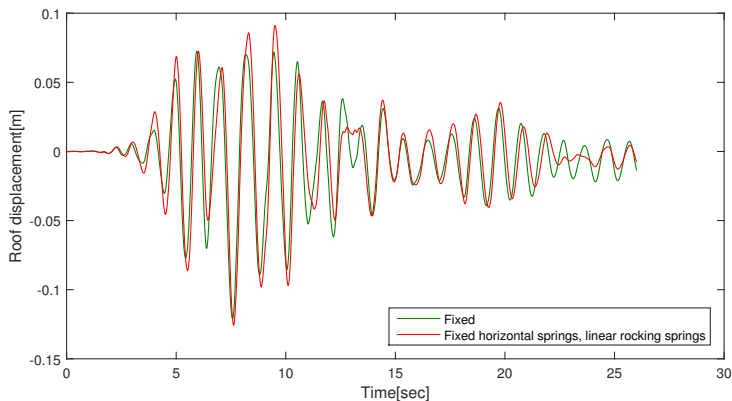


Figure 8.15: Displacements for structure with linear rocking springs applied.

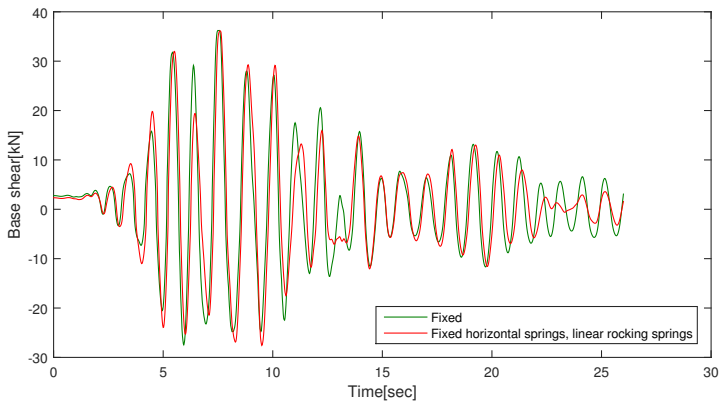


Figure 8.16: Shear force at base of column with linear rocking springs applied.

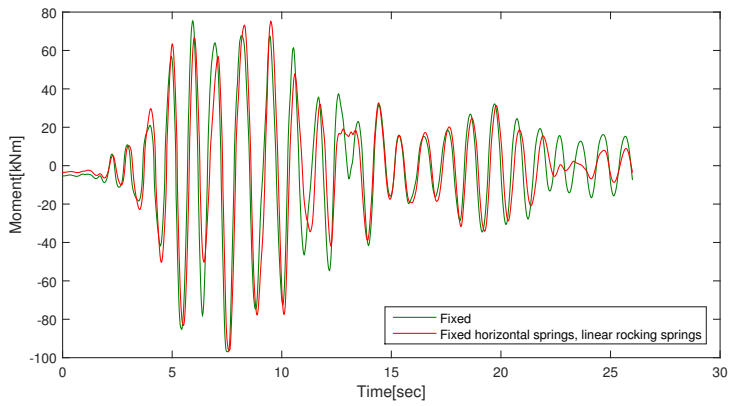


Figure 8.17: Moment at base of column with linear rocking springs applied.

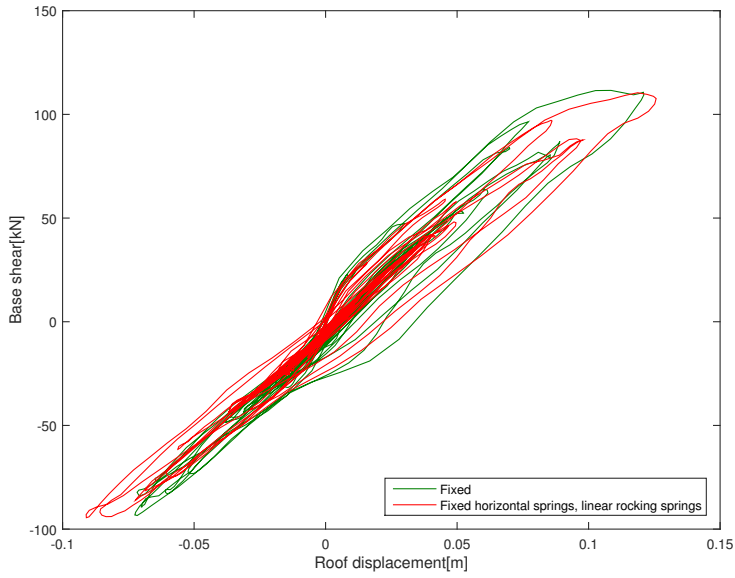


Figure 8.18: Force-displacement response for structure with linear rocking springs applied.

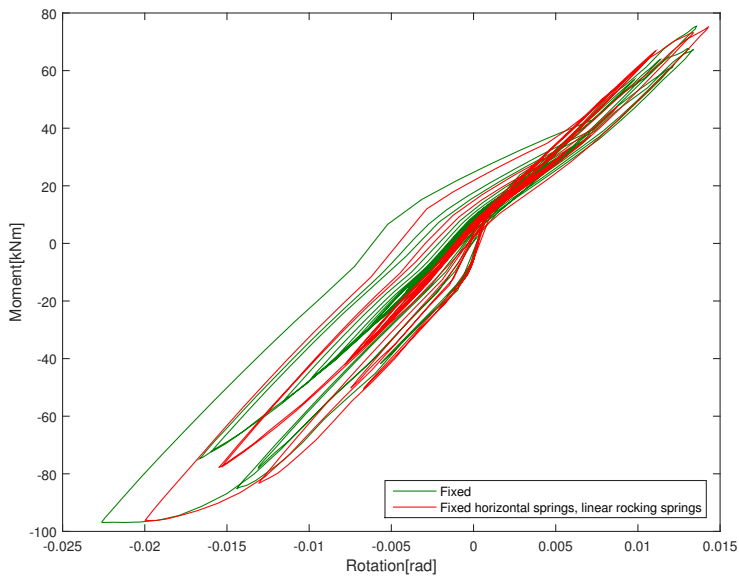


Figure 8.19: Moment-rotation response at base of column with linear rocking springs applied.

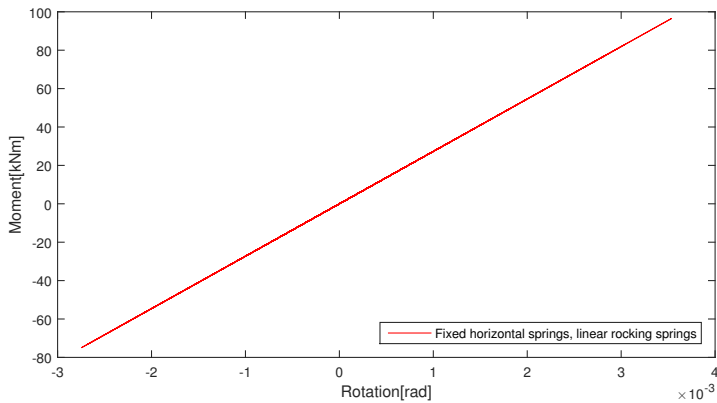


Figure 8.20: Moment-rotation response in rocking spring.

To check if the response in the rocking springs is linear, the moment-rotation hysteretic curve for the rocking spring is depicted in Figure 8.20. The response is obviously linear, and the link element behaves as expected.

iii. Increased Acceleration

To see the effect of soil-structure interaction under higher accelerations, the acceleration has been changed from the base case acceleration of $0.32g$ to $0.5g$. An analysis for the fixed building was first done, such that the results that are compared, are both results from analyses with an excitation of $0.5g$. The increased acceleration was applied to the model where the horizontal springs are assumed fixed and rocking springs are modeled to be linear, as in analysis *ii*. Results from the analysis with a higher excitation are depicted in Figure 8.21 to 8.25

Maximum moment that occurs when the structure is fixed and exposed to an excitation of $0.5g$ is $97.5kNm$. This is reduced to $97.4kNm$ by the use of rocking soil springs, which equals a reduction of 0.1% . For comparison, the reduction of maximum moment for analysis *ii* was 0.7% .

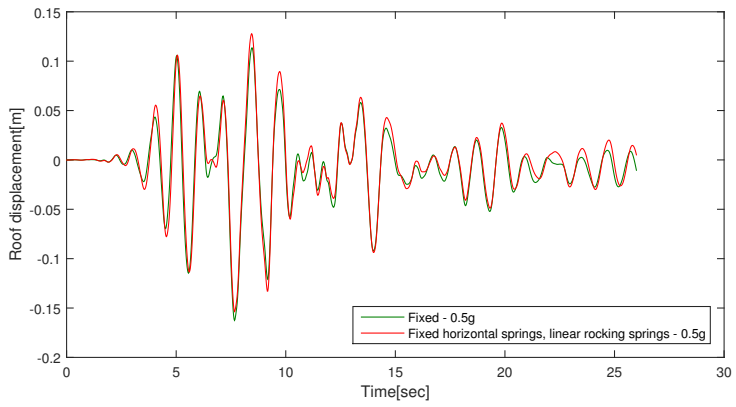


Figure 8.21: Displacements for structure with linear rocking springs applied.

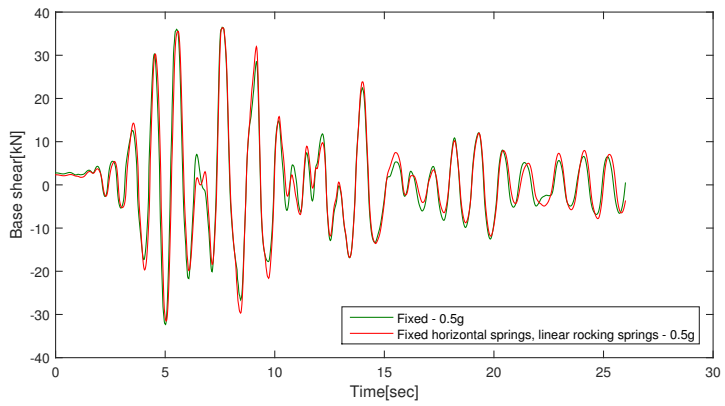


Figure 8.22: Shear force at base of column with linear rocking springs applied.

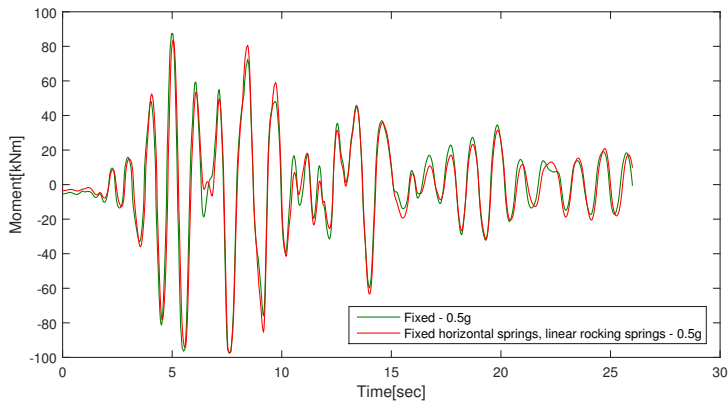


Figure 8.23: Moment at base of column with linear rocking springs applied.

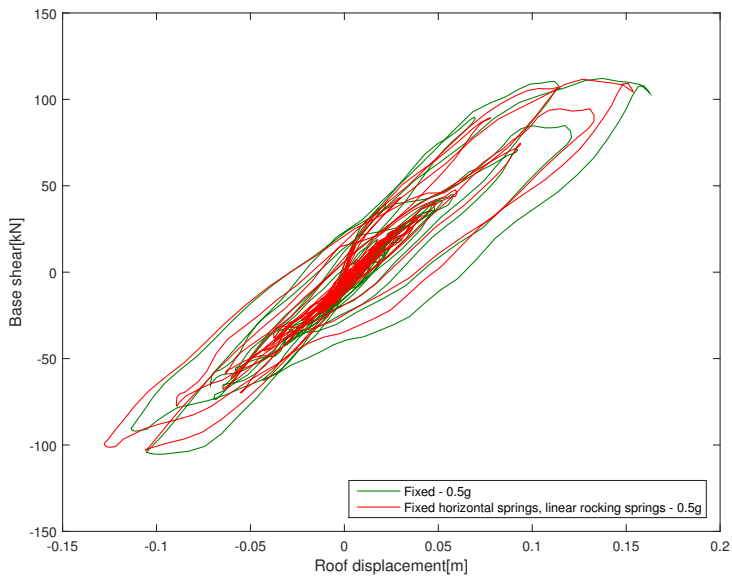


Figure 8.24: Force-displacement response for structure with linear rocking springs applied.

From Figure 8.24 it is seen that the hysteretic curve have gotten a more symmetric shape than in Figure 8.18. This is because higher displacements are reached for this analysis. The area under the load-deformation curve for one complete load cycle tells how much energy the structure is capable to dissipate (Shing (2014)), which means that the structure absorbs a higher amount of energy in this analysis than in analysis *ii*.

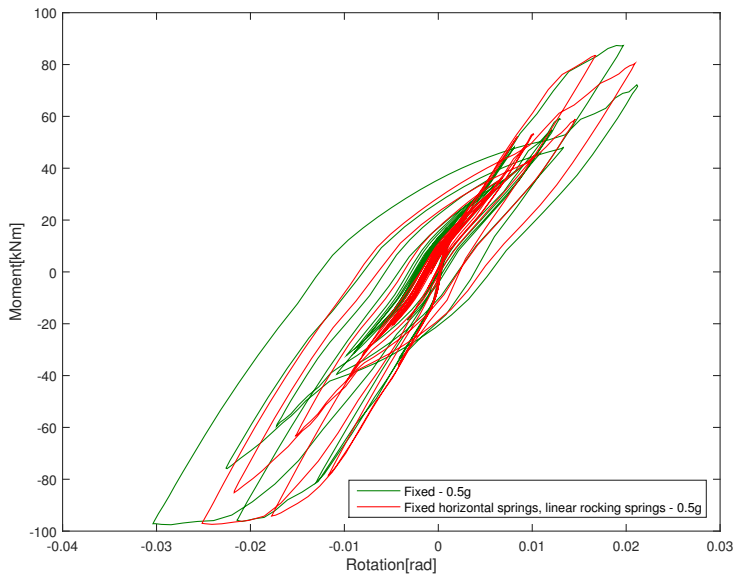


Figure 8.25: Moment-rotation response at base of column with linear rocking springs applied.

iv. Smaller Size of Foundation

The size of the foundation influences the response in the structure, as the stiffness is reduced. To see how this affects the results, the foundation size has been set to $1\text{ m} \times 1\text{ m}$. For a foundation with an area of 1 m^2 the yield force and displacement, horizontal and rocking stiffness are given in Table 8.1.

Table 8.1: Parameters for a foundation of $1\text{ m} \times 1\text{ m}$.

Parameters	Value
a	1m
F_y	10kN
$D_{y,h}$	0.0003571m
K_h	28000kN/m
K_θ	7805kNm/rad

The structure is modeled fixed in the horizontal directions and with linear rocking stiffness. The results from the analysis is compared to the results from analysis *ii*, such that the difference in the response is only due to change in size of foundation.

In Figure 8.26 to 8.30 the results are plotted. For the smaller size of foundation, the maximum moment is observed to be 75.1 kNm . This corresponds to a reduction of 22.5% compared to the maximum moment for the fixed structure. For the $1.5\text{ m} \times 1.5\text{ m}$ foun-

ation in analysis *ii*, the maximum moment for the fixed structure was only reduced by 0.7%.

Figure 8.29 shows the force-displacement response for the whole structure, and from the figure it is clear that the maximum displacement of the roof is less for the smaller foundation. It is also seen in Figure 8.30 that the maximum rotation at the base of the left column is much smaller for the $1\text{ m} \times 1\text{ m}$ foundation. By introducing a flexible foundation, through the use of a soil spring that is very flexible, the natural frequency of the structure is decreased, which leads to an increased period. A higher period results in lower forces, because earthquake is a high frequency response. From Figure 7.6 it is seen that if the period increases, the corresponding acceleration will decrease. This explains why the hysteretic curve in Figure 8.30 shows a smaller moment-rotation response for the $1\text{ m} \times 1\text{ m}$ foundation, than for the foundation of $1.5\text{ m} \times 1.5\text{ m}$.

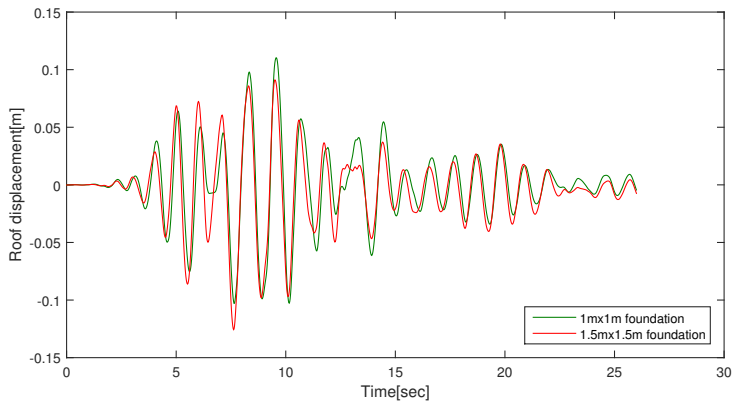


Figure 8.26: Displacements for structure with $1\text{ m} \times 1\text{ m}$ and $1.5\text{ m} \times 1.5\text{ m}$ foundation.

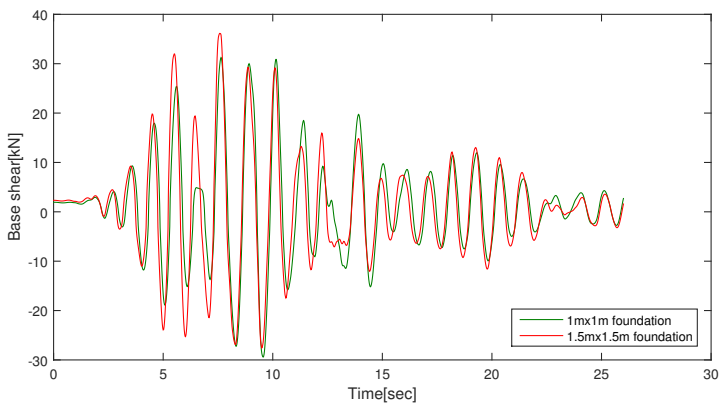


Figure 8.27: Shear force at base of column for structure with $1\text{ m} \times 1\text{ m}$ and $1.5\text{ m} \times 1.5\text{ m}$ foundation.

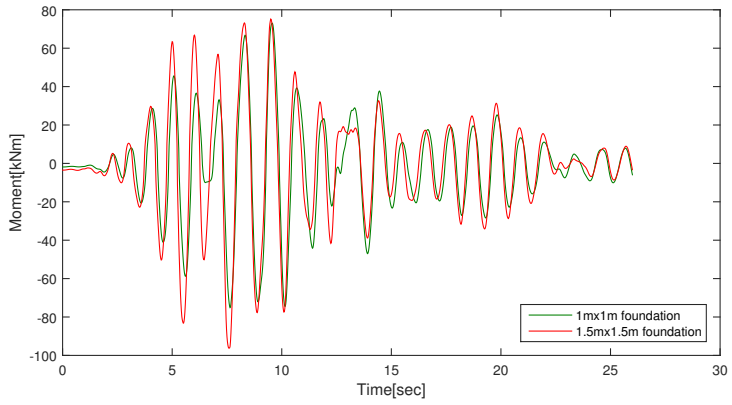


Figure 8.28: Moment at base of column for structure with $1\text{ m} \times 1\text{ m}$ and $1.5\text{ m} \times 1.5\text{ m}$ foundation.

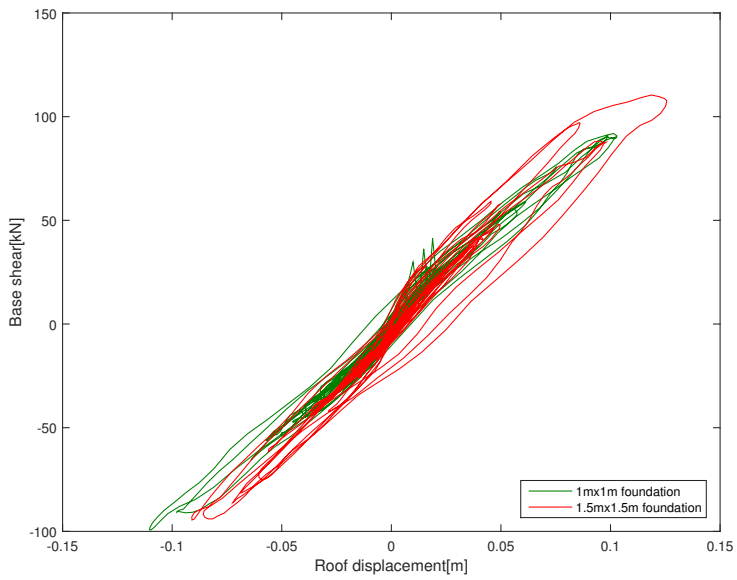


Figure 8.29: Force-displacement response for structure with $1\text{ m} \times 1\text{ m}$ and $1.5\text{ m} \times 1.5\text{ m}$ foundation.

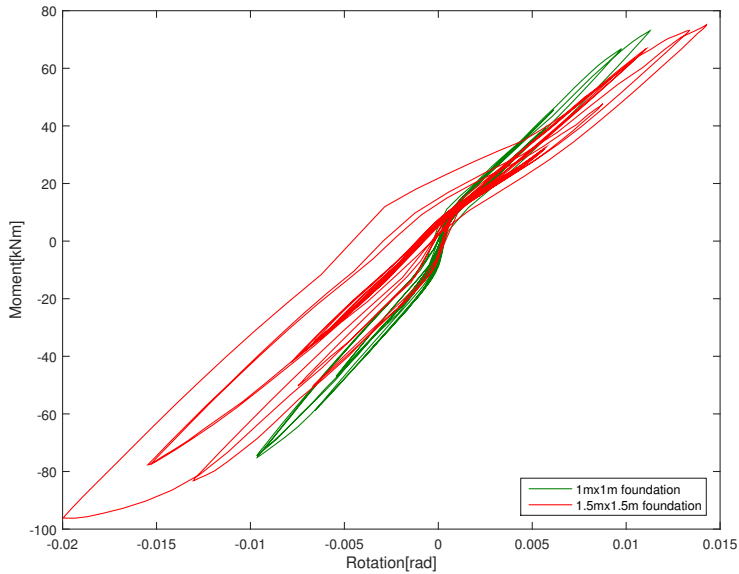


Figure 8.30: Moment-rotation response at base of column for structure with $1\text{ m} \times 1\text{ m}$ and $1.5\text{ m} \times 1.5\text{ m}$ foundation.

v. Linear Horizontal and Rocking Springs

From the previous analyses that have been done, it is seen that the effect of SSI is best shown in analysis *iv*. The foundation of $1\text{ m} \times 1\text{ m}$ is therefore used in an additional analysis. In this analysis, both the horizontal and rocking springs have been modeled to be linear. The results are shown in Figure 8.31 to 8.35, where they are compared to the results from the structure when it is fixed.

From analysis *iv* it was found that the reduction of maximum moment was 22.5%. By modeling the horizontal springs to be linear instead of fixed, the maximum moment is reduced even more. The maximum value of the moment is now found to be 74.0 kNm , which is a reduction of 23.6%.

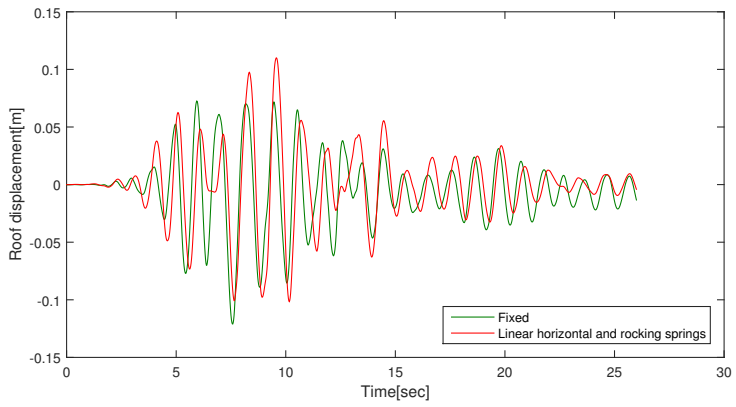


Figure 8.31: Displacement of roof for structure with linear soil springs, and foundation of $1m \times 1m$.

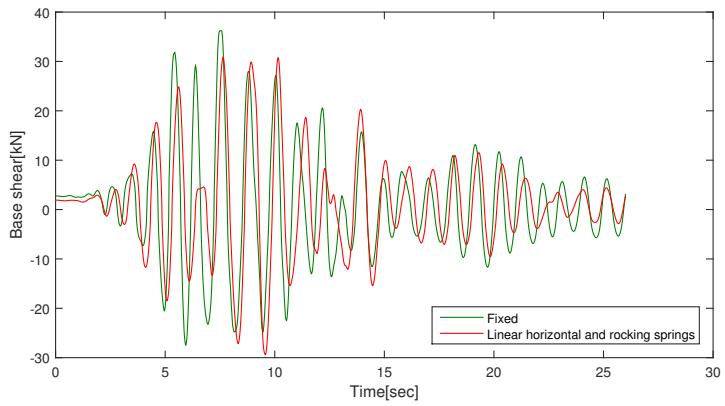


Figure 8.32: Base shear at base of column with linear soil springs, and foundation of $1m \times 1m$.

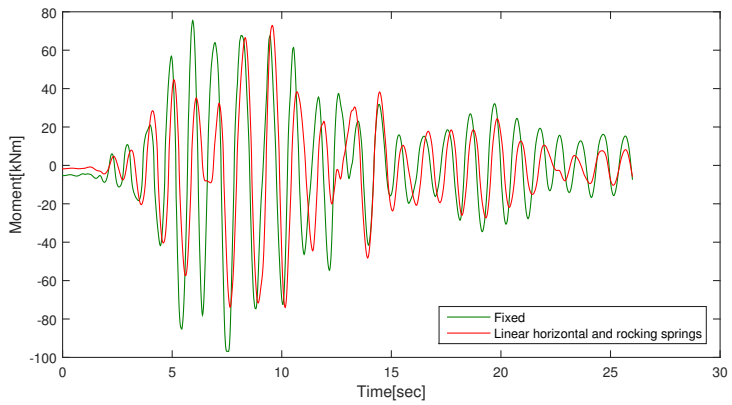


Figure 8.33: Moment at base of column with linear soil springs, and foundation of 1m×1m.

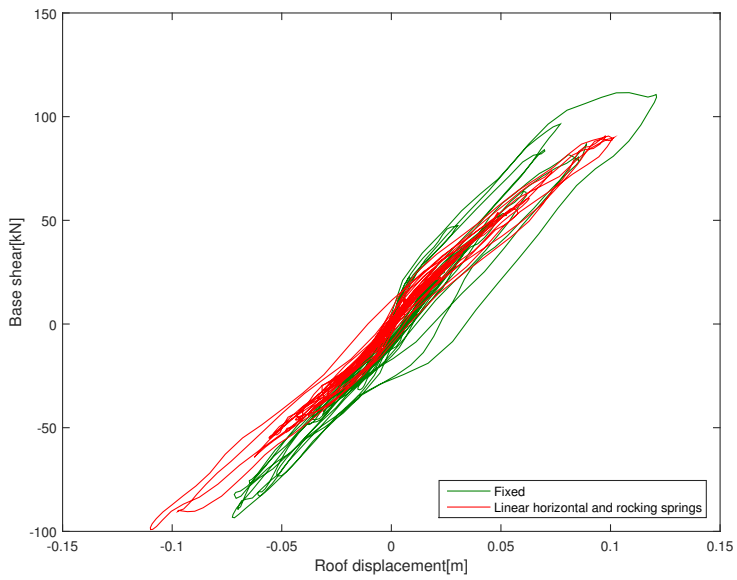


Figure 8.34: Force-displacement response for structure with linear soil springs, and foundation of 1m×1m.

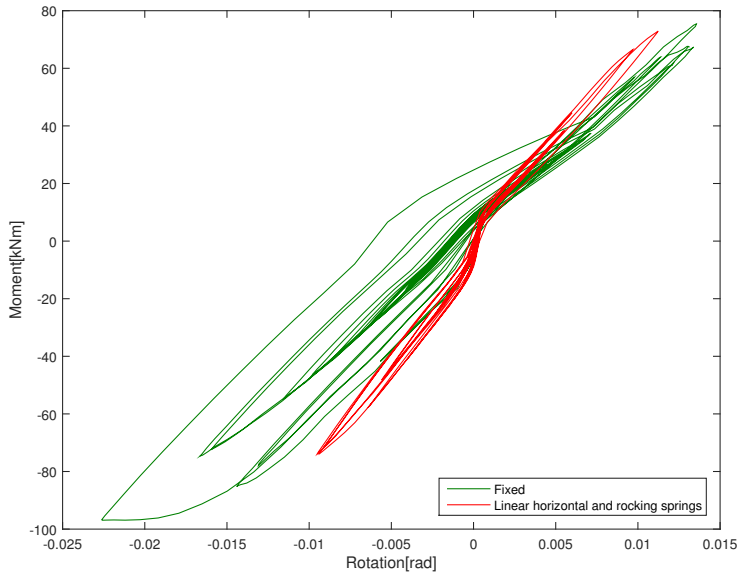


Figure 8.35: Moment-rotation response at base of column with linear soil springs, and foundation of $1m \times 1m$.

A summary of the results found from the different analyses for the one story building are given in Table 8.2. It is obvious that analysis *v* gives the largest reduction of the moment. The effect of SSI for analysis *i-iii* is close to none, and it may seem like the stiffness for the foundation of $1.5m \times 1.5m$ is so high that the introduction of springs does not give any particular change in results.

As the stiffness is reduced, by using a smaller foundation, the effect of SSI is a lot bigger. Compared to the moment for the fixed structure, the maximum moment is reduced 22.5% for analysis *iv*, and 23.6% for analysis *v*.

An important observation from all of the moment-rotation response curves, is that the fixed structure seems to have rotated. This is shown in Figure 8.13, 8.19, 8.25, 8.30 and 8.35. This must mean that plasticity occurs in the concrete, and that a rotation takes place. Since SeismoStruct does not completely restrain the columns from rotating, it may lead to that the effect of SSI will not be as clear as expected. For a fixed structure with no rotation at the base, the moment would probably be more affected by introduction of soil springs, than when a small rotation is already existing for the fixed structure.

Table 8.2: Maximum moment for the different analyses for the one story building, and reduction of maximum moment for the fixed structure in percent.

One story building		
Boundary conditions	Maximum moment	Reduction
i. Fixed horizontal springs, linear rocking springs	96.2kNm	0.8%
ii. Fixed rocking springs, Nonlinear horizontal springs	96.1kNm	0.7%
iii. Fixed horizontal springs, linear rocking springs - 0.5g	97.4kNm	0.1%
iv. Fixed horizontal springs, linear rocking springs - 1m×1m foundation	75.1kNm	22.5%
v. Linear horizontal springs, linear rocking springs - 1m×1m foundation	74.0kNm	23.6%

8.3 Effect of Soil Springs for Two Story Building

To get a better understanding on how SSI affects the forces and displacements for a structure, it is interesting to take a look at a multistory building. For simplicity the multistory building was also made in 2D with a unidirectional excitation, as seen in Figure 8.36.

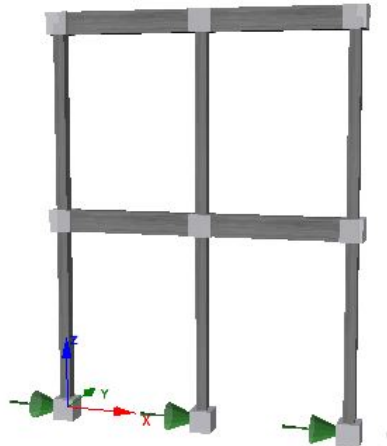


Figure 8.36: 2D model with two stories.

By expanding the model by one floor, it is possible to see the effect of SSI in several junctions. As for the previous analyses, the structure is still modeled with FB elements,

and the spacing in stirrups is set to 150mm.

As the vertical load increases with an additional story, due to increased self-weight, the foundations are set to be $2m \times 2m$, which will be the base case for the two story building. This leads to some changes in the parameters used for the hysteresis curves for the link elements. The new parameters are given in Table 8.3.

Table 8.3: Parameters for a foundation of $2m \times 2m$.

Parameters	Value
a	1.13m
F_y	40kN
$D_{y,h}$	0.0007080m
K_h	56500kN/m
K_θ	64129kNm/rad

Analyses $i - v$ from Section 8.2 have been done for the two story building, with the same parameter studies as for the one story building. An analysis where the structure is fixed has been done first, and will be the basis for comparison of results.

***i.* Nonlinear Horizontal Springs**

For the first parameter change, the results are given in Figure 8.37 to 8.43, and it is seen that they do not differ particularly from the fixed structure's results. However, the maximum moment observed is slightly reduced. The maximum moment for the fixed structure is $107.2kNm$, while it for this case is found to be $106.3kNm$. In percent, this is a reduction of 0.8%, which is the same reduction as for the one story building. Because an extra floor is added to the structure, an additional hysteresis curve is presented. The hysteresis curve in Figure 8.42 shows the moment-rotation response in the left column at the base of the first floor. From the hysteretic curves it is seen that more energy is absorbed at the base of the column at the ground floor than at the first floor. This is an observation that is as expected, as the moment will be higher at the ground floor than at the first floor.

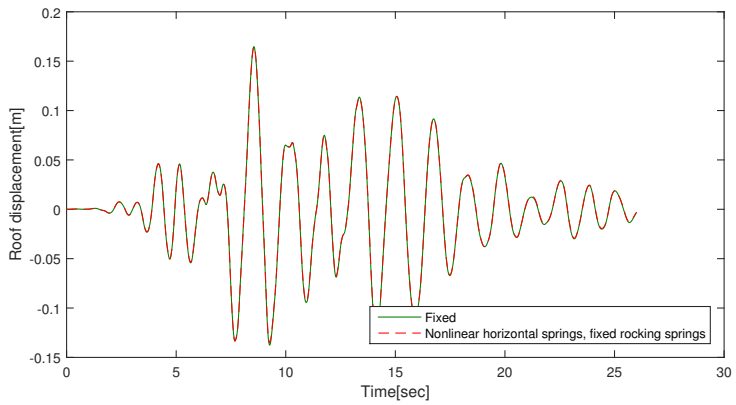


Figure 8.37: Displacements for structure with nonlinear horizontal springs applied.

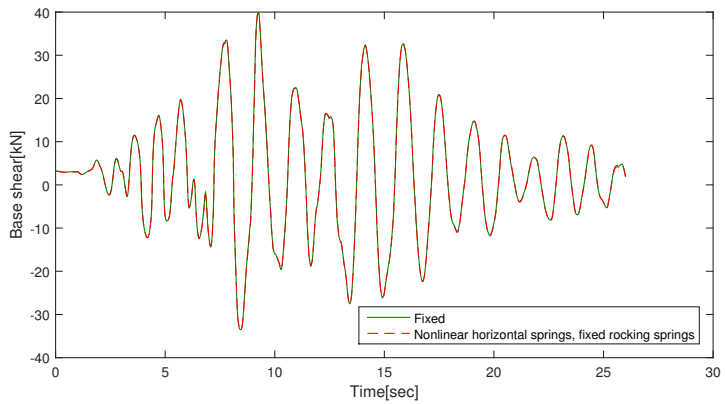


Figure 8.38: Shear force at base of column with nonlinear horizontal springs applied

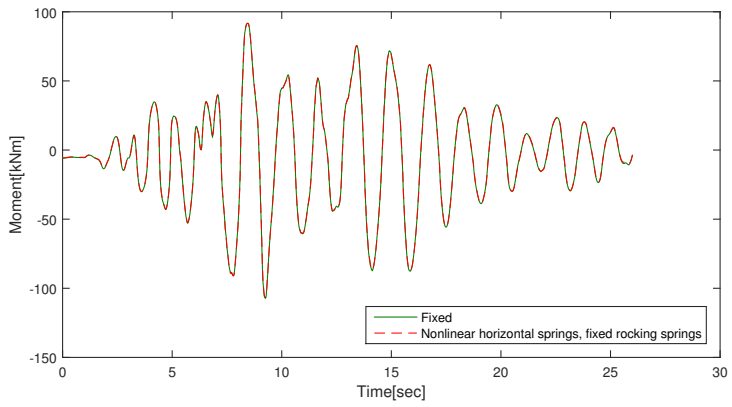


Figure 8.39: Moment at base of column with nonlinear horizontal springs applied.

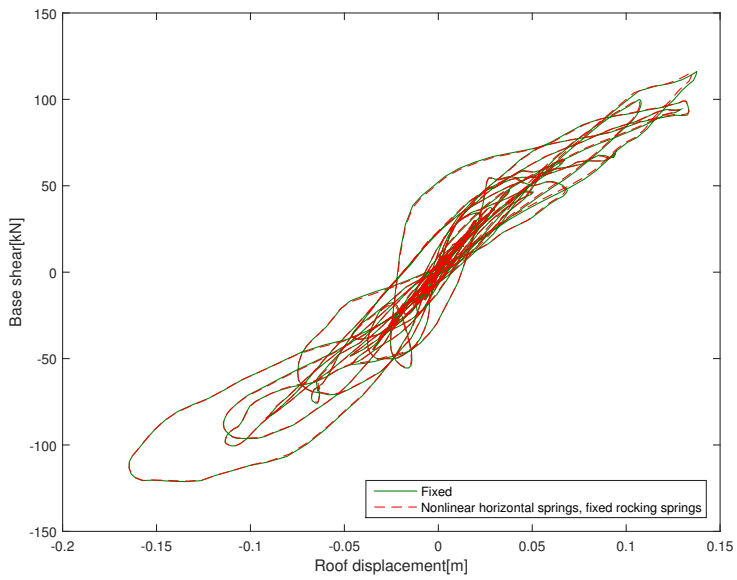


Figure 8.40: Force-displacement response for structure with nonlinear horizontal springs applied.

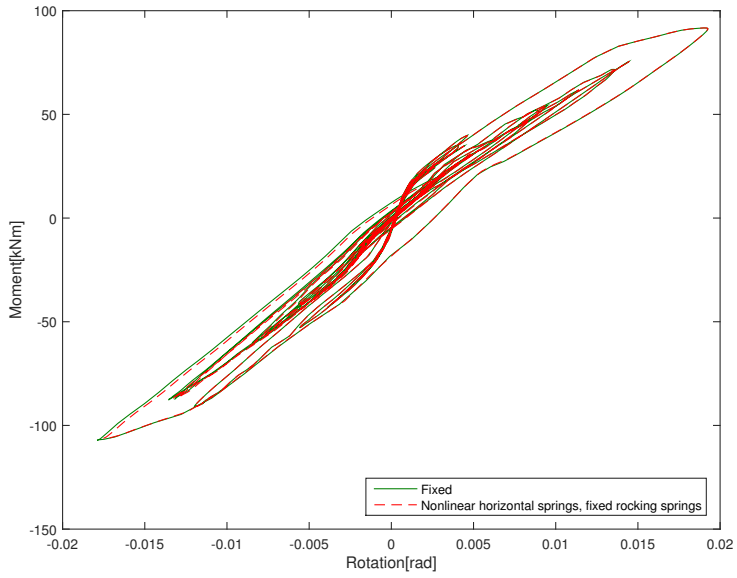


Figure 8.41: Moment-rotation response at base of column at ground floor. Nonlinear horizontal springs applied at the base of the structure.

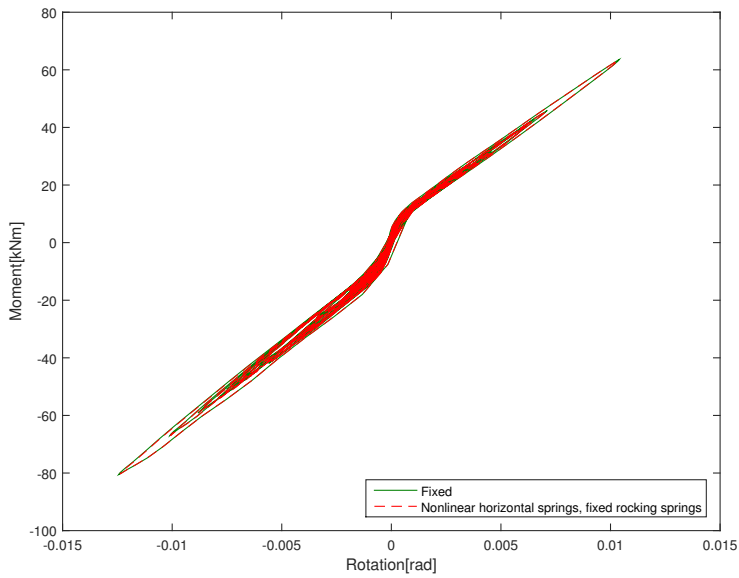


Figure 8.42: Moment-rotation response at base of column in first floor. Nonlinear horizontal springs applied at the base of the structure.

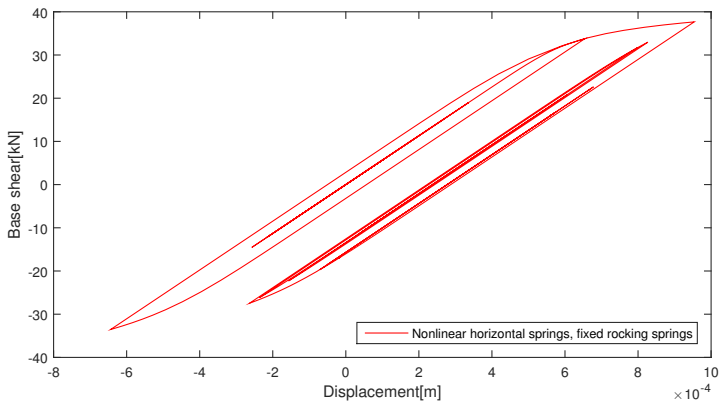


Figure 8.43: Force-displacement response for nonlinear horizontal spring.

The hysteretic curve for the horizontal link element takes the shape of the Ramberg-Osgood curve for the two story building as well. This is depicted in Figure 8.43.

ii. Linear Rocking Springs

To see the effect of rocking flexibility, the horizontal springs were again set to be fixed, and the rocking stiffness defined linear. The rocking stiffness from Table 8.3 was used, and the results are shown in Figure 8.44 to 8.49

For linear rocking springs applied to the two story structure, the results shows a small difference from the results for the fixed building. A maximum moment of $104.1 kNm$ is measured, i.e. a reduction of 2.9% compared to the maximum moment for the fixed structure. The results for the two story structure are also more similar to the response for the fixed structure, than for the one story structure.

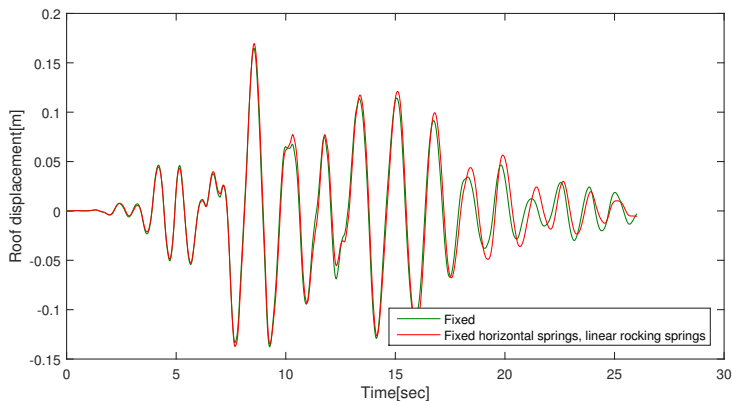


Figure 8.44: Displacements for structure with linear rocking springs applied.

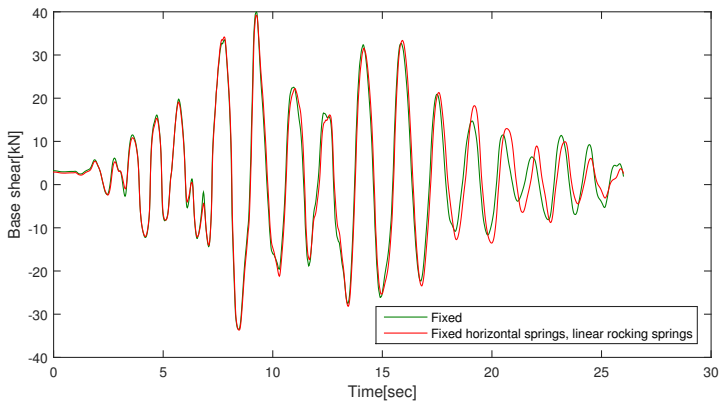


Figure 8.45: Shear force at base of column with linear rocking springs applied.

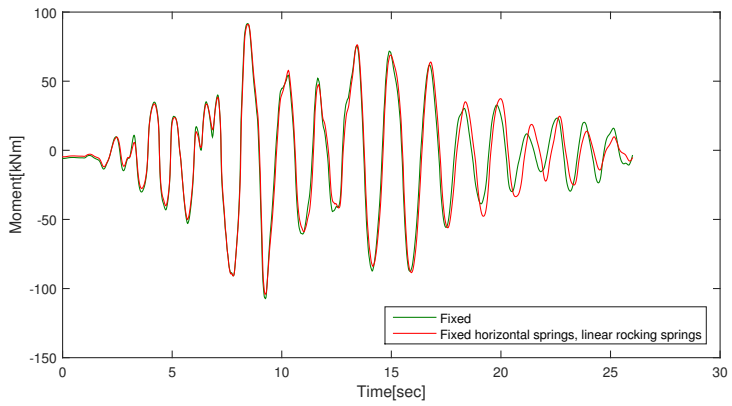


Figure 8.46: Moment at base of column with linear rocking springs applied.

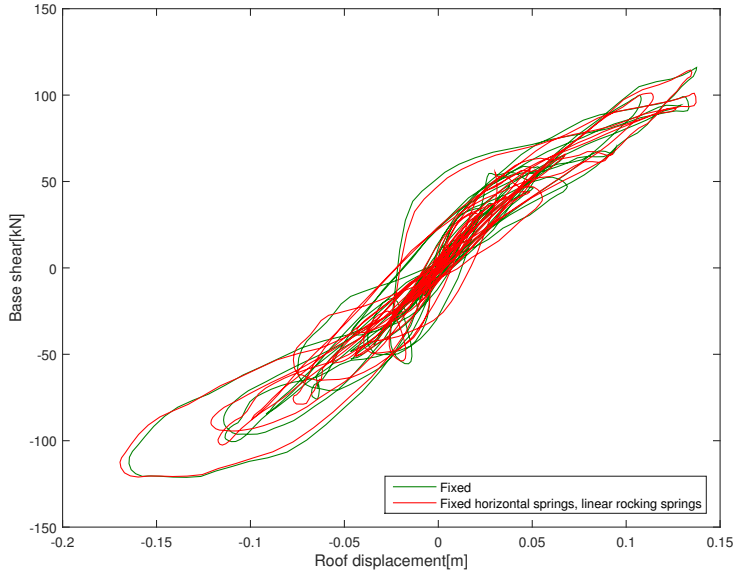


Figure 8.47: Force-displacement response for structure with linear rocking springs applied.

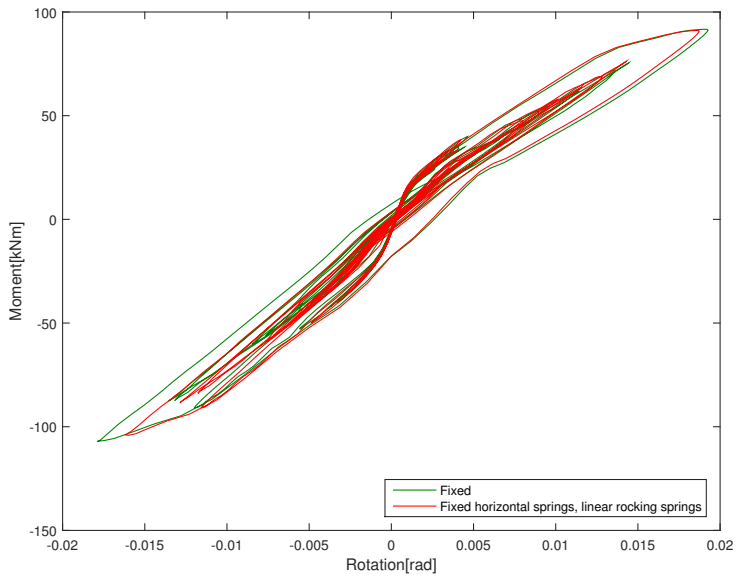


Figure 8.48: Moment-rotation response at base of column at ground floor. Linear rocking springs applied at the base of the structure.

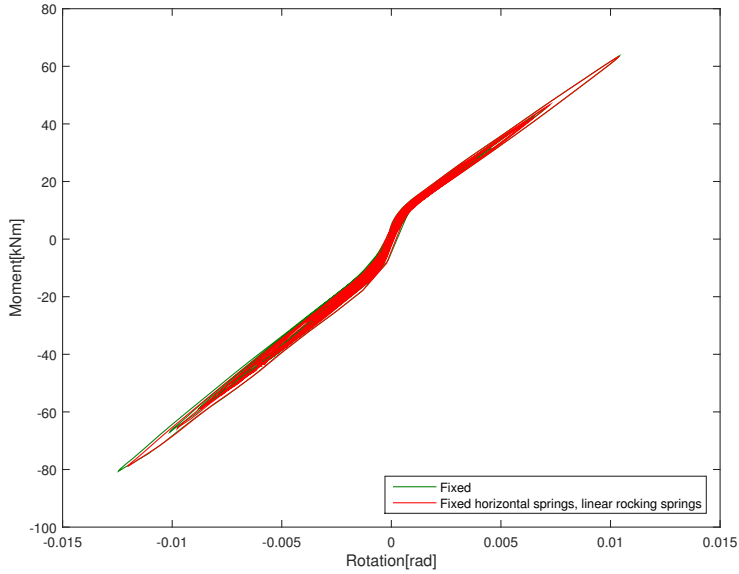


Figure 8.49: Moment-rotation response at base of column in first floor. Linear rocking springs applied at the base of the structure.

iii. Increased Acceleration

For the next analysis, the excitation has been set to $0.5g$ and the structure is modeled as in analysis *ii*. From the results in Figure 8.50 to 8.55 it is seen that the variation between the fixed structure and the structure with linear rocking springs is small. The maximum measured moment is equal for the analyses in this case.

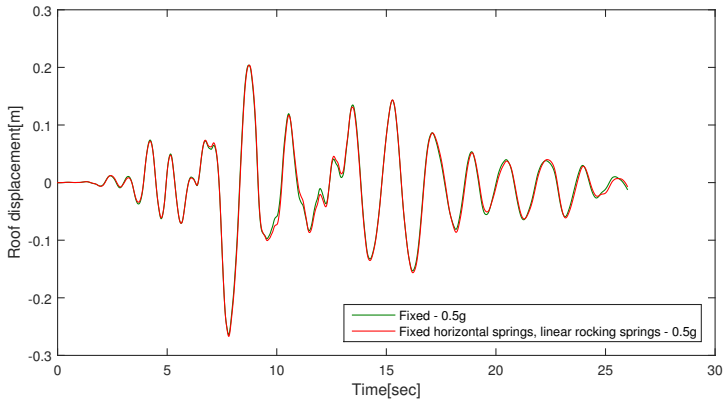


Figure 8.50: Displacements for structure with linear rocking springs applied, and increased acceleration.

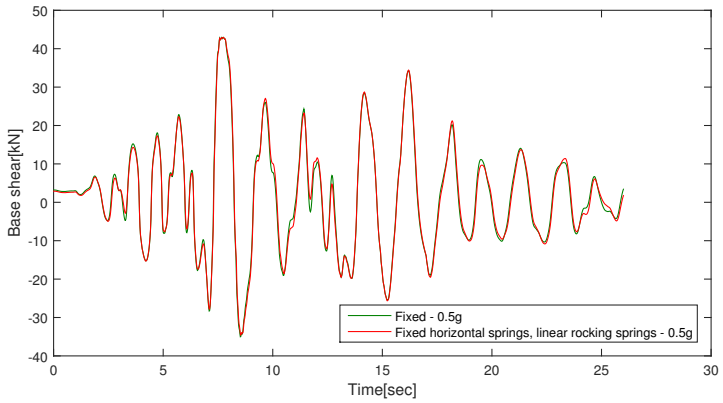


Figure 8.51: Shear force at base of column with linear rocking springs applied, and increased acceleration.

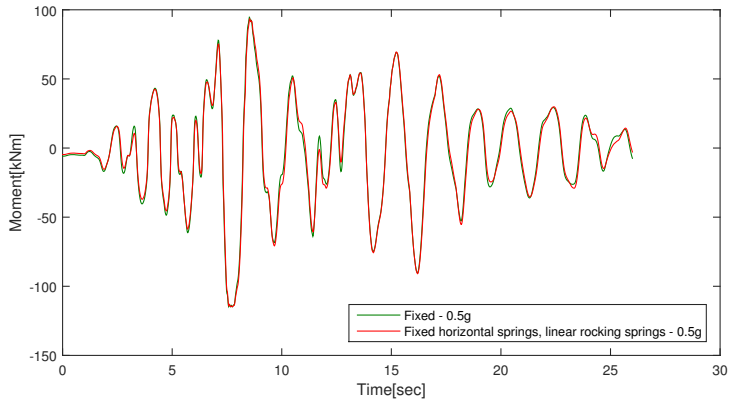


Figure 8.52: Moment at base of column with linear rocking springs applied, and increased acceleration.

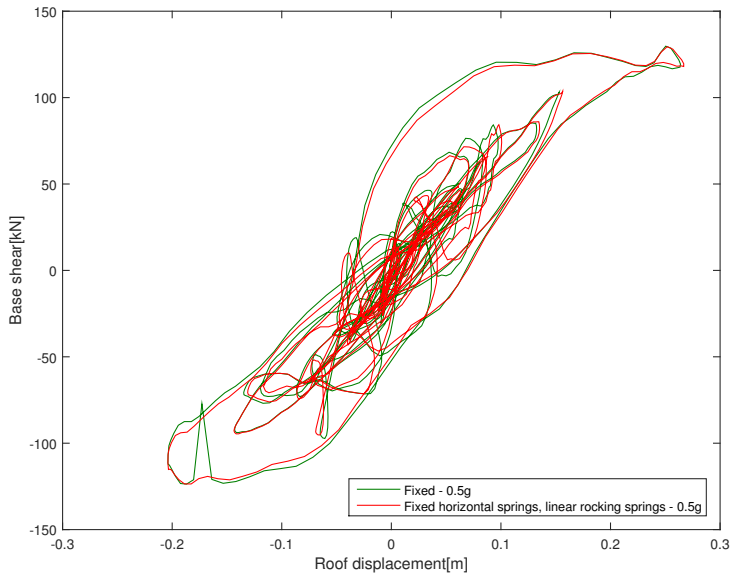


Figure 8.53: Force-displacement response for structure with linear rocking springs applied, and increased acceleration.

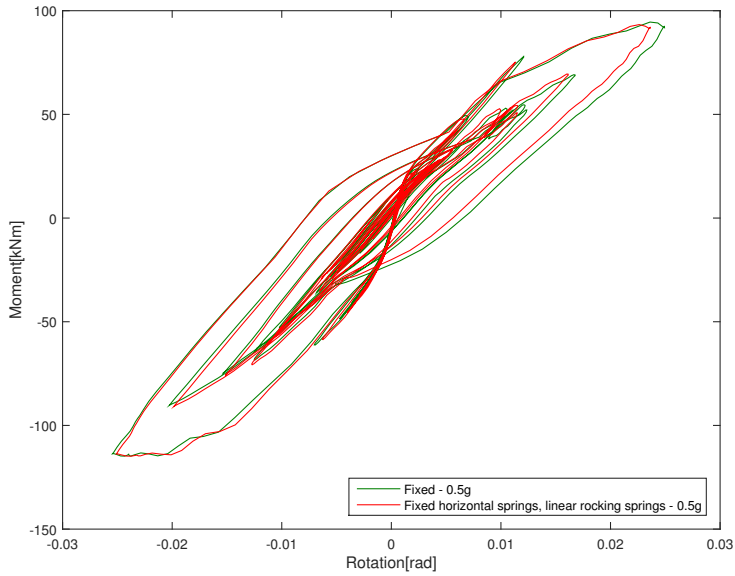


Figure 8.54: Moment-rotation response at base of column at ground floor. Linear rocking springs applied at the base of the structure, and increased acceleration.

As for the one story structure, the hysteretic curve is changed when the acceleration is increased. The area under the curve in Figure 8.54 and 8.55 is larger than in Figure 8.48 and 8.49, hence, a higher hysteretic damping and more energy absorbed by the structure.

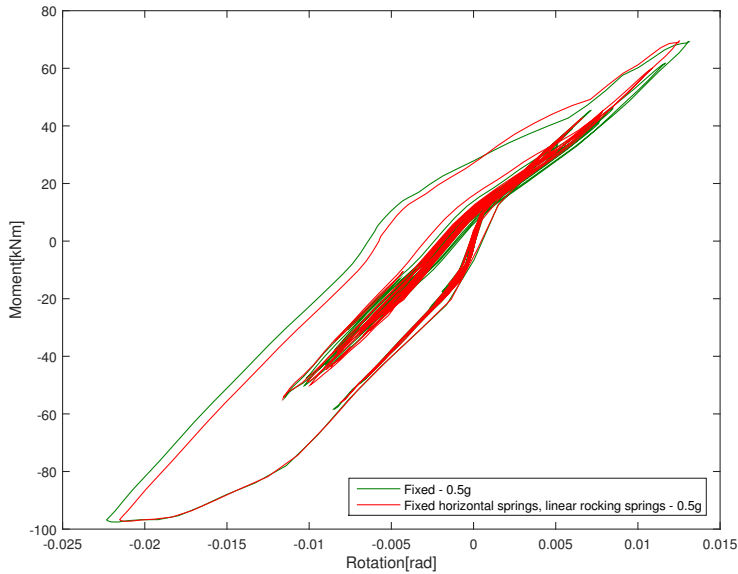


Figure 8.55: Moment-rotation response at base of column in first floor. Linear rocking springs applied at the base of the structure, and increased acceleration.

iv. Smaller Size of Foundation

To see how the response is influenced by defining a smaller foundation for the two story building, the foundation size has been set to $1.5m \times 1.5m$. The results from this analysis are compared to the results where the foundation was defined to be $2m \times 2m$. Soil springs in horizontal direction are still assumed to be fixed, and the rocking springs are modeled linear. For the foundation with a size of $1.5m \times 1.5m$, the properties in Table 5.2 are used. The results are shown in Figure 8.56 to 8.61.

From analysis *ii*, it was found that the moment was reduced 2.9% for the original foundation. By reducing the foundation size, the maximum moment is measured to be $99.5kNm$, which is a reduction of 7.2%.

It is worth mentioning that it seems like the stiffness of the springs are not modified as much in this analysis as it was in analysis *iv* for the one story building. Correspondingly for this case, it looks like the natural frequency of the structure is approximately the same regardless of the size of foundation.

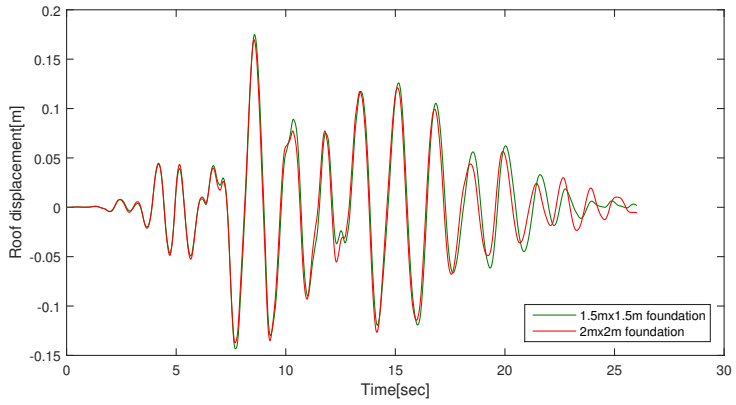


Figure 8.56: Displacements for structure with linear rocking springs applied, and foundation of $1.5m \times 1.5m$.

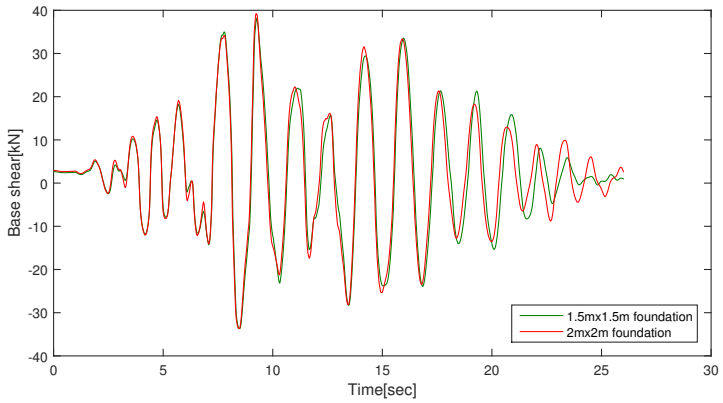


Figure 8.57: Shear force at base of column with linear rocking springs applied, and foundation of $1.5m \times 1.5m$.

8.3. EFFECT OF SOIL SPRINGS FOR TWO STORY BUILDING

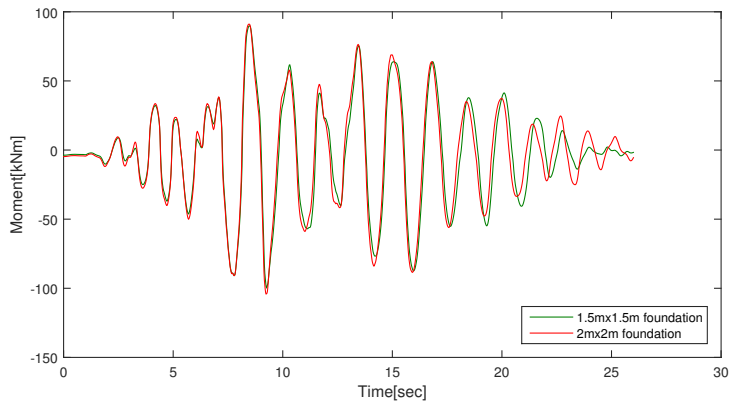


Figure 8.58: Moment at base of column with linear rocking springs applied, and foundation of $1.5\text{m} \times 1.5\text{m}$.

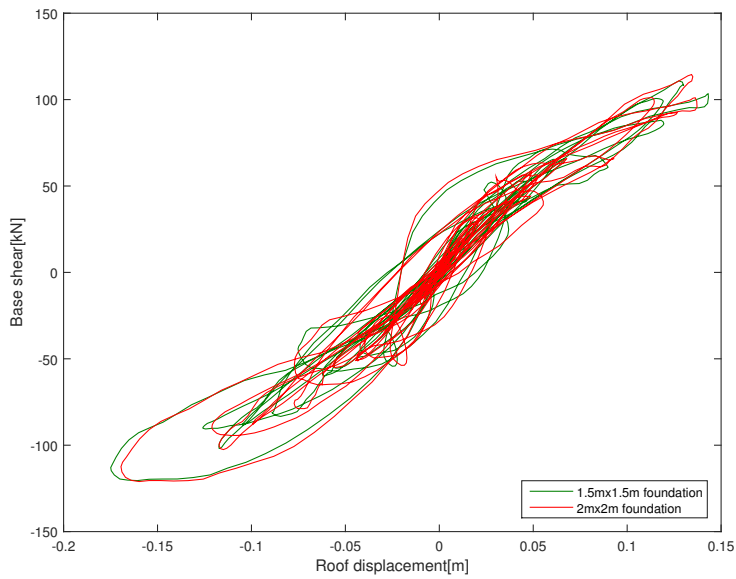


Figure 8.59: Force-displacement response for structure with linear rocking springs applied, and foundation of $1.5\text{m} \times 1.5\text{m}$.

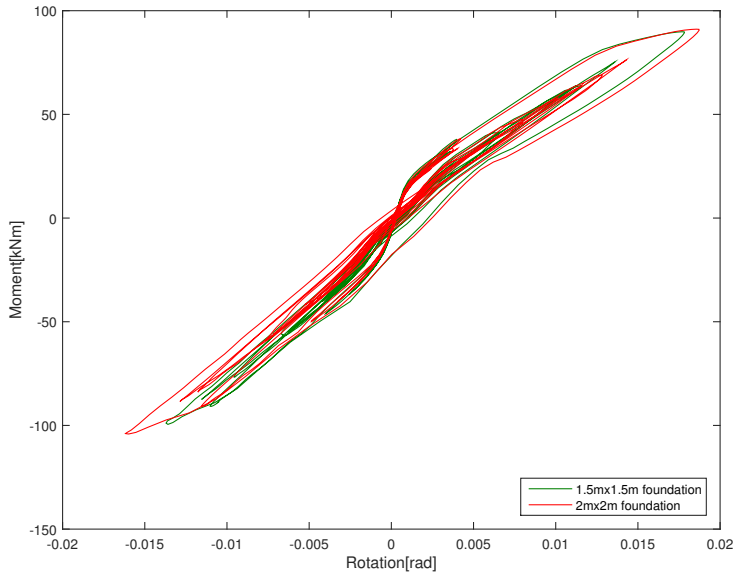


Figure 8.60: Moment-rotation response at base of column at ground floor. Linear rocking springs applied at the base of the structure, and foundation of $1.5\text{m} \times 1.5\text{m}$.

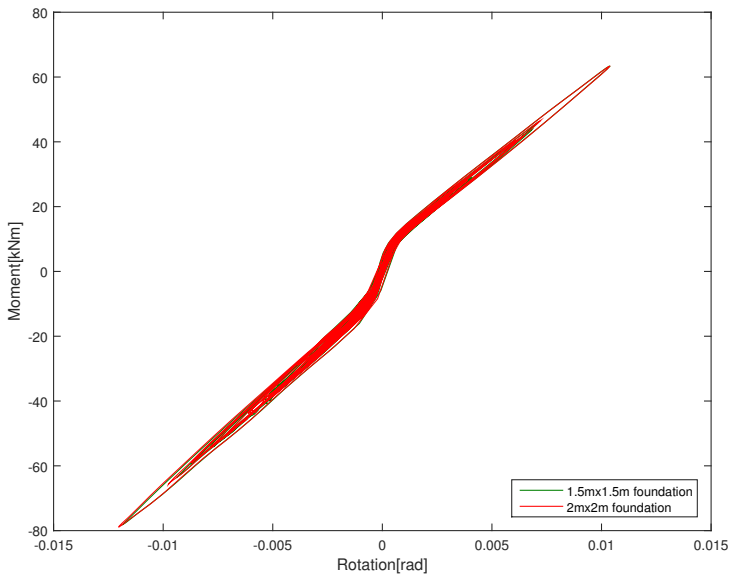


Figure 8.61: Moment-rotation response at base of column in first floor. Linear rocking springs applied at the base of the structure, and foundation of $1.5\text{m} \times 1.5\text{m}$.

***v.* Linear Horizontal and Rocking Springs**

For the last analysis, the foundation size of $1.5\text{m} \times 1.5\text{m}$ is kept, and all soil springs modeled to be linear. The results are shown in Figure 8.62 to 8.67.

From the analysis it was found that the maximum value of the moment is 98.9kNm . This is a reduction of 7.7% compared to the maximum moment of 107.2kNm for the fixed structure. The reduction for the maximum moment in analysis *iv* was 7.2%, which as earlier shows that the change from fixed to linear horizontal springs does reduce the moment more than in analysis *iv*, but the difference is small.

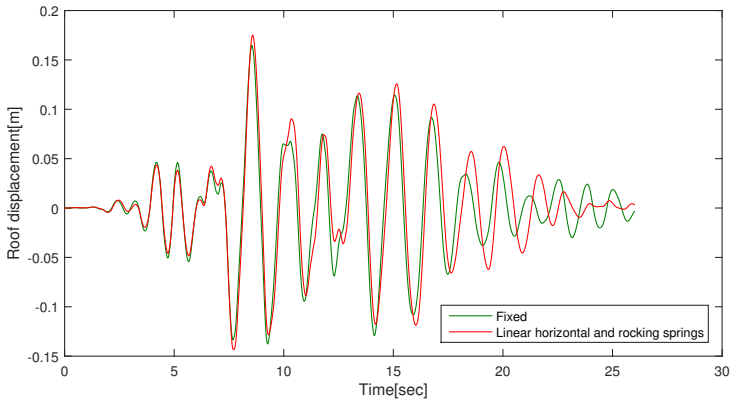


Figure 8.62: Displacement of roof for structure with linear soil springs, and foundation of $1.5\text{m} \times 1.5\text{m}$.

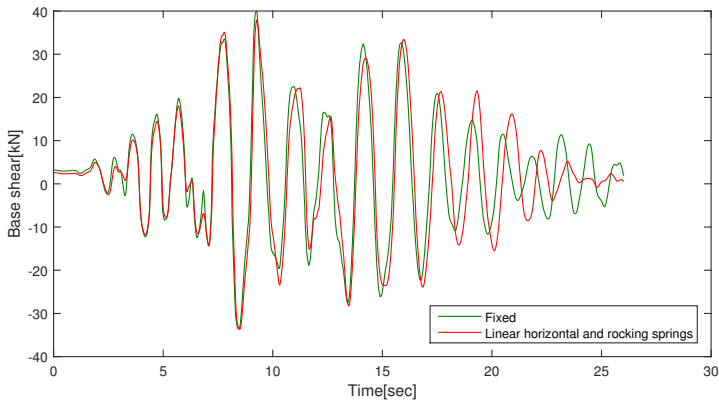


Figure 8.63: Base shear at base of column with linear soil springs, and foundation of $1.5\text{m} \times 1.5\text{m}$.

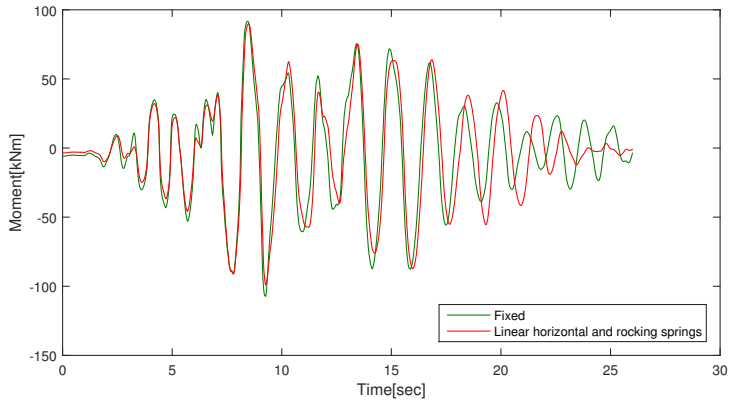


Figure 8.64: Moment at base of column with linear soil springs, and foundation of 1m×1m.

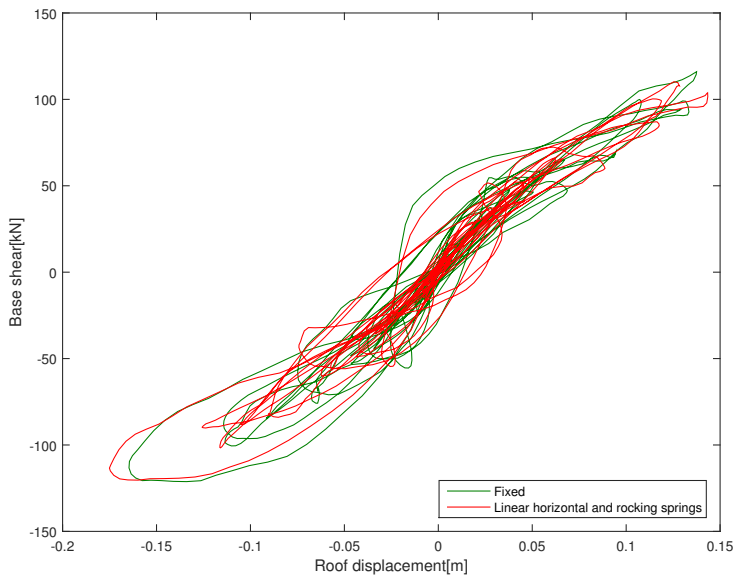


Figure 8.65: Force-displacement response for structure with linear soil springs, and foundation of 1.5m×1.5m.

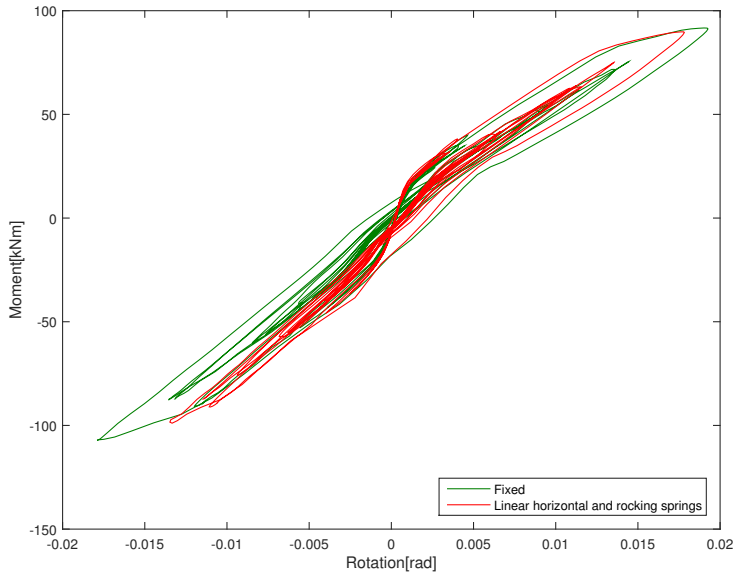


Figure 8.66: Moment-rotation response at base of column at ground floor. Linear soil springs applied at the base of the structure, and foundation of 1.5m×1.5m.

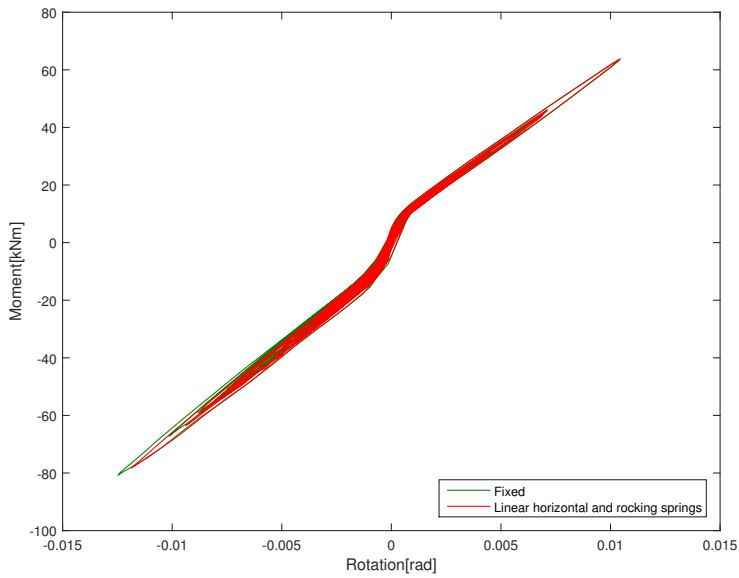


Figure 8.67: Moment-rotation response at base of column in first floor. Linear soil springs applied at the base of the structure, and foundation of 1.5m×1.5m.

In Table 8.4 a summary of the results from all of the analyses for the two story building are given. It is clear that the results are most affected by the change of the foundation size for the two story structure as well. However, the reduction is not of the same magnitude as when the smaller foundation was used for the one story structure. There are several factors that may be the reason why, but one worth mentioning is that the reduction of the foundation is not the same in percentage. The $2m \times 2m$ foundation is reduced by 43.8% while the $1.5m \times 1.5m$ foundation is reduced by 55.6%.

Table 8.4: Maximum moment for the different analyses for the two story building, and reduction of maximum moment for the fixed structure in percent.

Two story building		
Boundary conditions	Maximum moment	Reduction
<i>i.</i> Fixed horizontal springs, linear rocking springs	106.3kNm	0.8%
<i>ii.</i> Fixed rocking springs, Nonlinear horizontal springs	104.1kNm	2.9%
<i>iii.</i> Fixed horizontal springs, linear rocking springs - 0.5g	114.8kNm	0.0%
<i>iv.</i> Fixed horizontal springs, linear rocking springs - $1.5m \times 1.5m$ foundation	99.5kNm	7.2%
<i>v.</i> Linear horizontal springs, linear rocking springs - $1.5m \times 1.5m$ foundation	98.9kNm	7.7%

8.4 Conclusions

Based on the analyses done, and the results presented in the previous chapters, some conclusions can be drawn.

From the first set of analyses in Chapter 6 it was found that the effect of change in number of elements varies a lot for the three different element types. From the pushover analyses it was seen that the DB elements yields for a different force for the different analyses, the FB elements analyses terminates for different displacements and for the PH elements, the different analyses collapses for different displacements. The effect of different spacing in stirrups was also investigated in the same chapter, and was done by pushover analyses as well. The effect of different spacing in the stirrups turned out to be quite small under unidirectional loading. The bidirectional pushover, on the other hand, gives results that varies for the different spacings for all element types. It was observed that the column with a spacing of 50mm was able to withstand the largest force for all elements.

In Chapter 8 the effect of change in stirrups was examined again, but this time through the use of a 3D-model that is exposed to an excitation. From the analyses in Section 8.1 it was found that the change in spacing do not affect the displacement or base shear in any way. A hand calculation was therefore done, to see if the force measured in the structure was too low to see an effect of the stirrups. The hand calculations gave a dimensioning shear force of 71.7kN , while the observed force was 36.0kN . The acceleration was increased to be 5 and 10 times higher to see if the spacing in stirrups then would affect the results. From the analyses with a higher acceleration, the displacements differed for the different spacings.

The last two sections of the thesis presents the effect of SSI, for respectively a one and two story building. It has been observed that by changing different parameters, the effect of SSI has varied. The maximum moment has been reduced within the range from 0 to 23.6% for the different analyses.

From Section 8.2 with the one story building, the most significant effect of SSI was found to be given through reduction of the foundation size. The use of nonlinear horizontal springs or linear rocking springs did only give a slight change to the moment, compared to the reduction of foundation size. From the hysteretic curves from the base of the columns, it was observed that the program gave a moment-rotation response that showed rotation for the fixed columns, i.e. plastic deformation. With rotation included for the fixed structure, it is harder to see the effect of the soil springs, as plasticity in the columns means that rotation already occurs, even when soil springs are not applied. This may be the reason why the response of including soil springs is smaller than expected. The great reduction in moment due to reduced foundation size, must be because of a change of the natural frequency of the structure. As the period is increased, the pseudo spectral acceleration will decrease, which causes lower moments and forces.

For the two story building in Section 8.3, the behavior was similar to the behavior the one story building showed. The analyses gave results that showed the same trend as for the one story building. The effect of SSI was still shown best when the foundation size was decreased, but the reduction was not as good as for the one story structure. This is

probably because the stiffness of the springs does not change the natural frequency the same way as for the one story building. The change of foundation size is not the same in percent for the one and two story building, and this may also be a reason why the effect is more clear for the one story building.

As a concluding remark it can be said that SSI has an effect on the dynamic response of a concrete structure, and that it is possible to reduce the measured maximum force and moment for the modeled structure by use of SSI. It is shown that the effect depends on the choice of hysteretic models in the soil springs, stiffness of the foundation and the intensity of the ground motion.

Bibliography

- Calabrese, A., Almeida, J. P., and Pinho, R. (2010). Numerical issues in distributed inelasticity modeling of rc frame elements for seismic analysis. *Journal of Earthquake Engineering*, 14(sup1):38–68.
- Coleman, J. and Spacone, E. (2001). Localization issues in force-based frame elements. *Journal of Structural Engineering*, 127(11):1257–1265.
- Ferrara, L. and Negro, P. (2004). Seismic behaviour of reinforced concrete structures: Test on the cast-in-situ prototype.
- Filippou, F. (2013). Lecture notes from *CE221 Nonlinear Structural Analysis*. University of California, Berkeley.
- Gharakhanloo, A. (2014). Distributed and concentrated inelasticity beam-column elements used in earthquake engineering.
- Hillerborg, A. (1990). Fracture mechanics concepts applied to moment capacity and rotational capacity of reinforced concrete beams. *Engineering Fracture Mechanics*, 35(1–3).
- Jansen, D. and Shah, S. (1997). Effect of length on compressive strain softening of concrete. *Journal of Engineering Mechanics*, 123(1):25–35.
- Kausel, E., Whitman, R. V., Morray, J. P., and Elsabee, F. (1978). The spring method for embedded foundations. *Nuclear Engineering and Design*, 48(2–3):377–392.
- Neuenhofer, A. and Filippou, F. (1997). Evaluation of nonlinear frame finite-element models. *Journal of Structural Engineering*, 123(7):958–966.
- Otani, S. (1980). Nonlinear dynamic analysis of reinforced concrete building structures. *Canadian Journal*.
- Paulay, T. and Priestley, M. J. N. (2009). *Seismic Design of Reinforced Concrete and Masonry Buildings*. John Wiley & Sons Inc.
- Pecker, A. (2008). Advanced earthquake engineering analysis.
- Ruaumoko (2005). Ruaumoko Website. <http://www.civil.canterbury.ac.nz/ruaumoko/hystresis.html>. [Online; accessed 5-May-2015].

- Saiidi, M. and Sozen, M. A. (1979). *Simple and complex models for nonlinear seismic response of reinforced concrete structures*. University of Illinois at Urbana-Champaign.
- Scott, M. H. and Fenves, G. L. (2006). Plastic hinge integration methods for force-based beam-column elements. *Journal of Structural Engineering*, 132(2):244–252.
- Scott, M. H. and Ryan, K. L. (2013). Moment-rotation behavior of force-based plastic hinge elements. *Earthquake Spectra*, 29(2):597–607.
- SeismoSoft (2014a). Seismostruct user manual. http://www.seismosoft.com/Public/EditorUpload/Documents/SeismoStruct_User_Manual_en.pdf.
- SeismoSoft (2014b). Seismostruct v7.0 – a computer program for static and dynamic nonlinear analysis of framed structures, available from <http://www.seismosoft.com>.
- Shinde, D. N., Nair Veena, V., and Pudale Yojana, M. (2014). Pushover analysis of multy story building. *International Journal of Research in Engineering and Technology*.
- Shing, P. B. (2014). Lecture notes from *SE 221 Earthquake Engineering*. University of California, San Diego.
- Standard Norge (2008). Eurocode 2: Design of concrete sructures. part 1-1: General rules and rules for buildings. NS-EN 1992-1-1:2004+NA2008.
- Standard Norge (2014). Eurocode 8: Design of structures for earthquake resistance. part 1: General rules, seismic actions and rules for buildings. NS-EN 1998-1:2004+A1:2013+NA:2014.
- Wolf, J. (1988). *Soil-Structure-Interaction Analysis in Time Domain*. Prentice-Hall.
- Zeris, C. and Mahin, S. (1988). Analysis of reinforced concrete beam-columns under uniaxial excitation. *Journal of Structural Engineering*, 114(4):804–820.